Microfluidic flow of biomimetic tissues

Laura Casas Ferrer

To cite this version:

Laura Casas Ferrer. Microfluidic flow of biomimetic tissues. Biological Physics [physics.bio-ph]. Université de Montpellier, 2022. English. NNT : 2022UMONS001 . tel-03704329

HAL Id: tel-03704329
https://theses.hal.science/tel-03704329
Submitted on 24 Jun 2022

THÈSE POUR OBTENIR LE GRADE DE DOCTEUR DE L'UNIVERSITÉ DE MONTPELLIER

En Physique

École doctorale: Information, Structures, Systèmes

Unité de recherche : Laboratoire Charles Coulomb

Microfluidic flow of biomimetic tissues

Présentée par Laura CASAS FERRER
Le 29 Mars 2022

Devant le jury composé de

Gladys Massiera, Professeure, Université de Montpellier	**Directrice de thèse**
Laura Casanellas, Maître de conférences, Université de Montpellier	**Co-encadrante de thèse**
Lea-Laetitia Pontani, Chargée de Recherche, CNRS	**Rapporteur**
Kheya Sengupta, Directrice de Recherche, CNRS	**Rapporteur**
Sham Tlili, Chargée de Recherche, CNRS	**Examinateur**
Andrea Parmeggiani, Professeur, Université de Montpellier	**Président**

UNIVERSITÉ
DE MONTPELLIER

Table of contents

Abstract – resumé

Abstract: We designed a biomimetic prototissue as a model for cellular tissues that allows to identify the individual role of the different cellular constituents that play a role in the rheological behavior of tissues. The final goal is to characterize the flow behavior of this prototissue under microfluidic confinement. The first part of the Thesis focuses on the design and synthesis of the prototissue from the assembly of Giant Unilamellar Vesicles (GUVs). The ligand-receptor system that we used to drive the assembly was provided by the streptavidin-biotin pair. We have demonstrated that by changing the streptavidin-to-biotin ratio, the number of vesicles in solution and the biotin concentration in the vesicle membrane it is possible to tune the size of the aggregates and the compactness of the tissue. We have also been capable of changing the morphology of the biomimetic tissue from 3D-shapes to a 2D-monolayer structure by changing the incubation method. An alternative adhesion system based on DNA tethers was also evaluated. It proved to be effective in tuning the adhesion between vesicles, and was found to allow the design of prototissue with a high level of compaction. In the second part of the Thesis, the rheology of this biomimetic tissue was tested by means of a microfluidic setup. Specifically, a controlled pressure was applied and the deformation of the aggregate as it flowed through a constriction was tracked. The change in the aggregate size and shape was calculated for small aggregates, which contributed to elucidate the nature of their elastic behavior. For larger aggregates, the forward motion of the aggregate front in a microfluidic constriction as a function of time was measured. It was possible to observe a viscoelastic behavior, that we compared to the one observed in soft epithelial tissues. Both the prototissue model and the tools we developed to characterize its rheology can be implemented in the future to investigate cellular tissues mechanical properties varying its key properties: the adhesion between individual cells, the mechanical properties of the cytoskeleton and the cellular activity.

Resumé: Nous avons conçu un prototissu biomimétique comme modèle de tissus cellulaires qui permet d'identifier le rôle individuel des différents constituants cellulaires qui jouent un rôle dans le comportement rhéologique des tissus. L'objectif final est de caractériser le comportement d'écoulement de ce prototissu sous confinement microfluidique. La première partie de la thèse se concentre sur la conception et la synthèse du prototissu à partir de l'assemblage de Vésicules Unilamellaires Géantes (GUVs). Le système ligand-récepteur que nous avons utilisé pour l'assemblage est la paire streptavidine-biotine. Nous avons démontré qu'en modifiant le rapport streptavidine-biotine, le nombre de vésicules en solution et la concentration de biotine dans la membrane des vésicules, il est possible de contrôler la taille des agrégats et la compacité du tissu. Nous avons également modifié la morphologie du tissu biomimétique en changeant la méthode d'incubation, passant ainsi de formes 3D à une structure monocouche 2D. Un autre système d'adhésion basé sur des complémentarités de séquences d’ADN a également été évalué. Il s'est avéré efficace pour contrôler l'adhésion entre les vésicules, et a permis de concevoir des prototissus avec un niveau élevé de compaction. Dans la deuxième partie de la thèse, la rhéologie de ce tissu biomimétique a été testée au moyen d'une configuration microfluidique. Plus précisément, une pression contrôlée a été appliquée et la déformation de l'agrégat lors de son écoulement à travers une constriction a été suivie. Le changement de taille et de forme de l'agrégat a été calculé pour les petits agrégats, ce qui a contribué à élucider la nature de leur comportement élastique. Pour les agrégats plus grands, le mouvement vers l'avant du front de l'agrégat dans une constriction microfluidique en fonction du temps a été mesuré. Il a été possible d'observer un comportement viscoélastique, que nous avons comparé à celui observé dans les tissus épithéliaux. Le modèle de prototissu et les outils que nous avons développés pour caractériser sa rhéologie peuvent être mis en œuvre à présent pour étudier les propriétés mécaniques des tissus cellulaires en faisant varier ses propriétés clés : l'adhésion entre les cellules individuelles, les propriétés mécaniques du cytosquelette et l'activité cellulaire.

Chapter 1. Introduction.

In the beginning of the 20th century, physics and biology, which until then remained relatively separated, started to become more and more intertwined: common patterns in both disciplines were being found, and scientists thrived to rationalize what was the link between them [1]. D'Arcy Wentworth Thompson, Scottish biologist and mathematician, discussed for the first time in his 1917 work *On Growth and Form* how forces shape the morphology of organisms, cells and tissues [2]. Since then, the study of the effect of external forces on living matter and how living matter itself can generate forces have become central topics of research in the biophysics field. Another important remark that Thompson made was that the organization of bubbles within a soap froth was akin to how cells organize in a tissue. This observation paved the way for other scientists to delve into the common properties between liquid-like materials and cellular tissues, and how physics can be applied to study forces that drive biological processes. Morphogenesis, that is the process by which the different structures of an organism take shape and organize into tissues and organs, is the result of the organized flow of tissues arising from cell-generated forces and biochemical inputs. Figure 1 illustrates an example of tissue flow during morphogenesis in the model organism *Drosophila melanogaster*. This process, which is ubiquitous and crucial for the development of complex organisms, was studied by American biologist Malcolm S. Steinberg. He proposed that cells in a developing tissue such as an embryo sort into different layers in a similar way immiscible fluids do [3]. The force that drives the separation arises from the difference in surface tension between different types of cells, in a similar way immiscible fluids separate when they are put in contact with each other. Since more and more common features between soft biological materials and liquids were being found, there was a growing need in developing techniques that allowed to study their mechanical properties, both *in vivo* and *in vitro*. The branch of science that deals with how materials flow in response to an applied stress is rheology. Originally focused on studying the mechanical properties of inert solids or liquids, rheometric techniques were adapted to the study of biological matter to characterize its mechanical properties, and enabled to quantify rheological parameters like the elastic modulus or the viscosity. The outcome of these measurements has led to a better understanding on the rheological properties of cells and tissues, and how they can be used as a marker for pathologies. For example, it is known now that the flow of tissues is a key driving mechanism of organogenesis in the embryo [4,5], healthy cells become more fluid-like after undergoing malignant transformation [6], or that it is possible to relate the surface tension with the invasive potential of a tumor [7]. The flow of tissues is a complex phenomenon that arises from many different events: the forces generated by each individual cell, their individual mechanical properties, and the interaction between them through adhesion molecules and intercellular signaling molecules. Correlating the microscopic features of the flow behavior of tissues at the cell level with its macroscopic behavior still remains a challenging task, especially because living matter is an incredibly complex dynamic system with many events taking place simultaneously like cell division, growth, migration, death, and also interaction with the surrounding media. In order to reduce its degree of complexity, in this Thesis we have developed a model biomimetic prototissue with tunable properties. This will allow us to decouple and individually characterize different components of the tissue in a controlled manner, thus allowing us to understand the role that each one of them plays in the collective flow behavior of the tissue.

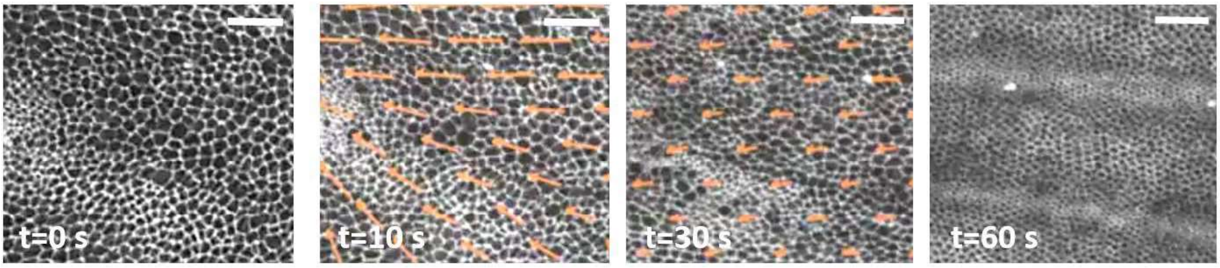

Fig. 1. Snapshots displaying the flow field of cells on the wing of *Drosophila melanogaster* during morphogenesis over a time lapse of 60 s. Cells are initially in a stationary state (0 s) and upon receiving a chemical input, they start reorienting and reorganizing (10 s). Cells flow and migrate (30 s) until they finally reach their final configuration, forming the characteristic microscopic structures of a wing (60 s). The arrows indicate the direction of the flow field. At t = 30 s, it is possible to see how cells stretch and deform as they flow. The translation, reorientation and separation of cells enable the formation of the different patterns forming the *Drosophila melanogaster* wing. Scale bar 50 µm. Adapted from [5].

This Thesis is structured as follows. The first Chapter is an overview of the state of the art in the topic. The second Chapter is dedicated to the materials and methods used for the experimental part. The third and fourth Chapter focus on the assembly of the vesicle prototissue and the study of its rheology behavior respectively. The last Chapter of the Thesis includes the general conclusions of our work and the future perspectives that arise from it.

1.1. Biomimetic tissues as models for cellular tissues.

The structure of the biomimetic tissue that we have developed in this Thesis shares many similarities with the structure of epithelial tissues. Epithelial tissue is found in the lining of organs and also forming the glands, and has the function of protecting against pathogens and mechanical perturbations in the first case and secreting cell products such as hormones in the second [8]. Their most characteristic property is the absence of extracellular matrix (ECM): unlike other tissues, cells are tightly bound to each other forming a barrier through *adherens junctions*, which are a molecular complex that binds the cytoskeleton of adjacent cells between each other forming an interconnected network. In epithelial tissues we can find important events involving the flow of cells, like wound healing, metastasis, and embryogenesis.

The two main cellular components responsible for the mechanical properties of tissues are the acto-myosin cortex and the cell adhesion molecules (CAMs). The cell cortex is a network that lies underneath the cell membrane and is the main responsible for providing cell surface tension and keeping cells' shape. Its structure, made of actin-myosin contractile subunits, allows the cell to resist both external and internal pressure changes, and adapt to them without deforming irreversibly. Cell adhesion molecules, on the other hand, decrease the surface tension between cells by spreading its surface onto one another, thus maximizing the area of contact and sticking them together forming a tissue. The adhesion molecules found in epithelial tissues are E-cadherins, and they are connected to the acto-myosin cortex through protein complexes of α-catenin, β-catenin and vinculin. A scheme on these components and their organization within cellular tisusues is given in Figure 2. Even though the forces provided by these mechanisms are antagonistic, they are inherently related because the cell cortex is linked to the cell adhesion molecules, and therefore their activity cannot be uncoupled from each other. The forces generated by these parts of the cell and their implications in the tissue geometry and compaction will be reviewed in section 1.2.2. of this Chapter. It is important to mention that not all cell-cell interactions are adhesive: in some cases, they induce repulsion. It is the case of the cell surface receptor – ligand interaction of the ephrin/eph pair, which has been proven to have a relevant role in tissue separation during embryogenesis [9,10] . The number of cadherins present in the cells' surface is an indicator of the compaction of the tissue, and by changing its expression level one can tune the tissue surface tension and degree of compaction at will [11]. Cell adhesion takes an important place in the context of cancer and embryogenesis, since diminishing the cadherin expression pattern in the cells' surface allow cells them to detach from their environment. This detachment allows cells to leave their initial position and migrate. In malignant cells, this migration causes metastasis or spreading of the cancerous cells into the adjacent tissues [12]. On the other hand, in cells undergoing embryogenesis, this process allows them to shape themselves into newly formed organs or tissues. Other mechanisms that contribute marginally to the mechanical and rheological behavior of cells are the composition of the cytoplasm, the size and quantity of organelles, the plasmatic membrane, the quantity of interstitial fluid or extracellular matrix, and the size and composition of the glycocalyx. Using a biomimetic alternative instead of a real tissue offers a great framework to study tissue adhesion, since it enables the possibility to have a fine control on the type and quantity of adhesion molecules present in the system, and to have an accurate insight of its role in the rheology of cellular tissues [13–15].

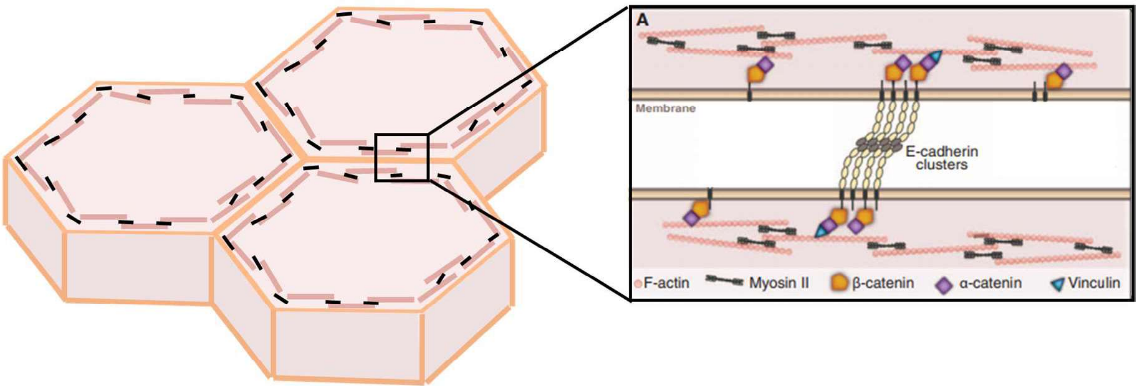

Fig. 2. Drawing of a cluster of cells forming an epithelial tissue. The inset represents the epithelial cell adhesion complex formed by E-cadherins, and the protein complexes that allow its coupling with the acto-myosin subunits of the cell cortex: α-catenin, β-catenin, and vinculin. Adapted from [16].

Biomimetics, also known as biomimicry, consists in withdrawing ideas from biological systems in order to design or adapt a tool or to solve a complex problem [17]. Several examples of the use of biomimetics are the development of antibacterial surfaces based on the microstructure of insect wings or plants [18], using the zip-like structure of burdock plants to create adhesive surfaces like Velcro, or designing flying devices by getting inspiration from the shape of bird wings. Biomimetics has many contact points with synthetic biology, which is the rational engineering of biological systems. Its purpose can be to mimic an already existing phenomenon to better understand how it works or to create novel functionalities that are not present in nature [19]. In the context of our work, we aim to combine concepts of biomimicry and synthetic biology to design biomimetic prototissues based on the assembly of lipid vesicles. It is thus necessary to provide an overview on the strategies that have already been explored to build prototissues in the scientific literature. The mostly used biomimetic units that replace cells in these artificial tissues are droplets, polymersomes, and lipid vesicles [20,21]. Their common feature is that they are spherical entities, formed by a membrane made of amphiphilic molecules that separate an inner compartment from an outer environment, which is usually an aqueous solution. They mimic the shape, size and membrane properties of cells and can be produced in large quantities using well-stablished, reproducible methods. In this Thesis, the system of choice for building the prototissue are giant unilamellar vesicles, an in-depth review of which will be given in section 1.1.1. of this Chapter.

The next step towards the assembly of a biomimetic prototissue is to control the adhesion between its constituting units. Over the last years, numerous methods for driving the assembly between vesicles, and between vesicles and Supported Lipid Bilayers (SLBs) have been investigated. Cadherin-mediated adhesion, which has been mentioned in section 1.1, has been studied in systems composed of SLBs and vesicles, [22–24]. But given the difficulties of handling cadherins *in vitro*, alternative methods were explored. Some of those newly developed assembling methods involve the usage of the electrostatic interaction between oppositely charged molecules [25], lectin-mediated with carbohydrates [26], streptavidin-biotin [27–32], or nucleic acid-mediated interactions [33–37], a summary of which is shown in Table 1. In this Thesis, the method of choice for driving the assembly of the biomimetic tissue is based on the streptavidin-biotin pair. We chose this method because it provides a robust and reproducible framework for inducing vesicle-vesicle assembly. The adhesive properties of DNA tethers have also been explored as an alternative method for inducing vesicle-vesicle assembly. Both vesicle adhesion methods will be reviewed in depth in sections 1.1.2 and 1.1.3. of this Chapter.

Vesicle-vesicle adhesion methods		**References**
E-cadherins	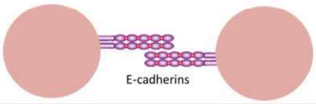	[22-24]
Electrostatic interactions		[25]
Lectin-carbohydrate	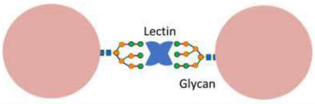	[26]
Streptavidin-biotin	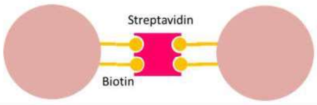	[27-32]
DNA tethers	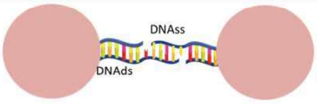	[33-37]

Table 1. Depiction of several different vesicle adhesion methods that are present in the scientific literature.

1.1.1. Giant Unilamellar Vesicles (GUVs).

Giant Unilamellar Vesicles (GUVs) are an excellent model for mimicking cells, and are the system of choice for designing the biomimetic tissue in this Thesis. Vesicles consist in a spherical compartment formed by phospholipids that enclose an inner aqueous space from an outer aqueous media, as shown in Figure 3. They can contain several bilayers in their inside (multilamellar, MLV), a number of smaller vesicles (multivesicular vesicle, MVV), or only have one single lipid bilayer (unilamellar). The latter can be classified depending on their size as small (SUVs <200nm), large (LUVs, 200-1000 nm) or giant unilamellar vesicles (GUVs >1000 nm) [38]. GUVs represent a great framework for biological membrane physics research, because they mimic cells plasma membrane and are cell-like in many aspects: they have a similar composition, similar size, flexible surface, and display a finite volume and area [14]. But despite their numerous similarities, vesicles are simplistic cell models and their complexity is very far from that of real cells. They are strictly passive systems, which cannot divide, grow, move, or metabolize any kind of molecule to obtain energy, and they do not have a cytoskeleton that transmits forces or allows the substance transport within its interior.

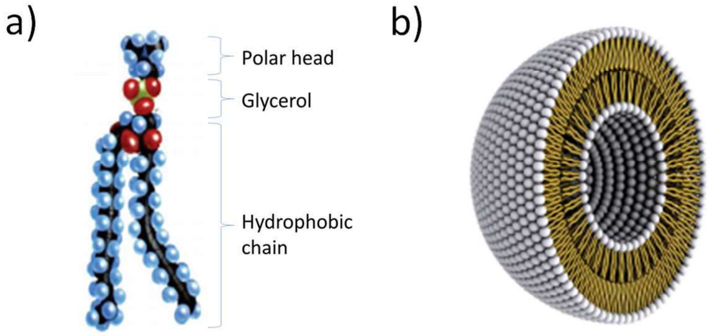

Fig. 3. A. Schematic representation of a phospholipid molecule. The polar head, formed by the phosphate group, points towards the inner and outer aqueous media in which the vesicle is immersed. The hydrophobic chains point inwards and form the inner leaflet of the vesicle. B. 3D Representation of a phospholipid vesicle, with the polar heads in white and the hydrophobic chain in yellow. From [39].

Vesicle production methods started being developed in the mid-20th century, with the rise in the interest for studying biological membranes. Vesicle production by lipid film hydration was the first method to be developed [40] and it consisted in evaporating a thin film of phospholipid solution in chloroform in the bottom of a flask, followed by the addition of an aqueous solution and gentle agitation at room temperature. This strategy had many drawbacks, mostly due to its low yield and long production times. In order to increase the efficiency of the process a step of sonication had to be added, which often oxidized the phospholipids and could impair the vesicle formation process [41].

Two decades later, Batzri *et al.* [42] conceived the vesicle production method by ethanol injection with the aim of solving this problem. In this method, a mixture of lipids dissolved in ethanol was injected through a syringe inside an aqueous solution. Even though the method eliminated the problems that arose from sonication, it still had the major drawback of having to dialyze the vesicles to eliminate the ethanol in the media. It was not until 1986 that vesicle production experienced a major improvement with Angelova and Dimitrov implementing the electroformation method [43], which is our method of choice to produce vesicles for the assembly of the biomimetic tissue. Electroforomation consisted originally in evaporating a phospholipid solution in the surface of two platinum electrodes, applying a voltage difference and immersing them in an aqueous solution. The application of an electric field favored the membrane bending instability, dramatically increasing the yield and decreasing the time of the process compared to the previous protocols, with the advantage of not needing additional steps to obtain the final vesicle solution. Such method was revised by the same authors in 1992 with the implementation of indium tin oxide (ITO) glasses as electrodes [44]. Using transparent conductive glass supposed an important innovation: first, more surface area to spread the phospholipid solution in, which favored their assembly into vesicles as the electroformation process yield was enhanced with decreasing the thickness of the phospholipid layer [45,46]. Second, its transparency allowed them to couple the procedure with optical microscopy, enabling to track the electroformation procedure in real time. But even though electroformation is a reliable, fast and robust method to obtain vesicles with a high yield, it also has inconvenients. The electric field that is needed for producing vesicles makes it difficult to work with solutions with high ionic concentrations. Also, the swelling of the film by molecular permeation does not allow the encapsulation of chemicals or macromolecules of high molecular weight like certain types of drugs or proteins. To solve this problem, a technique for vesicle formation through agarose gel rehydration was developed, which allowed the formation of lipid vesicles in physiological conditions of ionic strength [47]. The process consists in spreading a thin lipid film in an agarose-coated glass coverslip and then immersing it in an aqueous solution containing PBS for at least 1 hour. This gel hydration technique allowed the formation of liposomes in physiological conditions but it still had the drawback of producing highly polydisperse vesicles, with no control over their size or lamellarity. In the last decades, however, the implementation of microfluidic techniques in GUV production has allowed to solve these problems, enabling the possibility to work with volumes in the microliter and nanoliter scale, significantly reducing reaction volumes and lowering production costs [48]. Microfluidic technologies were first implemented in conventional vesicle production methods such as lipid film hydration [49] or extrusion [50], but they did not enhance the yield, encapsulation efficiency, or control of the size and polydispersity of the vesicles. However, the field experienced a significant improvement when it was coupled to techniques such as pulsed jetting [51], double emulsion [52], or phase transfer [53]. These techniques allowed a high encapsulation efficiency in physiological conditions, a good control on the polydispersity and size of the vesicles, and even the formation of asymmetric membranes. Specifically, phase transfer methods remarkably increased the encapsulation yield for large biomolecules, which is of great interest for bottom-up synthetic biology approaches and pharmacology applications [54]. The functioning principle of cDICE, which allows high throughput monodisperse vesicle formation and encapsulation, is based on the phase transfer method [55]. This technique is relevant to our work because it allowed us to encapsulate a biomimetic cytoskeleton reconstitution inside GUVs. Details on the functioning of cDICE and encapsulation procedure will be given in sections 2.1.2 and 2.3 of Chapter 2 respectively.

1.1.2. Vesicle adhesion molecules

In order to mimic cell-cell adhesion in the vesicle prototissue, Streptavidin-biotin pair and DNA tethers were used. Both interactions are robust and well characterized, and have successfully been implemented in a wide variety of both *in vitro* and *in vivo* systems. A review in the most relevant articles involving vesicle-vesicle adhesion will be given after explaining in detail the properties of streptavidin-biotin and DNA tethers.

Streptavidin – biotin

The Streptavidin-biotin pair is well-known for its high affinity constant of $K_a = 10^{15}\ M^{-1}$, which has been widely used for a great variety of biotechnological applications: protein purification, diagnostics, biosensors, to name only but a few [56]. Streptavidin is a 60 kDa tetrameric protein synthesized by the yeast *Streptomyces avidinii*, with four biotin-binding sites, one per subunit. Biotin is a cofactor, also known as B7 or H vitamin, which is biosynthesized by microbes and plants and is necessary for the homeostasis of mammalian organisms [57]. The streptavidin-biotin pair is the strongest biological interaction known to date, with an adhesion energy of 35 k_BT [58]. This value is beyond the cadherin interaction energy, which is between 2 and 12 k_BT [14]. In the vesicle prototissue designed in this Thesis, the streptavidin is in solution and the biotin is attached to the end of a Polyethylene Glycol (PEG) arm, which is grafted to the vesicle membrane through a 1,2-Distearoyl-sn-glycero-3-phosphorylethanolamine (DSPE) molecule as schematized in Figure 4A. The PEG arm gives biotin a higher degree of mobility, allowing it to access a larger number of spatial configurations. Such construct has already been used in studies regarding adsorption and binding affinity between vesicles [29,31], membrane tether coalescence [59], membrane adhesion between vesicles and supported lipid bilayers [32], and in the effect of pressure in biomimetic emulsions [28]. PEG is often used as a mimic for the cell glycocalyx, preventing the adsorption of non-specific proteins to the vesicles as well as non-specific vesicle-vesicle aggregation [60]. The ratio between streptavidin and biotin molecules in the system is defined by X, as shown schematically in Figure 4B. Scientific literature shows that by tuning this parameter it is possible to control the degree of adhesion between vesicles and supported lipid bilayers, which will be discussed further in section 1.1.3. The methods for control of X for the assembly of the vesicle prototissue will be provided in section 2.2.1 of Chapter 2.

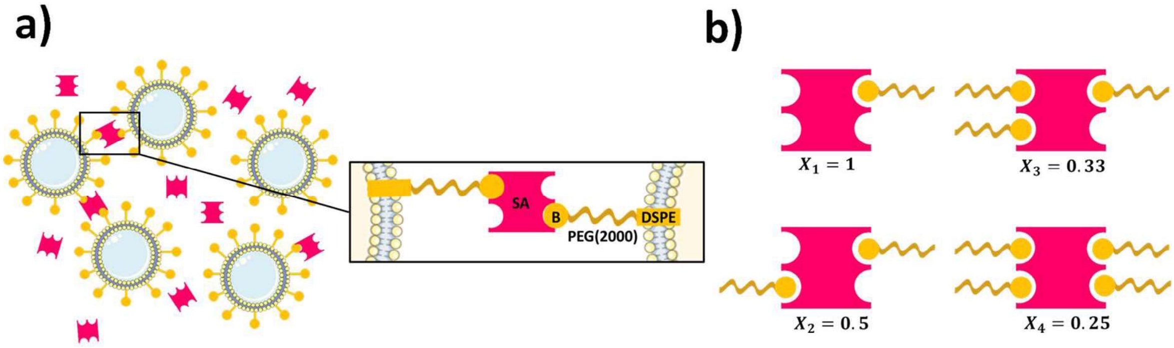

Fig. 4. A. Scheme of the biotin-functionalized vesicle aggregation with streptavidin (SA). The inset shows the synthetic construct made of DSPE, PEG and biotin (B) composing the vesicle membranes. Streptavidin molecules are added in solution. B. Graphical representation of X for one streptavidin molecule and its possible configurations depending on the number of biotins interacting with it. X_1 =1 streptavidin/1 biotin molecule, $X_2 = 1$ streptavidin/2 biotin molecules, $X_3 = 1$ streptavidin/3 biotin molecules, $X_4 = 1$ streptavidin/4 biotin molecules.

DNA tethers

In the last decades, DNA technologies have grown massively in the field of biotechnology to explore the functionalities of genes, tune the genetic expression pattern of certain organisms, or design new metabolic and protein synthesis circuits *de novo*. And even though DNA is undeniably interesting for its information storage properties, it can also be of good use as a structural molecule. While biotechnology was exploring the performance of DNA as a functional molecule, synthetic chemistry and structural biology joined efforts to rediscover its structural properties and mechanics. With the output of their research, technologies like DNA origamis [61] or DNA strands used as force sensors [62] were developed, and they are nowadays used as supramolecular building blocks for synthetic chemistry and for force spectroscopy applications respectively. These technologies were also proven to be very valuable tools for biomimetics and synthetic biology; for instance, they have been used as constructs that allow adhesion between magnetic particles [63], colloids [64], emulsion droplets [33,65], vesicles [36,37], or cells [66]. The DNA-based method chosen to drive the assembly between vesicles in this Thesis is the construct designed by Di Michele *et al.* [36], which was originally developed by Beales *et al.* [35] and will be described in section 1.1.3. This molecule consists in a cholesterol anchor that allows insertion to the vesicle membrane, followed by a DNA double strand (DNAds) of 46 base pairs and a DNA single strand (DNAss) end with 9 base pairs, as shown schematically in Figure 5. The force that drives the vesicle adhesion is the complementarity between DNAss strands or, more specifically, the hydrogen bonding between complementary base pairs. The protocol for vesicle functionalization with DNA tethers will be provided in section 2.2.2 of Chapter 2.

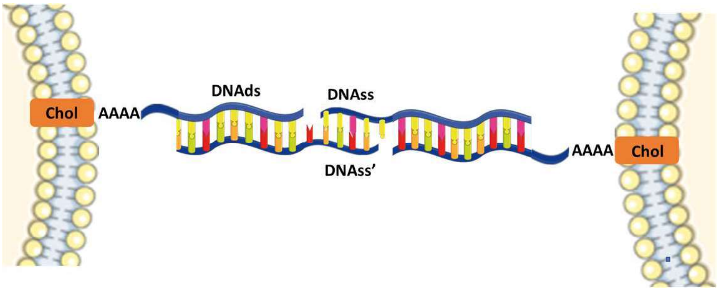

Fig. 5. Sketch of the DNA tethers that drive the assembly between vesicles.

1.1.3. Vesicle prototissues: state of the art.

In this section a review on the most relevant studies for our work regarding vesicle adhesion methods will be provided. The methods to be reviewed consist in the usage of the streptavidin-biotin pair and DNA tethers as drivers for vesicle assembly with the aim of designing model vesicle prototissues.

In 2017, Amjad *et al.* [30] demonstrated that it was possible to control the degree of adhesion between vesicles and SLBs by using the streptavidin-biotin pair. The membranes of both vesicles and SLB contained phospholipids decorated with a DNA double strand (DNAds) spacer with a biotin molecule on top, and streptavidin was added in solution to drive the assembly. This DNA spacer was implemented in order to give higher spatial flexibility to the biotin molecule. The occurrence and degree of adhesion between vesicles and SLBs was imaged by confocal microscopy, and complementary studies on membrane adhesion and bond formation were performed by using flickering spectroscopy and fluorescence recovery after photobleaching (FRAP) assays. The ratio between the quantity of biotin and streptavidin molecules in the system, defined as X, determinated the probability of assembly between vesicles and SLBs. Taking into account that every streptavidin has 4 binding sites for biotin, they defined as bridges the complexes formed by two, three or four biotin molecules simultaneously interacting in opposite sides of a streptavidin molecule, as shown in Figure 6A. The formation of bridges was what drove the interaction between vesicles and SLBs. In the first part of their study, they modelled the density of bridges between vesicles and SLBs in two different regimes: $X > 1/4$, in which there was more than one streptavidin molecule per biotin in solution, and $X \leq 1/4$, in which the quantity of streptavidin in solution was not enough to bind all available biotin binding sites and thus free biotins are left in the vesicle membrane. Ideally, the highest concentration of bridges and therefore the highest adhesion regime between vesicles and SLBs would be found at exactly $X = 1/4$, in which all streptavidin sites are occupied by a biotin molecule. Having these three scenarios in mind, they experimentally measured the fraction of adhering vesicles in the SLBs at different values of streptavidin-biotin ratio X. They observed three easily distinguishable X regimes: low, intermediate, and high, which are shown in Figure 6B. At low X regime, all streptavidin molecules were bound to biotin but their concentration was still too low to produce any effective adhesion between vesicles and SLB. They found the same for the high X regime, in which all biotin sites were passivated by streptavidin and therefore no interaction between vesicles and SLBs was possible. As predicted by their model, the highest vesicle adhering fraction was found in an intermediate regime, in which the ratio between streptavidin and biotin was adequate for producing bridge-like complexes between the membranes of vesicles and SLBs.

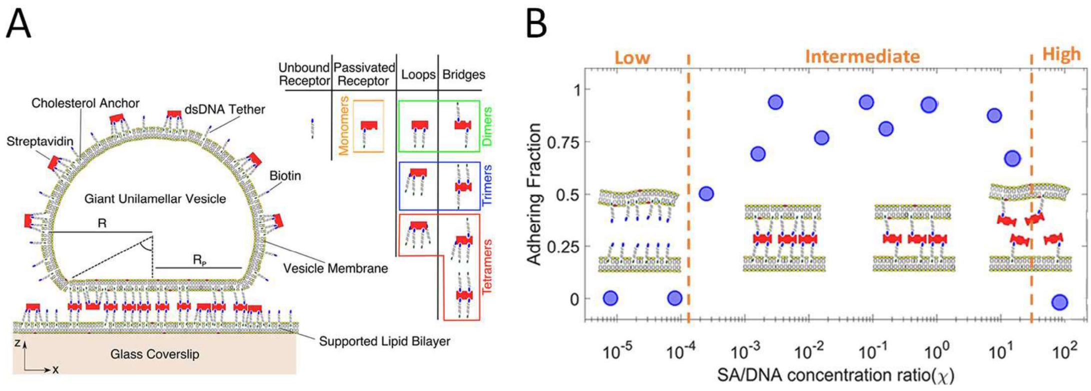

Fig. 6. A. Giant unilamellar vesicle (GUV) interacting with a supported lipid bilayer (SLB) through streptavidin-biotin bridges. B. Adhering fraction of GUVs as a function of the streptavidin/DNA concentration ratio X. In the text DNA is referred to as biotin, since every DNA molecule has a biotin it its tip. From [30].

Another important contribution to the knowledge on vesicle adhesion was published by Beales *et al.* [35] in 2007, which is the first article to our knowledge which used DNA tethers to assemble vesicles. The relevance of this paper for our work lies in the ability of tuning the size of their vesicle-vesicle aggregates by changing the concentration of DNA and the ionic strength of the solution. By changing the ionic strength of the solution one can increase the strength of interaction between DNAds strands, because the positive ions interact with the negative phosphate groups of the DNA backbone, stabilizing its structure. In this study, different concentrations of cholesterol-modified DNA single strands (DNAss) were added to populations of large (LUV) and giant (GUV) unilamellar vesicles. The cholesterol anchor allowed the grafting of the molecules in the membrane, and the adhesion was driven by the hydrogen bonding between complementary base pairs of the DNAss sequences grafted in the vesicles' surface. The ionic strength was also tuned by changing the concentration of NaCl in solution. After 30 minutes of incubation, the vesicle's membrane was imaged by confocal microscopy. Figure 7 shows vesicle aggregation upon changes of the DNA concentration and the ionic strength of the solution. Three different regimes were distinguished: no aggregation, small aggregates with free vesicles, and large aggregates. The results show that size control of vesicle aggregates is possible by tuning these two parameters. By increasing the DNA concentration, the anchoring points for vesicle-vesicle interaction also increase, therefore yielding larger aggregates. Higher ionic strength allowed to obtain large aggregates, due to the stabilization of the interaction between DNAds molecules. The ionic strength used in the DNA assemblies presented in this Thesis was of 80 [Na$^+$] mM, which is within the range in which large DNA aggregates were obtained.

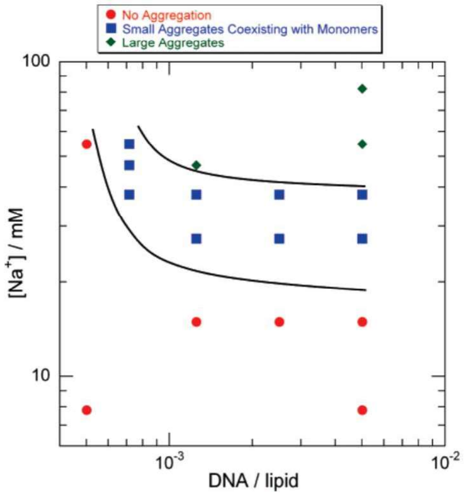

Fig. 7. Changes in the aggregation regime of DNAss-functionalized GUVs upon changes in the ionic strength of the solution and in the concentration of DNA molecules. Circles represent no aggregation, squares represent small aggregates coexisting with free vesicles, and diamonds account for large aggregates. From [35].

1.1.4. Encapsulation of a biomimetic cytoskeleton reconstitution.

As mentioned in section 1.1, one of the biggest interests of synthetic biology is encapsulating individually different parts of the cellular machinery. The cytoskeleton is one of the cell components that has awakened more interest among biophysicists, because it plays a crucial role in processes such as cell division, substance transport, active response to deformation and motility [67]. In the last years, many efforts have been made in order to encapsulate the cell cytoskeleton to better understand its functioning when uncoupled from the rest of the cell components [68]. For example, a reconstitution of the acto-myosin cell cortex has been enclosed inside GUVs [69–71], or attached outside of them [72] to study their dynamics of assembly and its response to deformation. In this Thesis, we aim to take the complexity of the prototissue one step further and add the component of cell activity in it. Our goal is to encapsulate a biomimetic cytoskeleton reconstitution that generates motion by ATP consumption inside biotin-functionalized GUVs [55]. An assembly of active vesicles can be driven by the addition of streptavidin in solution, enabling the design of an active prototissue. This biomimetic reconstitution was first used by Dogic *et al.* [73] and it consists in a mixture of microtubules and kinesins, which produces motion and internal flows in expense of ATP. A detailed description of the mixture and its functioning is given in section 2.3. of Chapter 2. Such encapsulation has already been pursued [74]. Inside the vesicles, the microtubules assembled creating a 2-dimensional network underneath the membrane, in a similar way the acto-myosin cortex organizes in cells. This mixture also generates cytoplasmic streaming, which are mass movements of cytoplasm that occur in large eukaryotic cells and are generated by the cytoskeleton activity [75]. They also seem to induce filopodia-like membrane deformations as shown in Figure 8, which are involved in cellular processes such as migration, wound healing and embryonic development [76]. But even though the cell reconstitution composition is akin to that of the cell cytoskeleton, it does not reproduce its full complexity. In the first instance, the microtubules are not attached to the membrane as it would happen in a real cell, but they are adsorbed in its surface through the action of depletion forces induced by PEG. To increase the level of biomimicry, it would be necessary to include membrane anchoring proteins, which would largely change the dynamics on how the microtubule forces are transmitted to the membrane. The advantage of using this system instead of an acto-myosin cortex reconstitution is that the latter requires sophisticated protein purification and molecular biology techniques to obtain and handle its components. The microtubule-based reconstitution is suitable for handling in a physics laboratory setting, while still proving a good degree of biomimetism for the cell activity. The combination of far-from-equilibrium systems with bottom-up synthetic biology approaches represents an important step towards the creation of new biomaterials that better resemble the properties of real tissues, with noteworthy properties such as autonomous motility and self-organization.

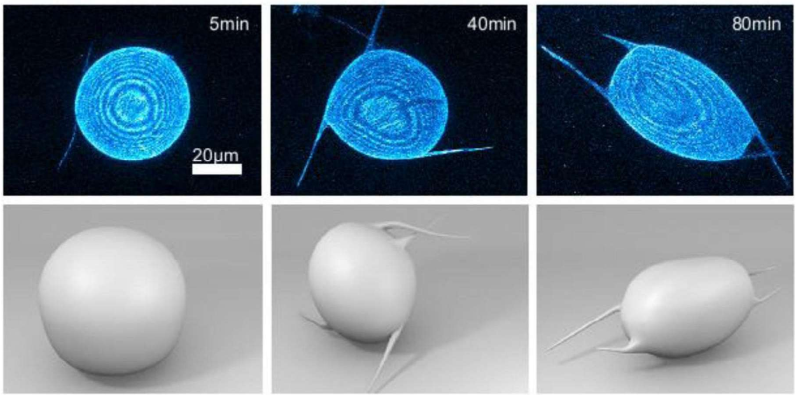

Fig. 8. Image sequence of the encapsulated cytoskeleton inside a GUV obtained by confocal microscopy, over a time lapse of 80 minutes. The row above is a 2D projection of the vesicles, with fluorescently labelled microtubules. The images below are 3D reconstructions of the image stacks. The cytoskeleton reconstitution lies underneath the membrane, and its activity induces filopodia-like deformations. From [74].

1.2. Tissue mechanics and rheology.

In this part, an insight on the methods used to apply and quantify the forces acting on and arising from cells and tissues will be given, starting with a few basic concepts on rheology and then focusing on specific experimental approaches developed for measuring forces at the cell and tissue scale.

1.2.1. Rheology principles relevant to the study of tissue flow.

Rheology studies the deformation of materials to an applied stress. Stress (σ) is the applied force per unit area (Pa in SI units), and strain (γ) is dimensionless and accounts for the relative deformation (or the deformation divided by the original length of the material). Constitutive equations describe the relation between the stress and the strain. Depending on the geometry used to probe the mechanical response of the material one can distinguish between shear or elongational stresses. In shear mode, the force is applied along the surface and the strain is calculated as $\gamma = \Delta x/h$; in the elongational mode, the force is applied perpendicular to the surface and the strain is calculated as $\varepsilon = \Delta L/L_0$ [77]. Both types of deformation are shown schematically in Figure 9A and 9B respectively. In this Thesis we studied the rheology of vesicle prototissues in microfluic confinement, in which the geometry of the microfluidic channel sets the mode of deformation. In the constriction channels we used, the flow is composed of a mixture of shear and elongational modes, and will be discussed further in Chapter 2.

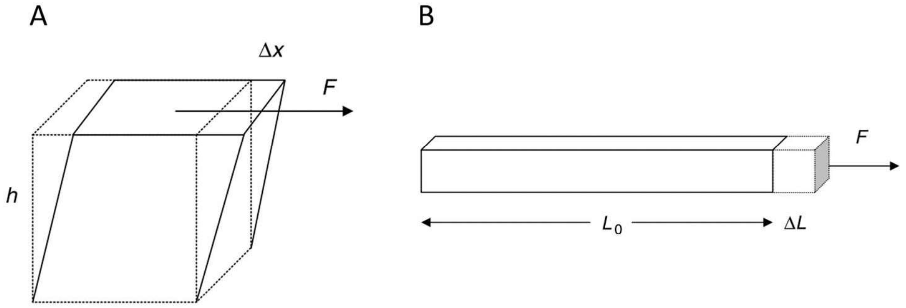

Fig.9. A. Material element undergoing a deformation by shear stress. B. Material element deforming under elongational stress. From [77].

How can we classify the rheology of soft materials and in particular how can we define the rheological behavior of tissues? Before tackling this question, it will be first necessary to briefly review the rheology of elastic solids and Newtonian fluids. Elastic solids deform linearly with the applied stress and as soon as the stress is released they return to their original state. The constitutive equation that describes this behavior under shear stress is the Hooke's law (Eq. (1)):

$$\sigma = G_0\,\gamma \ (1)$$

where G_0 is the elastic modulus, which is the parameter that quantifies the resistance of a material to an elastic deformation. An ideal Newtonian fluid, instead, flows as long as a stress is applied, and the flow rate is proportional to the applied stress($\gamma^{\cdot}$). Viscosity (η) relates the stress to the shear rate, and it is constant in Newtonian liquids (Eq. (2)):

$$\sigma = \eta\gamma^{\cdot} \ (2)$$

Fluid rheology distinguishes between simple or Newtonian fluids from complex or non-Newtonian fluids. The materials of our interest, which are soft biological materials like mucus, cartilaginous tissue and cell spheroids, belong to the category of complex or non-Newtonian fluids. They usually present viscoelastic properties: they display a response to stress which is a mixture between that of an elastic solid and that of a Newtonian fluid. The simplest constitutive equation for viscoelastic fluids is the Maxwell model, defined by Eq. (3), where t_{relax}, usually defined as λ in the rheology literature, accounts for the relaxation time and corresponds to the ratio between the viscosity and the elastic modulus of the fluid (Eq. (4)):

$$\sigma + t_{relax}\frac{\partial\sigma}{\partial t} = \eta\dot{\gamma} \ (3)$$

$$t_{relax} = \frac{\eta}{G_0} \ (4)$$

t_{relax} sets which component –elastic or viscous- predominates in its rheology behavior: if a stress is applied at $t \ll t_{relax}$ the material deforms elastically; whereas for $t \gg t_{relax}$, the material behaves like a viscous fluid.

Another important parameter to take into account when defining the rheology of soft biological materials is plasticity. Plasticity is the ability of materials to suffer non-reversible structural changes that alter their microstructure when they are deformed above a yielding value. Cellular materials like soap foams [78,79], emulsions [80–82] and cell aggregates [83] display this type of behavior. The constituting subunits of these materials will be referred to as cells for the current explanation. During plastic deformation, cells within a cellular material change their initial position in response to an applied stress, leading to a new microscopic structure of the material. These changes in the topology of the system are called rearrangements or transitions. A rearrangement that relaxes stress is energetically favorable, so the system will overcome an energy barrier in order to achieve the new configuration. The energy is dissipated, making the process irreversible [15]. The most relevant type of transition for our work is known as T1transition. In a T1 transition, a group of 4 hexagonal cells are initially in contact forming two 3-sided junctions, as shown in Figure 10. Upon application of a stress, the cells transition to a high-energy state in which they form a 4-sided junction. This state is, however, unstable, so eventually the energy dissipates giving place to a new topological configuration, in which two new 3-sided junctions are formed [84].

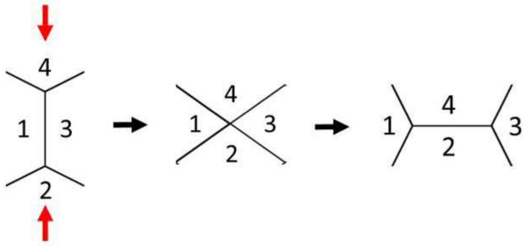

Fig.10. Schema of a T1 spatial rearrangement on a cellular material. The red arrows represent the compressive forces that act on the tissue. Adapted from [84].

1.2.2. Techniques to measure tissue rheology.

In this section we provide a review on the most widely used experimental techniques for the characterization of rheological properties at the scale of individual cells and tissues. The underlying principle of these techniques consists in the application of a known force to the material and measuring the consequent deformation. Since the rheological properties of cells and tissues arise from the interplay between the forces taking place in their inner structure, force inference techniques can be used in order to complement the information obtained with the experimental methods. Both types of approach, together with their advantages and disadvantages, will be described in the following paragraphs.

In this Thesis, the rheology of biomimetic tissues is measured by microfluidic aspiration. Still, there are complementary techniques to measure cell and tissue rheology: parallel plate compression (PPC), micropipette aspiration (MA), Atomic Force Microscopy (AFM) and Optical Tweezers (OT). The main difference between those techniques is that, while plate compression and micropipette aspiration are outstanding tools for measuring the global rheological properties of cells and tissues, their resolution is limited to $10^{-10} N$. OT and AFM have access to the sub-microscopic length scale and can work with forces as small as piconewtons ($10^{-12} N$) [85]. This becomes especially relevant to probe the mechanical properties of single molecules and molecular interactions, elastic properties of the cell cortex or the plasmatic membrane, or of individual organelles like mitochondria and the nucleus. For the scope of the present work, only parallel plate compression and micropipette aspiration will be reviewed in detail.

In parallel plate compression, the sample is deformed at a controlled force by being compressed between two plates, and then allowed to relax to a new equilibrium position [86]. By tracking the shape relaxation as a function of time it is possible to infer the sample´s viscoelastic properties, and by analyzing the radius of curvature of the aggregate when it reaches equilibrium it is possible to to estimate the surface tension, as shown in Figure 11A. With this technique the surface tension and viscoelasticity of cell aggregates have been measured, as well as the interfacial tension of embryos [15,87]. It has also been used as a high-throughput method for screening mechanosensory cytoskeletal proteins in cells [88]. The micropipette aspiration technique was developed by Mitchinson *et al.* [89] in 1954 under the name of cell elastimeter, and it was the first method that enabled to quantify the elastic modulus of single cells. The procedure consists in aspirating the sample -which can be a single cell or hundreds of them - through a glass capillary at a controlled pressure while tracking the length of the aspirated protrusion, as displayed in Figure 11B. The setup consists in a glass micropipette coupled to a system that allows the application of a controlled negative pressure and a manipulator to control its position in the x y and z axis. The sample to analyze is mounted on the stage of the microscope, and with the manipulator the tip of the micropipette is aligned with the sample to be aspirated. Relevant studies using this technique involve the characterization of the viscoelastic properties of cell aggregates [13], mapping tensions of embryo cells to study how the actomyosin cortex generates forces for tissue compaction [90], or probing the mechanical properties of living cells and tissues [91,92]. Both parallel plate and micropipette aspiration methods are robust, easy to implement and have a relatively low cost, but they have some limitations. Firstly, they need an open setup to perform the measurements, which exposes the sample to evaporation and causes a volume change which can be large enough to induce significant experimental uncertainty to the measurements. Also, the setup is very sensitive to vibrations, temperature changes and other experimental fluctuations [93]. In order to overcome these problems, in this Thesis we chose to probe the rheological properties of vesicle prototissue in a microfluidics-based aspiration system, which will be detailed in Chapter 2.

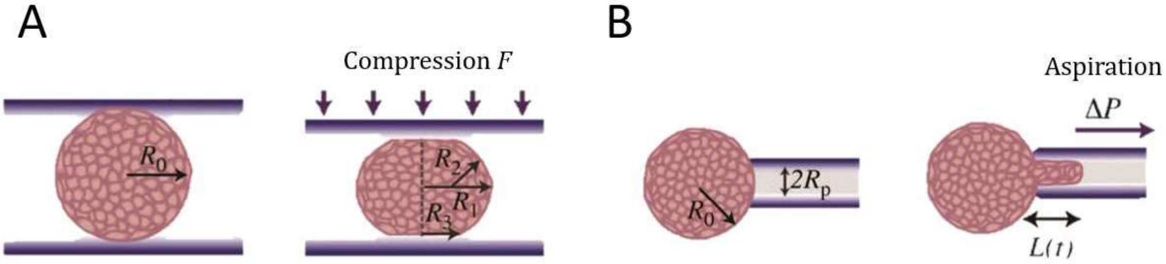

Fig. 11. A. Parallel plate compression experiments. R_0 is the initial radius of the aggregate. Upon compression at a certain force F, the aggregate deforms until a new equilibrium state is reached. R_1 and R_2 correspond to the curvature radii of the compressed aggregate. R_3 is the radii of the contact area of the aggregate with the plates. The surface tension, viscosity and the elastic modulus can be inferred from tracking the changes in the shape deformation with time. B. Micropipette aspiration experiments. The aggregate with an initial radius R_0 is aspirated at a constant pressure difference ΔP in a glass micropipette with a radius R_P. The evolution of the protrusion length with time $L(t)$ is tracked, and the viscosity and elastic modulus are calculated from the stress-strain curves. The aggregates' surface tension is calculated by relating the minimal applied pressure to aspirate the aggregate P_c with R_0, R_P. From [86].

In order to further analyze the forces that play a role in the rheological properties of cells and tissues it is possible to implement force inference techniques. In these techniques, the force actuating or generated by cells or tissues is estimated from analyzing their geometry. These methods do not require a specific setup, only an imaging platform such as confocal or light sheet microscopy to properly visualize the edges and contours of the cells. The forces are calculated through the contact angles of adjacent cells, and they are described in terms of tension (N/m). One important limitation of this type of analysis is that it gives information on the relative values of the forces but not absolute quantities; therefore, the results obtained with force inference methods must be completed and validated with experimental data.

The main driving forces responsible for the geometrical organization of cells within a tissue are adhesion and surface tension forces, which are shown in Figure 12A. The relative tensions can be calculated in symmetric cell doublets, which we may consider as the minimal tissue structure. The

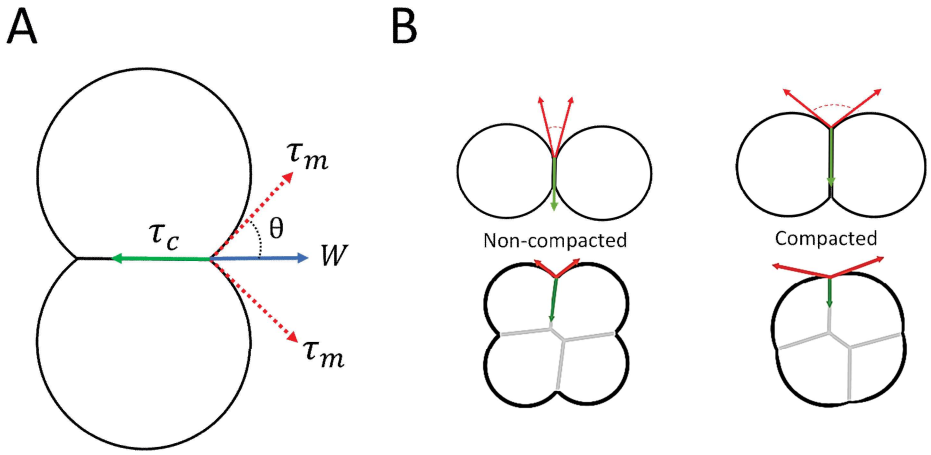

Fig. 12. A. Sketch of a cell doublet with a contact interface defined by the contact angle θ. Red arrows define the vectors corresponding to the cell-medium line tension τ_m and the green arrow corresponds to the cell-cell tension τ_c . The adhesion energy W is defined by the blue arrow. B. Drawing of a non-compacted (left) and compacted (right) cell doublet and aggregate. Adapted fom [94].

cell-medium tension τ_m, indicated in red, is the force arising from the inside of the cell, provided by the actomyosin cortex that lies underneath the membrane. It works by minimizing the surface exposed to the outer media. The cell-cell tension τ_c in green is the force that drives the contact between cells. The adhesion energy W, in blue, is generated by homophilic interactions between cadherins and it acts by maximizing the interaction between cells, increasing their area of contact and keeping them together. One must take into account that, in living matter, τ_c, τ_m and W are affected by the activity of the cell. This activity includes the deformation of the acto-myosin cortex, the changes in the protein expression pattern, the synthesis and transport of metabolites, and others. However, in this section they will be treated purely as forces arising from the mechanical properties of the sample, and the influence of the cell activity will not be considered. In the case of vesicles, τ_c, τ_m and W arise entirely from the mechanical properties of the membrane and the adhesion molecules, since they are passive systems. At equilibrium, the contribution of cell-cell tension, cell-medium tension and cell-cell adhesion energy are balanced, and can be expressed by the Young equation (Eq. (5)) [94]:

$$\tau_c - W = 2\,\tau_m \cos\theta \quad (5)$$

Force inference techniques are especially useful for characterizing the changes in compaction within tissues, in particular those undergoing embryogenesis. Compaction is a very important event that takes place in early stages of development, and it consists in an increase in the cell density within a limited space [94]. The progression of compaction can be defined by studying the contact angle between external cells, as exemplified in Figure 12B.

While it is relatively simple to estimate the relative tensions in doublets, the calculations become more complicated as the number of the cells increases. To tackle this issue, programs like CellFit have been developed [95]. Its algorithm consists, firstly, in segmenting the image of the tissue to identify the edges of the cells and calculate the contact angles between them as shown in Figure 13A. Then the Young equation for each triple junction is built assuming that it is in equilibrium. Next, the relative tension at each cell edge and triple junction is calculated. The result is displayed in a colored code, in which the lowest relative tension value (0) is in the left and the maximal (1) is in the right side of the spectrum as shown in Figure 13B. A more refined method to calculate the tensions in tissues is based on the analysis of the contact angle between cells that form fluid-filled interstitial gaps. Interstitial fluid gaps are present in compact monolayer or multilayered tissues such as the epithelium, and their purpose is to support fluid and osmotic balance, as well as substance exchange between cells. The gaps are generally stable in time, and are found at the intersection between three cells. Winklbauer *et al.* [96] developed a model that is able to correlate how changes in cell-cell and cell-medium tension and cell radii affect the gap's geometry. A graphical depiction of an interstitial gap and its geometrical parameters is provided in Figure 13C. Such model has been validated with experimental data from *Xenopus* embryo explant tissue, an image of which is shown in Figure 13D. [97]. It is important to note that, like in the previous case, in order to relate the geometrical parameters to the mechanical properties of the tissue, it is considered that pressure and tension balances at interstitial gaps are at equilibrium. Even though these last two methods have not been implemented in the current work, they could be used as a tool to map the membrane tensions in 2D tissue-like vesicle aggregates and how these values vary depending on their properties, such as the number of adhesion molecules, the packing fraction, or the vesicle polydispersity.

1.2.3. Microfluidics as a tool to study the flow of tissues.

Microfluidics is the science which studies the behavior of fluids at volumes that range from microliters to femtoliters, and it also deals with the technologies and devices used to handle this minute amounts of fluid. Some examples of naturally occurring microfluidic flows are blood running through capillaries, the cerebrospinal fluid circulation system, and, more closely related to our work, the collective movement of cells in an embryo or the extravasation of tumor cells into the bloodstream. Microfluidics as a discipline was born in the first decade of the 20th century, with the development of microfluidic chips. Microfluidic chips are a collection of micrometric channels imprinted into a material which allow the handling of micrometric volumes of fluids. Originally, microfluidic chips were fabricated with the same techniques as micro-electromechanical systems (MEMS), since their technologies allowed to build channel networks in the microscopic length scale. These techniques worked with silicon and glass to make chips that would serve as electronic storage devices, among many other applications. Over the years, the techniques evolved so they adapted to manipulating fluids in the microscale and specialized to handling biological samples. The material that provided such enhancement was polydimethylsiloxane (PDMS), an elastomeric polymer whose high flexibility and robust methods of production made it a perfect candidate for engraving micrometric channels

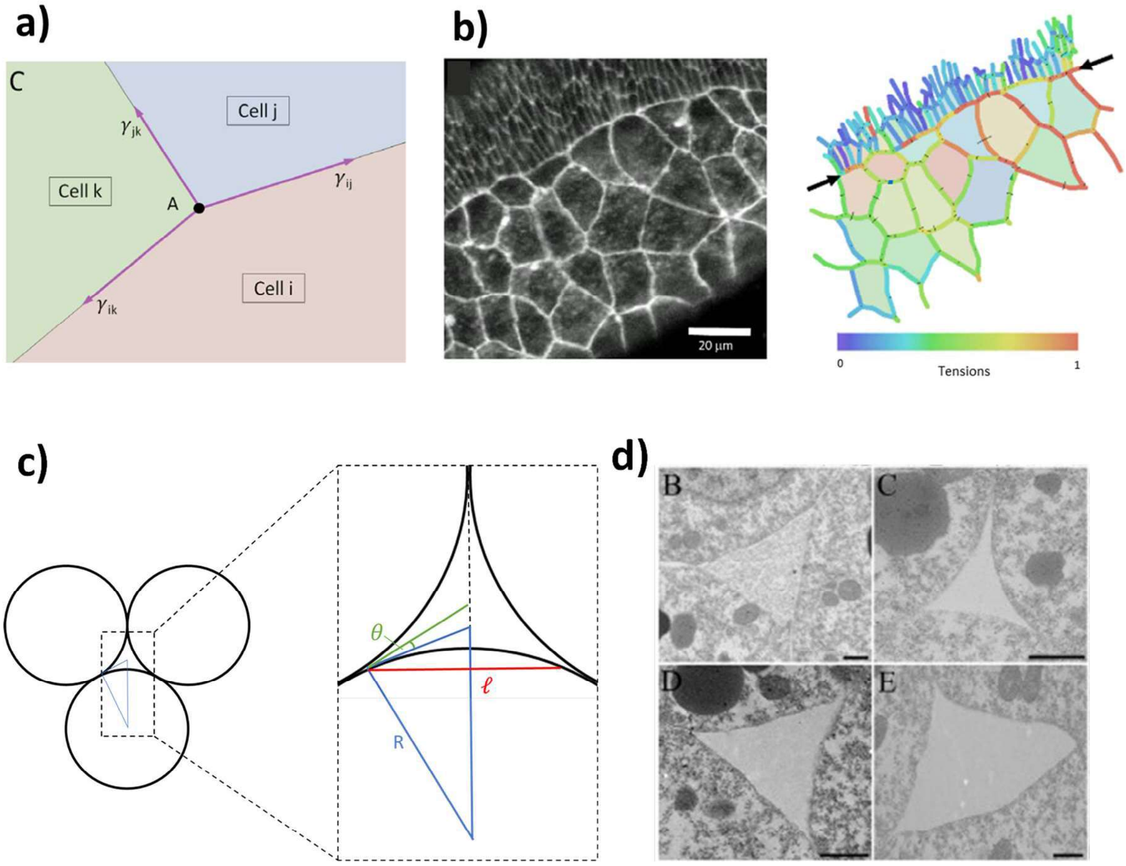

Fig. 13.A. Triple junction on a tissue in the intersection between three cells i, j and k, with their respective edge line tensions $\gamma_{ij}, \gamma_{ik}, \gamma_{ki}$ vectors indicated in purple. B. Color-coded relative tension map on the interface between two tissues in the *Drosophila* embryo: amnioserosa (top) and lateral epidermis (bottom). The cells on the boundary between the two tissues –indicated with black arrows - are subjected to a higher tension than those in their surroundings. From [95]. C. Drawing of an interstitial gap between three cells. The geometrical parameters that describe the gap's morphology are the contact angle between two adjacent cells (θ), the radius of curvature (R), and the gap length (ℓ). Adapted from [96]. D. Electron transmission microscopy image of fluid-filled interstitial gaps in *Xenopus* embryo tissue. Scale bar 1 μm. From [97]

and intricate networks in small-scale settings. Furthermore, PDMS is transparent, which is ideal for visualization through optical microscopy, hydrophobic, and allows irreversible bonding with glass surfaces. Another important characteristic of microfluidics is that in the microscale certain forces that are predominant in the macroscale –such as gravity and inertial forces – become negligible. Under these conditions viscous, elastic and capillary forces become the main driving forces responsible for the observed processes [98]. For all of these characteristics, microfluidics provides outstanding resources to use in the framework of biology and biomedicine research. Its biocompatibility, drastic reduction of the sample size, scalability, decreased reaction times, and relatively easy and low-cost implementation are only some of the many advantages that it offers [99]. The usage of microfluidic techniques to probe the rheology of cells and tissues is of great interest in the context of biomedical investigation. For example, studies in erythrocyte deformability have been made in order to correlate the changes in their stiffness with pathologies such as malaria [100], diabetes [101], or sickle cell anemia [102–104]. The characterization of the rheological properties of cancer cells and tumors was also performed thanks to the application of microfluidic techniques. Tran and coauthors, for example, studied the viscoelastic fracture of model tumors in microfluidic chambers in order to analyze the phenomena of cell detachment and migration to the circulatory system [105,106]. Microfluidic tools also enable the implementation of controlled chemical gradients, which is especially relevant for mimicking morphogenesis and embryonic development processes [107,108]. Other applications of microfluidics in the biomedical field that are worth mentioning are the Lab-on-a-chip and Organ-on-a-chip devices [109], single cell manipulation [110], and systems to encapsulate drugs inside biocompatible microstructures for targeted drug delivery [111]. The interest of using microfluidics in the context of this Thesis is that it enables to probe the rheological properties of the vesicle prototissue in closed controlled geometries and visualize the flow simultaneously in microscopy.

1.2.4. Flow of biomimetic tissues: state of the art.

In this section, the most relevant studies for our work in tissue rheology in microfluidic confinement will be reviewed. The discussion is organized in decreasing order of complexity, starting with epithelial tissue monolayers, continuing with cell aggregates, and finishing with a biomimetic system consisting in an emulsion with adhesive properties. The complexity of our biomimetic system lies in between that of cell aggregates and adhesive emulsions.

In 2020 Tlili *et al.* [112] published a study that discuss the mechanical behavior of an epithelial tissue monolayer. In their study, they wanted to elucidate whether if the behavior of a migrating tissue monolayer made of Madin-Darby Canine Kidney (MDCK) cells corresponded to that of a Kelvin-Voigt viscoelastic solid or to that of a Maxwell viscoelastic liquid. MDCK cells are a line of cells that are widely used for studying epithelia because they have well defined cell-cell adhesion boundaries, fast growth rates, and are able to polarize in both 2D and 3D cell cultures [113]. Most importantly, they have the ability to move collectively while keeping their cohesion, which makes them ideal for studying the rheological properties of migrating epithelial tissues. In order to study the flow behavior of an MDCK migrating tissue, they performed a Stokes experiment under microfluidic confinement. The Stokes experiment is widely used for studying the viscoelastic properties of cellular materials such as foams, emulsions and tissues, and consists in making the fluid of study flow through a narrow channel with a circular obstacle in the middle. In their experiment, they first deposited suspended MDCK cells in one end of a microfluidics strip coated with fibronectin, and allowed them to adhere to the substrate and between each other forming a compact monolayer [114]. The flow of the tissue was recorded as it migrated from one end of the microfluidic strip to the other, passing through the circular obstacle as shown in Figure 14A. The visualization was performed using phase contrast microscopy. The influence of cell division on the flow behavior of the migrating tissue was prevented by using a division inhibitor, and no external pressure was applied to the setup. The process was imaged over a time lapse of 24 h and the 2D deformation of individual cells, their velocity field and rearrangement rate were computed. The region of interest used for calculating these two parameters is provided in the highlighted blue square of Figure 14A. It was found that the cell deformation and the rearrangement rate correlated strongly, a signature characteristic of a Maxwell viscoelastic liquid. The relaxation time t_{relax} could be obtained by the slope of the linear fit between the cell deformation and the rearrangement rate indicated in a dashed black line in Figure 14B, which was of 70 ± 15 min. In a cellular tissue like the MDCK cell monolayer, the relaxation time is related to the time for a group of cells to rearrange, which allow cells to relax their shapes.

The second level in the scale of tissue complexity are cell aggregates. Cell aggregates are obtained from tissues that have been dissociated using tripsin. Trypsinization breaks the cell-cell interactions and eliminates the cell surface molecules that allow tissue-specific adhesion [115]. Upon elimination of tripsin from the media, the cells will aggregate again at a homogeneous rate, forming a spheroidal structure. One of the most relevant characteristics of cell aggregates is that unlike tissues, it is possible to tune their energy of adhesion by controlling their cadherin expression levels [116]. Guevorkian *et al.* [13] studied the viscoelastic properties of murine sarcoma cell aggregates by using the micropipette aspiration technique. They aspirated cell aggregates at a constant pressure while

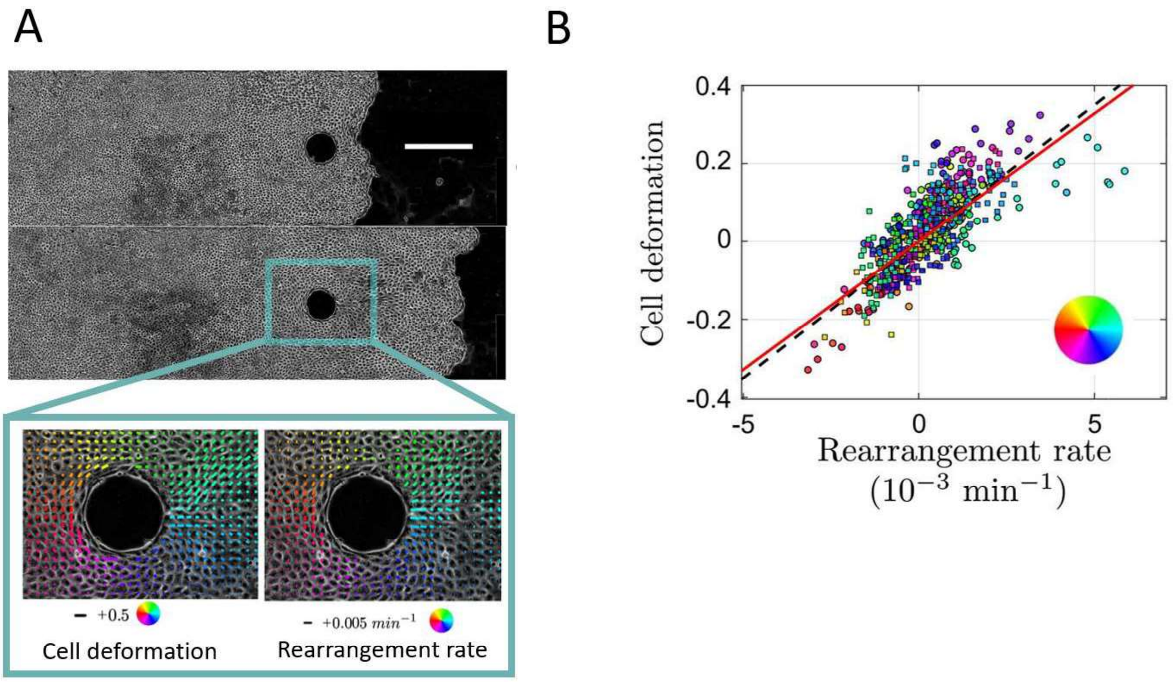

Fig. 14. A. Stokes experiment consisting in the migration of an MCDK cell monolayer across a circular obstacle under microfluidic confinement. The upper panel shows the MDCK cell monolayer 2h after adding the cell division inhibitory drug, which they define as t=0. The bottom panel shows the advancement of the cells at t=12h. The blue square corresponds to the region of interest for calculating the cell deformation (right), and the rearrangement rate (left). The color code represents the angular position in polar coordinates of each analyzed point of the tissue, with the origin being the circular obstacle center. Scale bar: 500 µm. B. Cell deformation as a function of the rearrangement rate. The dashed black line is the linear fit to the data, with a slope τ of 70±15 min. The color code is the same as in Fig. 14A. From [112].

monitoring the deformation of the aspirated tissue with time. After aspiration, the pressure was set to zero and the retraction of the aggregate front with time was also monitored, as shown in Figure 15A. In this experiment, cell division was not inhibited since the timescales used for aspiration were lower than those needed for the cells to undergo mitosis and therefore did not affect the flow behavior of the tissue. In the aspiration curve they observed a fast exponential increase of the tissue deformation followed by a linear increase with time, which is characteristic of viscoelastic materials and is known as creep behavior. The displacement of the aspirated advancing and retracting front in the micropipette was found to be defined by a modified Maxwell model with two relaxation times: t_e and t_{relax}. t_e characterizes the elastic regime and it is defined as the raising time of elastic deformation or elastic local cell's relaxation time. The second, accounted for the global relaxation time t_{relax} for their aggregates was 44±7 min, not far from the 70 ± 15 min that Tlili *et al.* [112] found for their MDCK migrating tissue monolayer. The viscosity and elastic modulus of the aggregates were also inferred, obtaining values of $1.9 \pm 0.3 \cdot 10^5\ Pa \cdot s$ and $700 \pm 100\ Pa$ respectively. Interestingly, they observed that $t_{elastic}$ had different values depending if the model was fitted in the aspiration (t_e^a) or the retraction (t_e^r) curve. They saw that t_e^a was larger than t_e^r, suggesting that previously stressed tissues have a faster elastic response. This change in the rheological properties of the tissue is due to the active response of the cells to the application of a force, also known as mechanosensing. Mechanosensitive responses are essential for cells to adapt to an externally applied stress, and they act mainly on remodeling the cytoskeleton and tuning the expression and distribution of cell adhesion molecules within the membrane.

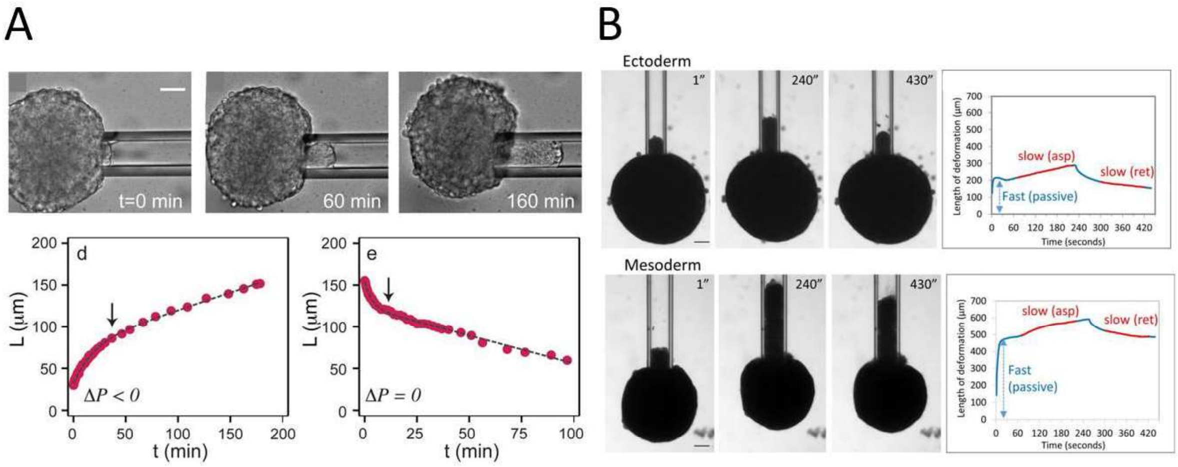

Fig. 15. A. Upper panel: cell aggregates aspirated with a micropipette at times 0, 60 and 160 min after application of a constant pressure of 1370 Pa. Bottom panel: Advancing (left) and retraction (right) of the aggregate front as a function of time. The dotted line indicates the fit of the modified Maxwell model to the experimental data. The black arrow indicates the transition from an elastic to a viscous regime. Scale bar 50 µm. From [13]. B. Micropipette aspiration of ectoderm and mesoderm tissue explants from *Xenopus* in a time interval of 430 seconds. The panels in the right display the advancement of the tissue front inside the micropipette as a function of time. The blue arrow indicates the deformation of the tissue within the first 20 seconds of aspiration. From [92]. Scale bar 100 µm.

Micropipette aspiration has also been used in molecular biology studies to characterize the rheological properties of tissues and how these properties can be tuned by activating or inhibiting specific biochemical pathways. A relevant example is the case of the ectoderm and mesoderm, two embryonic tissues whose viscoelastic properties change with the progression of the embryogenesis process, and this change is essential for the embryo to continue its development into a new organism. Within gastrulation, which is the phase of embryogenesis in which the cells separate into different layers, the ectoderm is formed. Upon the second stage of gastrulation, a part of the cells forming the ectoderm develops into mesoderm [117]. Ectoderm cells have higher cortical stiffness and cadherin expression levels than mesoderm cells, and do not display migratory properties. Mesoderm is more fluid, soft and spreadable than ectoderm, and displays migratory properties. Kashkooli *et al.* [92] performed micropipette aspiration experiments in tissue explants of *Xenopus* ectoderm and mesoderm to test the differences in viscosity, and surface tension between these tissues. Figure 15B displays images of a micropipette aspiration experiment performed in *Xenopus* ectoderm explants for a time interval of 430 seconds. It is possible to see that by applying the same pressure the mesoderm tissue travels further than the ectoderm, which is indicative of a lower resistance to flow and therefore a lower viscosity. The graphs in the right show the measurement of the advancing front inside of the pipette for the aspiration and retraction parts of the experiment. The blue line indicates the ´fast´ or elastic deformation phases and the red line indicates the ´slow' or viscous deformation phases. The viscosity for the three different samples was calculated from the slope of the slow aspiration part of the deformation with time. The average viscosity values calculated for their experiments oscillate between 1 and $2 \cdot 10^3\ Pa \cdot s$, two orders of magnitude smaller than that calculated by Guevorkian *et al.* [13] in their murine sarcoma cell aggregates.

Up to this point, the systems that have been discussed are formed by cells, which are active entities that display high variability and complexity. The next system to be discussed is formed by droplets which are passive, biomimetic entities. The simplicity of the system, which allows a high degree of tunability and reproducibility of the experiments, allows to address complex phenomena that otherwise would be very complicated to study in real cells, like the different mechanisms involved in cell rearrangements. Cell rearrangements are the mechanism that allows tissues to flow with a viscosity η, and are therefore an important event that defines the flow behavior of tissues. The quantification of the cell deformation as a function of the rearrangements rate has been used as to determine the viscoelastic response of a migrating epithelial monolayer, as described in the work by Tlili *et al.* [112] earlier in the text. Golovkova *et al.* [118] wanted to take the discussion one step further and elucidate the role of adhesion in both the cell deformation and the number of rearrangements within a flowing tissue. For this, they used a simplified prototissue consisting in an oil-in-water emulsion. Oil droplets are stabilized through a monolayer of amphiphilic molecules. Their surface can be tuned by adding different types and concentrations of adhesion molecules, which can help mimicking the adhesive properties of cells. Like in the vesicle prototissue developed in this Thesis,

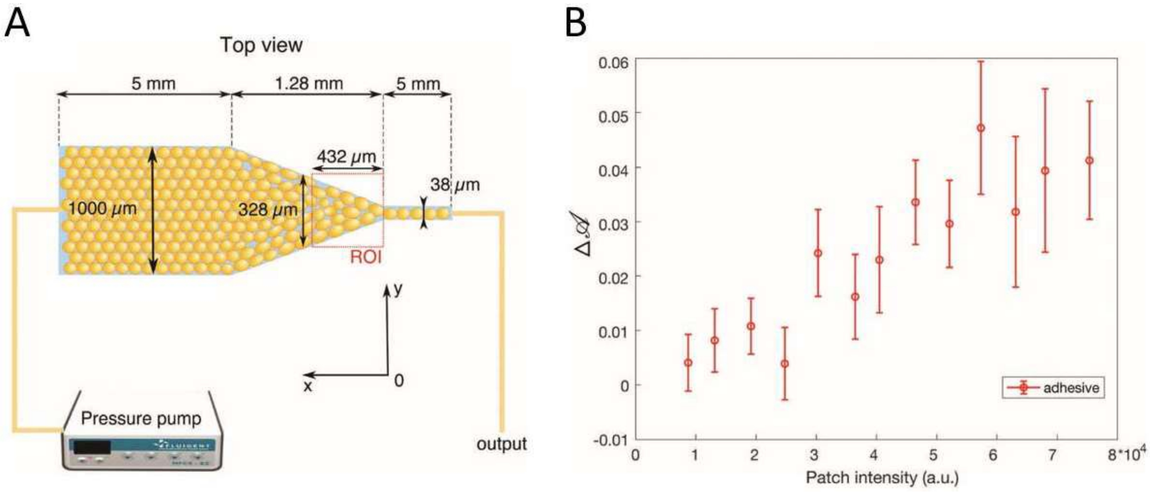

Fig. 16. A. Experimental setup for flowing an oil-in-water emulsion through a microfluidics constriction. B. Shape parameter $\mathcal{A}$ before and after undergoing a T1 rearrangement as a function of the patch intensity. From [118].

the system to drive the assembly in the adhesive emulsion was the Streptavidin-biotin bond. The monolayer at the droplet interface was constituted of EggPC and DSPE-PEG(2000)-biotin molecules. Fluorescent streptavidin was added in solution to drive the droplet assembly. The experimental setup consisted in a microfluidic constriction which was designed to both maximize the number of rearrangements and also to mimic the convergent extensional flow that cells experience during embryogenesis [119]. A drawing of the setup is provided in Figure 16A. The visualization of the droplets as they flowed through the constriction at a constant pressure was performed by using confocal microscopy. Prior to the collection of the quantitative data, a Voronoi tessellation of the space was performed using FIJI, and the neighbors of each droplet were identified for each image. The cell deformation was calculated as the shape parameter $\mathcal{A}$, which is the inverse of the circularity, and also by tracking the aspect ratio of the droplets. The rearrangements were tracked by following the formation or breaking of contacts and edges of the Voronoi cells surrounding each droplet. The measurement of the adhesion patch fluorescence intensity provided by the streptavidin was also performed, in order to monitor the concentration of adhesive binders between droplets. Droplet deformation was computed as a function of the patch intensity before and after undergoing a T1 rearrangement $\Delta\mathcal{A}$. The results showed that droplets that displayed higher deformation values also had higher patch fluorescence intensity levels, suggesting that there was a correlation between the deformation of the droplets and their energy of adhesion as shown in Figure 16B. They analyzed both deformation and rearrangements in droplets with and without streptavidin-biotin in their membranes for comparison. This suggested that adhesion diminished the freedom of the droplets to rearrange, thus increasing the energetic cost of the transition and making them flow more elastically than non-adhesive droplets. Similar results were observed when depletion force was used as a trigger for droplet adhesion: emulsions with higher depletion forces displayed more elastic behavior when flowing through a constriction than those with low depletion forces [81]. These results might help elucidating the role of adhesion in the viscoelastic properties of tissues and open new ideas for studying the flow behavior of cellular tissues *in vitro*.

Chapter 2. Materials and methods

2.1. Vesicle fabrication methods

2.1.1. Electroformation

The first step towards the assembly of the biomimetic prototissue is fabricating giant unilamellar vesicles. The methods we chose for vesicle production are electroformation, which has been reviewed in section 1.1.1. of Chapter 1, and continuous droplet interface crossing encapsulation method (cDICE), which will be detailed in the next section. More specifically, the electroformation protocol used for our experiments was provided by Okumura *et al.* [120], which uses ITO glasses as electrodes and applies increasing pressure voltage to increase the yield and size of the vesicles. The protocol started by spreading a thin layer of Egg phosphatidylcholine solution 100 mg/ml in chloroform (EggPC, Sigma Aldrich, P3556) diluted in a 9:1 chloroform in methanol solution on the conductive side of two ITO glass slides (Sigma Aldrich, 636916). For the biotinylated vesicles, concentrations ranging from 1.25 to 10% mol/mol of DSPE-PEG(2000)-biotin (Avanti Lipids, 880129P) were added to the lipid mixture. The glasses were then assembled together with the conductive sides facing each other using a 1 mm-thick PDMS spacer and the inner space was filled with a sucrose aqueous solution at 290 mOsm/kg (Sigma Aldrich, S7903). A drawing of the electroformation chamber and its components is shown in Fig. 17. The glass plates were connected to an AC function generator and an electric potential difference was applied with increasing steps of 0.2 V every 15 minutes up to 0.8 V at 10 Hz. After 1h, the electric potential was increased again up to 1.2 V every 15 minutes. The last step consisted in leaving the chamber at 1 V and at 4Hz for 20 minutes. The gradual potential increase favored the growth of vesicles in size, and the last additional step at 4 Hz allowed them to detach from the glass, releasing them in the aqueous media. Once the electroformation was finished, the solution was carefully collected and stored in an Eppendorf tube at 4°C for a maximum of one week. In order to visualize the vesicles, they were suspended in a 300 mOsm glucose (Sigma Aldrich, G7021) aqueous solution. Sucrose has a higher density than glucose, which allowed us to sediment the vesicles and provide contrast for observation in phase contrast microscopy. The slight osmolarity difference of +10 mOsm between the inside and the outside of the vesicles provides a slight deflation, providing them with an excess membrane area which is enhances their assembly into a tissue.

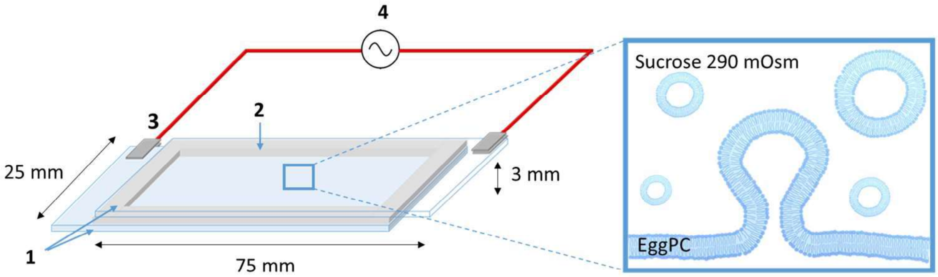

Fig. 17. Drawing of an electroformation chamber with its different parts. The inset displays the electroswelling of a lipid bilayer. 1) ITO glasses, 2) PDMS spacer, 3) Clamps and copper wire, 4) AC generator.

2.1.2. Continuous Droplet Interface Crossing Encapsulation (cDICE).

Despite the high yield, robustness and easy implementation of the electroformation method it had two important limitations: the high size polydispersity of the vesicles and it does not allow to control encapsulation. As reviewed in the previous chapter, interface crossing and microfluidics methods enable the encapsulation of precious substances such as drugs, proteins, or even entire cells in small volumes. For this reason, the second method we used for vesicle production was the continuous droplet interface crossing encapsulation method (cDICE) that enables to control the size and therefore diminish the size polydispersity of the vesicle population, apart from allowing encapsulation [55,121]. Figure 18 illustrates the differences in size distribution we obtained for the two methods: electroformation and cDICE.

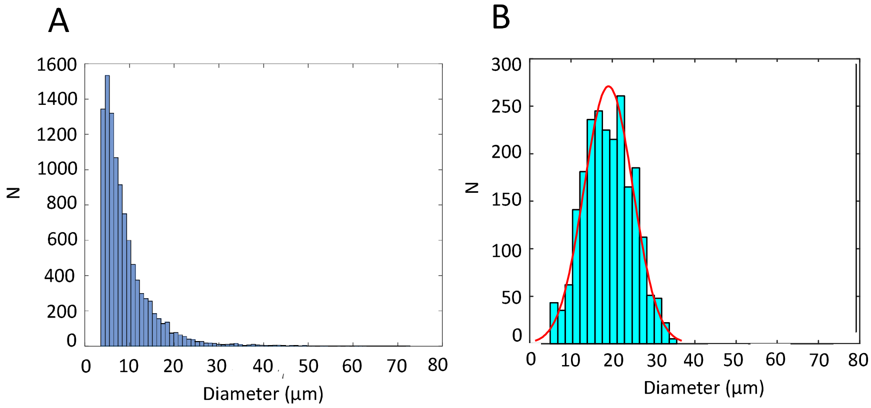

Fig. 18. A. Size distribution of electroformed vesicles, with a mean diameter of 9 ± 6 µm and a sample size of N=10000. B. Size distribution of cDICE vesicles, which follows a normal distribution with µ=19 µm and σ=6 µm. Sample size N=2500. The parameters used for cDICE vesicles are ω=350 rad/s, $d_i = 9\ \mu$m. The number of vesicles N differs significantly in both cases, since the yield of electroformed vesicles is much higher than that offered by cDICE.

The cDICE method is based on the production of aqueous droplets and forcing their passage through a liquid interface during which they eventually end covered with a lipid bilayer. The setup, which is schemed in Figure 19A, consists in a cylindrical chamber that rotates around its principal axis. Three solutions are placed sequentially inside the chamber in rotation: DAS or Dispersing Aqueous Solution, LOS or Lipids in Oil Solution, and CP or Continuous Phase. EAS is the encapsulated aqueous solution, which is injected through a glass capillary in the continuous phase. Thanks to the centrifugal force, the EAS droplet travels through the LOS phase, and gets covered with a lipid monolayer as shown in Figure 19B. When reaching the interface between the LOS and the DAS, the lipid monolayers will encounter and 'zip' into a bilayer. The newly formed vesicle is then suspended in the DAS that is collected at the end of the process.

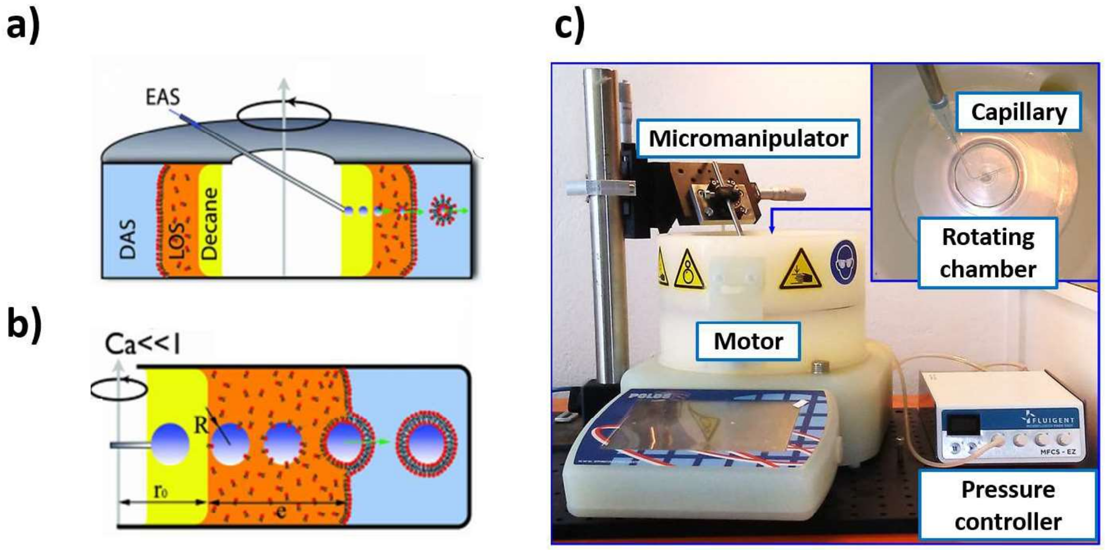

Fig. 19. A. Schematic view of a cDICE chamber displaying its different phases. B. Interface crossing by the EAS droplet through the CP, LOS and DAS. Adapted from [55]. C. Photography of the cDICE device with its different parts.

The principle for droplet production in cDICE is based on the balance between the viscous drag forces and the surface tension [122]. When injecting a liquid inside an immiscible liquid from a capillary tip, the surface tension and viscous drag forces compete. The surface tension acts by minimizing the interfacial area, leading to spherical droplets and the viscous drag pulls on the interface downstream. The capillary number Ca is a dimensionless parameter that describes the ratio between the viscous and the surface tension forces (Eq. (6)):

$$Ca = \frac{F_{viscous}}{F_{capillary}} = \frac{\eta v}{\gamma} \quad (6)$$

Where v and η are respectively the speed and the viscosity of the continuous phase, and γ is the interfacial tension between the continuous phase and the EAS droplet. In order to obtain monodisperse vesicles it is necessary that the surface tension forces dominate over the viscous forces, to prevent deformation of the EAS volume into a jet instead of a spherical droplet. So with cDICE one should always work at a small capillary number ($Ca <<1$). A scheme on how changes in Ca affect the dripping of the EAS from the capillary and thus the droplet size polydispersity is shown in Fig. 20.

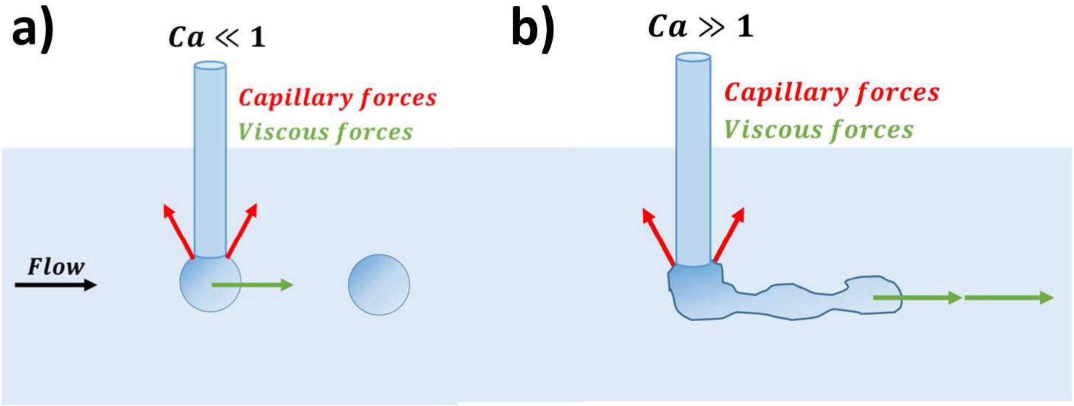

Fig. 20. Scheme describing the role of Ca on the dripping conditions and how the balance between capillary and viscous forces affect the droplet polydispersity in A. Low and B. High Ca regimes. Adapted from [121].

The cDICE setup, as shown in Figure 19C, is composed of a cylindrical Plexiglas chamber fixed on a rotating motor, a micromanipulator that allows to control the position of the glass capillary in the xyz axis, and a pressure controller. The procedure started by setting the chamber to spin at the desired angular velocity. Next, the three different phases for the interface crossing were added. The first one was the DAS or dispersing aqueous solution, which was a glucose solution 300 mOsm. The second phase was the LOS or Lipids in Oil Solution, a mixture of silicon:mineral oil at a 1:4 ratio, 6% v/v decane, 1% v/v chloroform, and 0.5% v/v of the Egg-PC or Egg-PC-biotin percentage of choice. The third phase, the CP or continuous phase in which the droplets were injected, was decane. Decane was chosen because of its small viscosity ($0.85\ mPa \cdot s$), that allows to fulfil the requirement of a small Ca. The last step consisted in injecting the encapsulated aqueous solution (EAS) in the continuous phase. The EAS was an aqueous glucose solution at an osmolarity of 300 mOsm. As mentioned before, one of the particularities of cDICE is that it allows to control the size of the vesicles which are produced with it. The vesicle size d is given by (Eq. (7)) [121,122]:

$$\frac{d}{d_i} = A\frac{1}{Ca} \quad (7)$$

where A is an empirical parameter. For similar phases, Loiseau *et al.* [121] obtained an A value of 0.11. The droplet size can therefore be controlled by tuning two parameters: d_i and Ca. The two parameters that can be adjusted to vary Ca are η and v, since the interfacial tension between the continuous and the encapsulated phase does not vary significantly. v can be changed by tuning the angular speed of the rotating chamber, which we define ω. The angular velocity will affect the time during which the droplet travels through the LOS layer, which might affect the interface saturation with lipids. It also affects the ratio between inertial and surface forces at the interface which should be kept small to prevent oil encapsulation during crossing. Consequently, the most convenient parameters to tune the vesicle size are the capillary diameter d_i and ω. Table 2 shows how the experimentally measured droplet diameter d changed when varying these two parameters

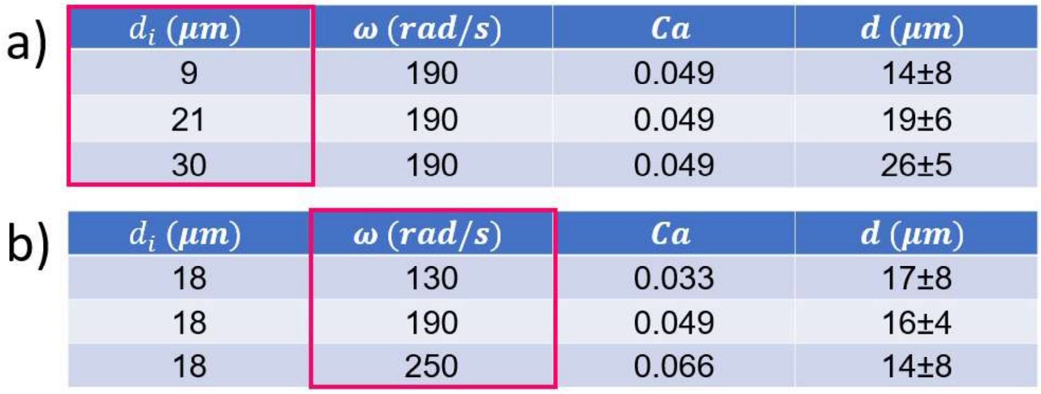

a)

$d_i\ (\mu m)$	$\omega\ (rad/s)$	Ca	$d\ (\mu m)$
9	190	0.049	14±8
21	190	0.049	19±6
30	190	0.049	26±5

b)

$d_i\ (\mu m)$	$\omega\ (rad/s)$	Ca	$d\ (\mu m)$
18	130	0.033	17±8
18	190	0.049	16±4
18	250	0.066	14±8

Table 2. A. Table displaying the experimentally measured droplet diameter d at varying capillary diameter d_i. B. Table displaying d at varying rotational speed ω.

2.2. Vesicle adhesion methods.

2.2.1. Streptavidin-biotin

As mentioned in Chapter 1, the streptavidin-biotin pair is the method we chose for driving the vesicle assembly. It is possible to change the aggregation conditions by tuning the number of streptavidin molecules in solution over the number of biotin molecules present in the vesicle membranes, noted X. By doing so we controlled the size and compaction of the vesicle prototissue.

The assembly of vesicles by using the streptavidin-biotin pair is as follows. Biotin was added to the vesicle membranes by including DSPE-PEG(2000)-biotin constructs in the phospholipid mix before starting the electroformation or cDICE process, as depicted in Figure 4, Chapter 1. The quantity of biotin was controlled by tuning the molar percentage of this reactant in the phospholipid mix and in the number of vesicles in solution. After the vesicles were prepared, the concentration of vesicles in solution was calculated by applying an ImageJ-based routine that will be detailed later in section 2.6.3. of this Chapter. With this estimation we then took the desired quantity of vesicles and diluted them in a 300 mOsm glucose solution. Texas red fluorescent Streptavidin (Fisher Scientific, 10338002), stocked at a concentration of 1 mg/ml in PBS, was added to the vesicle incubation mix at the desired quantities. The vesicles were incubated at room temperature during at least 2h before imaging. X was calculated by estimating the number of streptavidin and biotin molecules in solution. The number of biotin molecules available in the incubation mix was estimated by taking into account the average surface provided by one vesicle, the density of lipids in the vesicle surface, and the number of vesicles in solution, by using a custom-made MATLAB code. Further information on the incubation methods and the implications of X in the control of the tissue properties will be given in Chapter 3.

2.2.2. DNA tethers

In our system, we use the synthetic constructs designed by Parolini *et al.* [36] to drive the adhesion between GUVs. A graphical representation of the DNA constructs is given in Figure 5, Chapter 1. The sequences of the DNA tethers were:

- (a) 5'-GGATGGGCATGCTCTTCCCGTTTTTTATCACCCGCCATAGTAG A [Sticky End]-3'

- (b) 5'-CTACTATGGCGGGTGATAAAAAACGGGAAGAGCATGCCCATCC AAAA [Cholesterol TEG]-3'

The first 43 base pairs are complementary between sequences (a) and (b) and act as the DNAds spacer. The 9 last base pairs of sequence (a) are the sticky end, which are DNAss. The cholesterol-TEG molecule allows the inclusion of the constructs to the vesicle membrane. There is a second version of (a), called (a'), which has the same structure as (a) but contains the DNAss sequence complementary to the sticky end of (a). The complementarity between (a) and (a’) is the mechanism that drives the vesicle-vesicle adhesion. Sequence pairs (a’)-(b) and (a)-(b) are formed prior to vesicle functionalization. For the assembly, EggPC vesicles were functionalized with the DNA constructs by adding them to the incubation mix at the desired concentrations, which ranged from 32 to 644 nM. Sequences (a’)-(b) and (a)-(b) were added at equivalent volumes. The incubation mix contained IDTE pH 8 buffer, NaCl 80 mM, SYTO 64 2 µM (Thermo Fisher, S11346). SYTO 64 is a nucleic acid stain that intercalates between the DNAds base pairs and allowed the visualization of the vesicle assemblies by epifluorescence and confocal microscopy. The samples were incubated for 2h before imaging, and the energy of the interaction between DNAss sequences (a) and (a’) was calculated by using the Nucleic Acid Package software [123]. This software calculates the free energy of the secondary structure formed by two complementary DNA strands at a certain temperature and ionic conditions, which in our case was 20°C and NaCl 80 mM.

There are several remarkable differences between the streptavidin-biotin pair and the DNA tethers. The first and most notable is that DNA tethers have a total interaction energy of 18.3 k_BT , which is lower than the 35 k_BT provided by the streptavidin-biotin pair. The second is the length of the PEG(2000)-biotin versus the DNAds arm. The first is 6 nm long while the second is almost three times higher, with 14.5 nm. The extra length of the DNAds arm gives the tether a much higher mobility and ability to access a higher number of configurations, favoring the adhesion between vesicles. Also, an unpaired adenosine base is left between the DNAds and the sticky end, and four extra bases are added immediately after the cholesterol molecule to confer an extra degree of flexibility to the construct. Finally, it is also important to note the influence of the length of the carbon chain of the anchoring lipids in each construct. The longer the carbon chain is, the higher it is the anchoring of the lipid to the membrane. DSPE contains 41 carbon groups, whereas cholesterol contains only 27. The smaller length of the cholesterol molecule allows a higher degree of mobility and a higher rate of detachment and reinsertion of the DNA construct to the lipid membrane compared to that offered for the DSPE-PEG-biotin construct [30].

2.3. Active cytoskeleton reconstitution encapsulation with cDICE.

The active reconstitution that was encapsulated by using cDICE is a mixture that essentially consists in microtubules and kinesin clusters. A scheme of the components and their assembly in solution is provided in Figure 21. Microtubules are the first constituent of the mix, are also one of the main structures of the cell cytoskeleton. Their ability to polymerize and depolymerize at a fast rate makes them necessary for dynamical processes like cell movement, division, polarization, and growth [124].

They also actively participate in the transport of molecules within the cytoplasm. In the cell, they are anchored in the outer part of the nucleus in structures called centrosomes, which act as the nucleation center to start the microtubule polymerization [124]. Microtubules are formed by the assembly of tubulin monomers with GTP consumption. Tubulin subunits assemble and disassemble in both sides of the growing microtubule at different rates, which gives the filament a polarity. Due to this polarity it is possible to distinguish between the plus and the minus end, the plus end being the side of the microtubule that grows at a faster rate. The second component of the mix are kinesins. Kinesins are motor proteins that travel along the microtubule filaments towards the plus end with ATP consumption. The cytoskeleton reconstitution used in this Thesis contains kinesin clusters that consist in a pair of biotin-modified kinesins bound between each other through a streptavidin molecule. When the kinesins of a cluster bond to two antiparallel microtubule filaments, they make them slide against each other as they advance towards their respective plus ends. This movement produces an elongational stress, generating internal flows and producing topological defects that annihilate each other repeatedly in continuous motion. Apart from the microtubules and kinesin clusters, the mixture provides GTP for microtubule polymerization and an ATP regenerating system to allow the kinesins to produce energy to move. Polyethylene glycol is added to the mix to bundle the microtubules together through depletion forces.

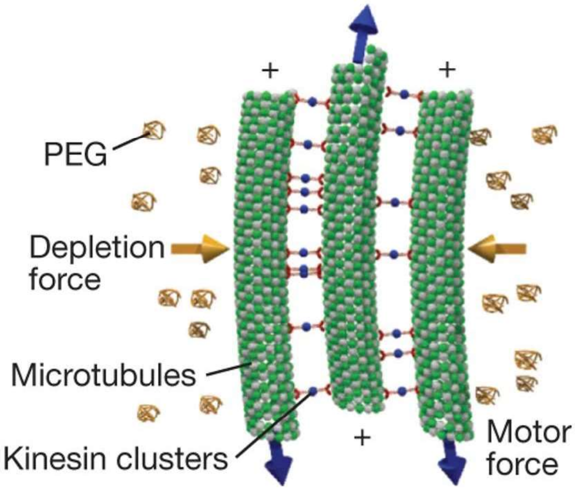

Fig. 21. Scheme of the active cytoskeleton reconstitution. From [73].

The active cytoskeleton reconstitution samples were provided by the SOCSAM laboratory (University of Barcelona) and were stored at – 80°C upon arrival. Before proceeding to the encapsulation, a test sample was imaged using epifluorescence microscopy in order to verify that the sample displayed activity. 1 µl of the mixture was added to a 5 mm PDMS well sticked at a glass coverslip with 0.5% v/v Pluronic (Sigma P2443) and covered with a silicon oil droplet. Pluronic acted as a surfactant to stabilize the interface between oil and water, allowing the mixture to form an active nematic liquid crystal phase between these two fluids. In Fig. 22 we show an example of the active sample motion recorded at different time stamps, in which we can observe the formation of topological defects. Once the activity of the sample was tested, we proceeded to the encapsulation by using the cDICE method. The LOS mixture was prepared so that the composition of the vesicle membranes was EggPC with 5% mol/mol of PE-PEG(2000) (Sigma Aldrich, 80130P). The active mixture was enriched with 10% v/v of sucrose 1M to increase the density between the vesicle interior and the dispersing aqueous solution, yielding a final osmolarity of roughly 1050 mOsm. Adding sucrose to the mixture increases the density of the droplets, which facilitates the interface crossing and is crucial for achieving a successful encapsulation. The dispersing aqueous phase consisted in a 1060 mOsm glucose solution in water, so the osmolarity difference between the inner and the outer vesicle solution was kept at +10 mOsm. A total volume of 20 µl of the active solution was injected through a glass capillary with an internal diameter of 30 µm in the continuous phase of the cDICE chamber, while it was rotating at a speed of 250 rad/s. After injection, the vesicles were collected from the outer aqueous solution, washed and kept in an observation chamber for 10 minutes to allow sedimentation. The observation chambers and eppendorfs used for handling the active vesicles and for visualizing the active solution were previously cleaned and functionalized with β-casein. The imaging was performed using epifluorescence microscopy, which was possible thanks to the fluorescently labelled microtubules with Alexa-647 ($\lambda_{absorption}$ =650 nm, $\lambda_{emission}$=670 nm).

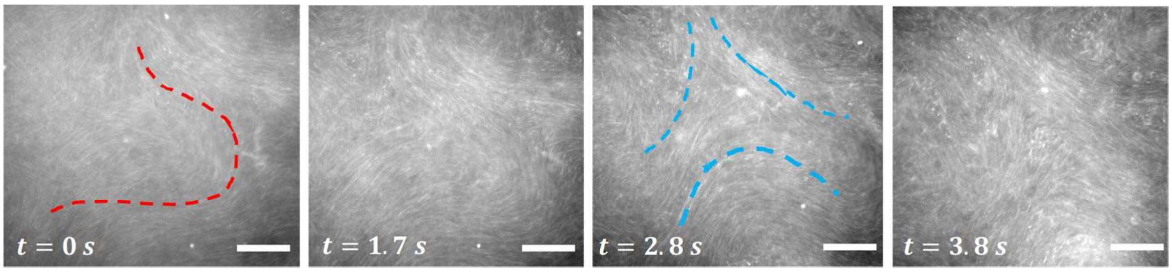

Fig. 22. Biomimetic cytoskeleton reconstitution transitioning from a +1/2 to a -1/2 topological defect. (lines in red and blue respectively). The microtubule filaments condense in the interface between the aqueous solution and the oil, displaying an active nematic behavior. When the antiparallel microtubule filaments slide against each other, they produce internal flows. Scale bar 50 µm.

2.4. Imaging methods. Optical microscopy

Optical microscopy has been evolving since the XVIII century for the observation of phenomena at the microscale. Its non-invasive nature and great variety of techniques in which it has diverged over the years has made it a very important tool for the study of living matter [125]. In this Thesis, the microscopy methods used for the visualization of the biomimetic tissue and its flow behavior are phase contrast microscopy, epifluorescence microscopy, and confocal microscopy, which will be briefly reviewed in the following subsections.

2.4.1. Bright-field and phase contrast microscopy.

Bright field imaging is based on the difference in how the light is transmitted through the different parts of a sample, which is determined by the differences in their refractive index. Biological samples are mainly composed by water; therefore, the differences in the refractive index are very small or inexistent. Phase contrast microscopy (PhC) was developed in order to magnify the differences in the refractive index of the samples and make them visible to the human eye. A representation of a Phase Contrast microscope and its optic path is provided in Figure 23A. It is worth noting that the majority of microscopes used for biological samples imaging are inverted, which means that the objective is placed under the sample. This allows to image the sample in *in vivo* conditions, since cells or tissues can be kept in a glass coverslip or petri dish with culture medium open at the top. The microscope used for our experiments was a LEICA Inverted phase contrast microscope (DMIRB, Leica) with objectives ×10 (NA = 0.25) or ×20 (NA = 0.4). The images were obtained by using a Hamamatsu camera (C13440 ORCAflash 4.0).

2.4.2. Epifluorescence and confocal microscopy.

Epifluorescence and confocal microscopy are based on the phenomena of fluorescence. Fluorescence is the emission of light at a certain wavelength by molecules that have been previously excited. Upon excitation, electrons increase their energetic state, and when they return to their initial, low-energy state, the excess energy is emitted as photons. The wavelength of excitation is shorter and therefore more energetic than the wavelength of emission [126]. Fluorescence-based microscopy provides an excellent platform for visualizing living matter, both *in vivo* and *in vitro*, because conventional chemical staining methods might result in the death of the specimen or in loss of its structure and function. By genetically encoding fluorescent probes, biotechnologists have developed methods to label the different biomolecules from cells and tissues in a non-invasive way. Another important

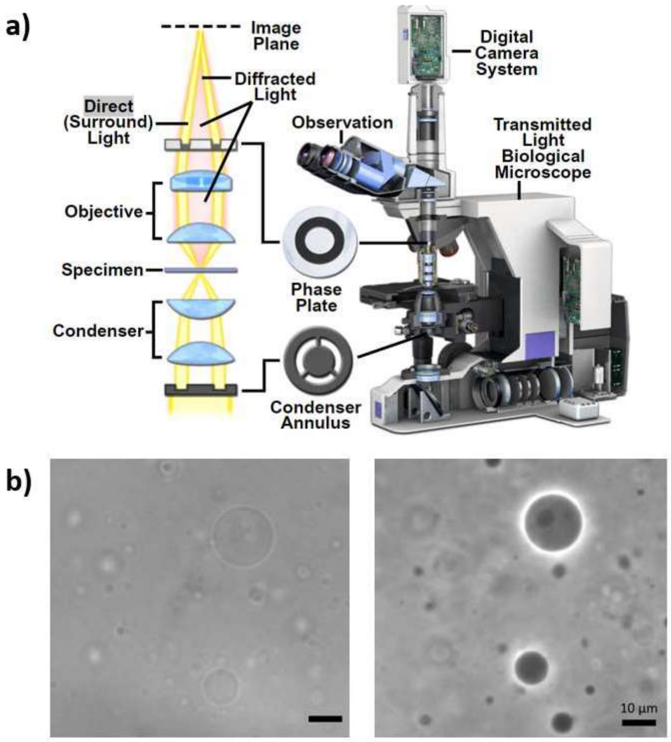

Fig. 23.A. Structure of a phase contrast microscope. Light coming from the light source passes through the condenser annulus and gets focused by the condenser lens. As it reaches the specimen, the light passing through it gets refracted, changing the angle in which it hits the objective lens. The phase plate shifts the phase between the refracted and non-refracted light, creating a phase difference that is visible for the observer. Adapted from [127]. B. Photo of GUV sample in bright field (left) and phase contrast (right). The inner part of the vesicles is filled with a 290 mOsm sucrose solution and the media is a 300 mOsm glucose solution.

feature of fluorescence microscopy is that it is possible to correlate the concentration of a fluorophore in solution with the detected fluorescence intensity, enabling absolute quantification of molecule concentration in the sample. A graphical schema of the structure of a widefield epifluorescence microscope is provided in Figure 24A. In epifluorescence microscopy, a filter selects the light with a wavelength in a range containing the excitation wavelength of the fluorophore. This filtered light passes through the objective upon reflection by a dichroic mirror until it finally hits the sample. The parts of the sample which contain the fluorophores emit light at a higher wavelength. The light passes again through the objective lens until reaching the emission filter, that filters out all the wavelengths that do not belong to the fluorophore´s emission spectrum. But even though fluorescence microscopy is a very relevant tool for molecular biology research, it does not come without some drawbacks.

Fluorophores are organic molecules, and after excitation they can interact with oxygen molecules in the environment and become reactive oxygen species (ROS). In this state they lose their fluorescent properties, a phenomenon known as photobleaching. These photobleached molecules are highly reactive and can damage DNA, proteins and fatty acids impairing their normal functioning [128]. Another important inconvenient of epifluorescence microscopy is the amount of out-of-focus light emitted by the sample after fluorophore excitation. Confocal microscopy is a technique that was later developed that helped to ease these issues. Confocal microscopy operates with a laser laser light that is focused onto a defined position of the sample. Thanks to a pinhole, only the light emitted by the excited fluorophores of the illuminated focal plane will be recorded by the detector. A depiction of a confocal microscope is shown schematically in Figure 24B. By illuminating a significantly smaller volume of the sample, the amount of irradiated molecules diminishes, and so does the photobleaching of the sample. The collection of the emitted light through a pinhole avoids the blurring of the image by out-of-plane light. Another application of the confocal microscopy is the possibility to perform tridimensional images of the analyzed samples. An image of each plane of the sample can be recorded by displacing the laser position in the z direction. If the overlap between the two planes is high enough, it is possible to integrate all the images into one 3D-reconstruction. This task is performed by specialized commercial software, and it enables to obtain quantitative information on the size and morphology of the sample such as its area, volume, or sphericity.

In the presented work, epifluorescence imaging was performed with the same inverted microscope and camera used for the phase contrast imaging. The source of light was provided with a CoolLED pE-300 white LED lamp. For the confocal microscope imaging, a Zeiss microscope (Zeiss LSM880) with a ×40 objective (water immersion, NA = 1.1) with a spatial resolution in xyz of 0.21 μm x 0.21 μm x 1 μm was used. The confocal microscope is available at the Montpellier Ressources Imagerie (MRI) platform. The fluorophores used for our samples are Texas-red labelled Streptavidin, which has a wavelength of absorption/emission of 560 and 583 nm, and NBD-labelled phospholipids, with emission/absorption wavelengths of 460/535 nm. Carboxyfluorescein-labelled DSPE-PEG(2000) and DSPE-Rhodamine molecules were also used, with an emission/absorption spectra of 460/515 nm and 560/583 nm respectively. Signal acquisition was performed with two detectors: gallium arsenide phosphide (GaAsP) and photomultiplier tube (PMT), used respectively for an Argon laser ($\lambda = 488$ nm), and for a He/Ne laser ($\lambda = 633$ nm). The 3D reconstruction of the image stacks and the quantification of the aggregates' size and shape was performed with the commercial software IMARIS by Oxford Instruments, and the Cell plugin was used for individual vesicle segmentation and mapping.

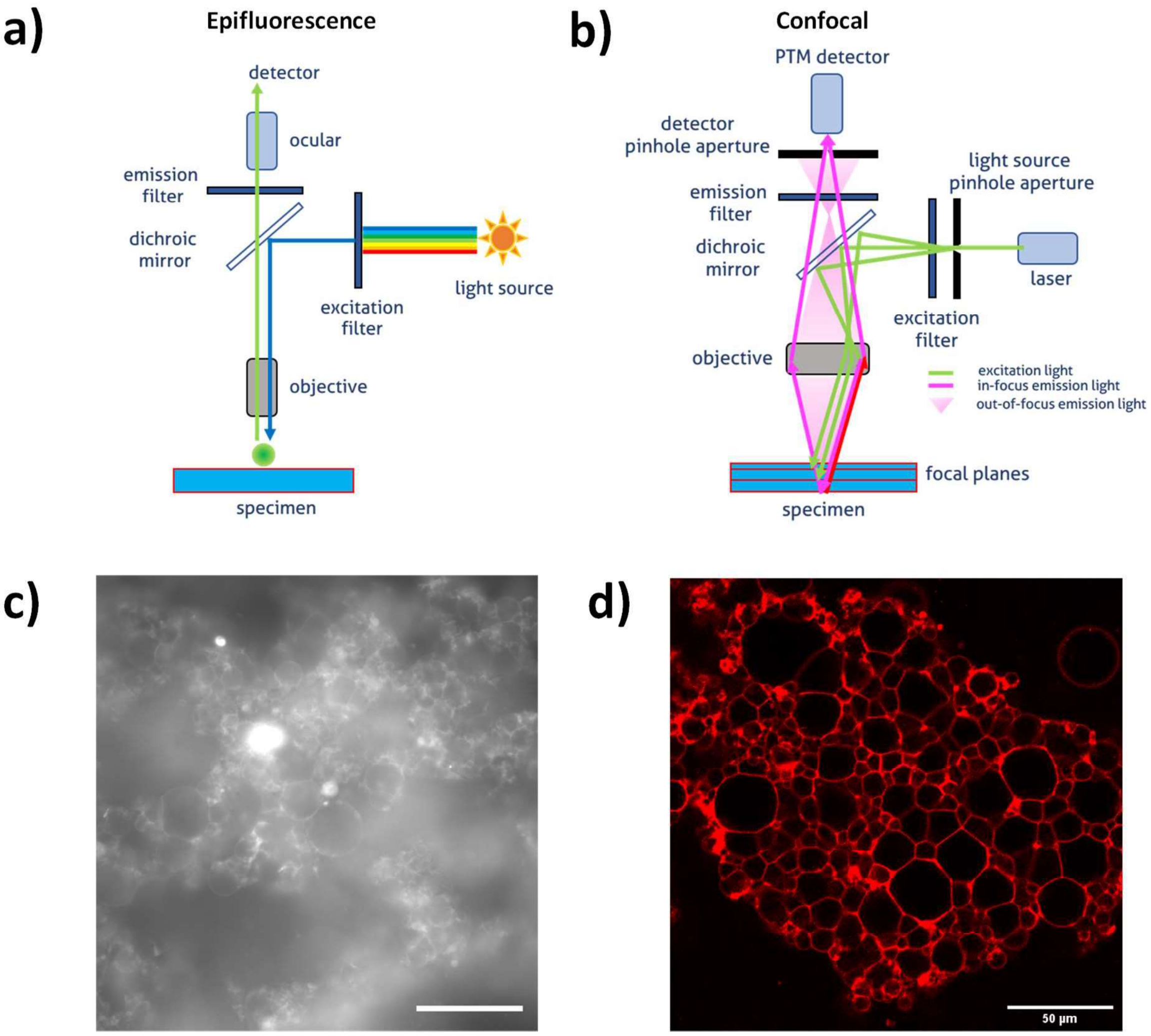

Fig.24. A. Schematic drawing of an epifluorescence microscope. B. Schematic drawing of a confocal microscope. From [129]. C. Biomimetic tissue under epifluorescence (left) and confocal (right) microscopy. Epifluorescence microscope collects the out-of-plane fluorescence od the sample, leaving a lot of out-of-focus light that blurs the image (left). Confocal microscope scans the sample plane by plane, so only the in-focus light passes through the detector pinhole. An image of each plane of the sample is obtained after passage through the detector (right). In both images, fluorescence is provided by Texas Red Fluorescent Streptavidin, whose maximum absorption wavelength is 596 nm and its maximum emission wavelength 615 nm.

2.5. Microfluidics.

2.5.1. Chip fabrication.

The microfluidic chip is a device, usually made of PDMS, which enables the processing of micrometric amounts of liquid and has microscopic channels with controllable geometries imprinted in their surface. The space between the channels and the outside is sealed thanks to the irreversible bonding of a glass coverslip, which also facilitates its visualization by optical microscopy. For the experiments of this Thesis, the microfluidic chip used had the shape and dimensions displayed in Figure 25. The geometry consists in a central constriction with the inlet for the liquid in the right part of the channel and the outlet in the left side of the channel. The entrance of the constriction has a 45° funnel geometry to avoid the trapping of bubbles in the corners of the channel. The width of the constriction W_c was 50$\pm$2 µm. The size was chosen so it would be small enough to deform the sample, yet large enough to test the rheological properties of the whole aggregate and not those of single vesicles. In the next sections a detailed description of the steps followed to produce the microfluidic chips is given.

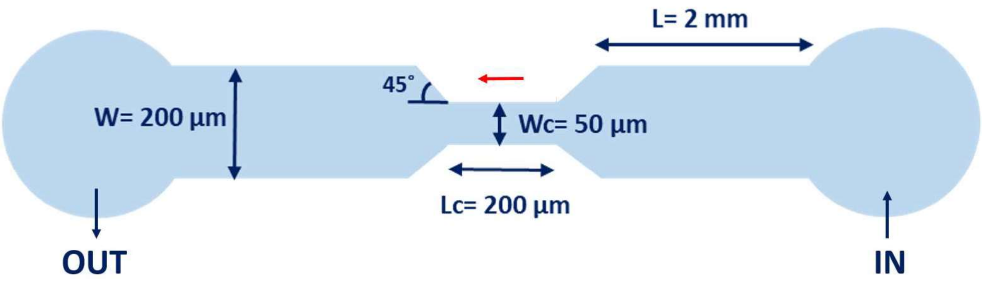

Fig. 25. Sketch of the geometry of choice for the microfluidic aspiration experiments. The height of the channel is 40 µm. The red arrow indicates the direction of the flow. Drawing not to scale.

The type of stress provided by the geometry of the microfluidic chip is a mixture of shear and elongational, as depicted in Fig. 26. In the parallel parts of the channel, the flow velocity profile of a Newtonian fluid has a parabolic shape, which is also known as Poiseuille profile. In these conditions, the maximum value of the flow velocity is found in the midsection of the channel and gradually decreases until reaching the walls, in which velocity should be equal to 0 (non-slip condition). As the fluid approaches the funnel and the width of the constriction becomes smaller, the velocity at the center of the channel along the flow direction increases, leading to an elongational flow. A mixture of shear and elongational stress exists in the intermediate region between the funnel walls and the center of the channel. Once the liquid is streaming inside the constriction, the regime goes back to simple shear.

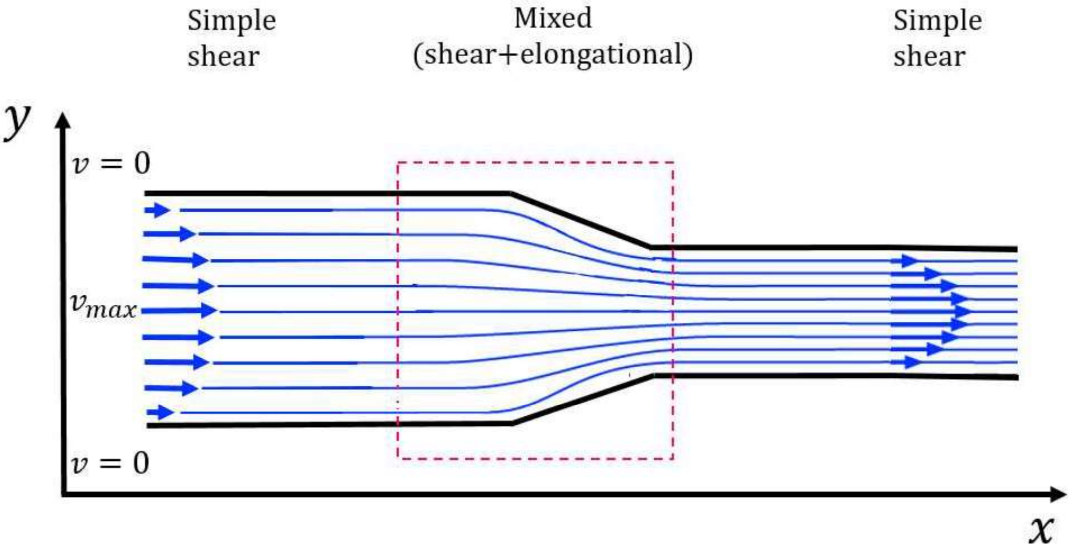

Fig. 26. Schema of the flow behavior of a Newtonian fluid inside a funnel-shaped microfluidic constriction. Illustrative streamlines and velocity profiles are depicted. Adapted from [130].

Photolithography

The first step in the microfluidic chip fabrication was to build the template with the desired channel geometries. For that, the channel geometry was printed on a silicon wafer by using photolithography. It consisted in shining UV light through a mask with the desired channel geometries on top of the wafer, after having covered it with a photosensitive resin, as shown in Figure 27A, steps 1 to 3. Upon UV light exposure, the photosensitive substrate hardened and the rest was washed away, giving a template with the desired micropattern. For our experiments, the photolithography was already made so the chip fabrication procedure started with the soft lithography step.

Soft Lithography

The next step consisted in replicating the structure printed on the silicon wafer using a soft, elastomeric polymer in a process called soft lithography, which is depicted in Figure 27B [131]. The elastomer was Polydimethylsiloxane (Sylgard 184 Dow Corning), which was obtained by mixing the Base elastomer and the Curing Agent at a 1:9 ratio. The mixture was poured on top of the master and degassed to eliminate the bubbles that formed during the mixing process, and was left in the oven at 70º C for a minimum of 4h. After this time, the mixture had reticulated and the result was a flexible but solid block of PDMS with the desired channel geometry imprinted on it, that could be easily detached from the master.

Plasma bonding

Once the PDMS channels were made, they were irreversibly sticked on a glass slide by a plasma bonding procedure, as shown in Fig. 27C. This provides them physical support as well as a means to properly visualize the aggregate aspiration process with optical microscopy. The plasma bonding protocol consisted in activating the surface of the glass slides using an oxygen plasma assisted chamber at a pressure of 500 mTorr (Harrick Plasma PDC-32G-2 (230V)). In these conditions, the oxygen molecules oxidizes the SiO_2 groups in the surface of the glass so they become reactive ($SiOH$). After the treatment, the glass was immediately placed against the PDMS so the activated surface reacted with the $SiOH$ groups form a covalent bond ($Si - O - Si$). The last step consisted in heating the assembled chip for 5 minutes at 70ºC to enhance bond formation.

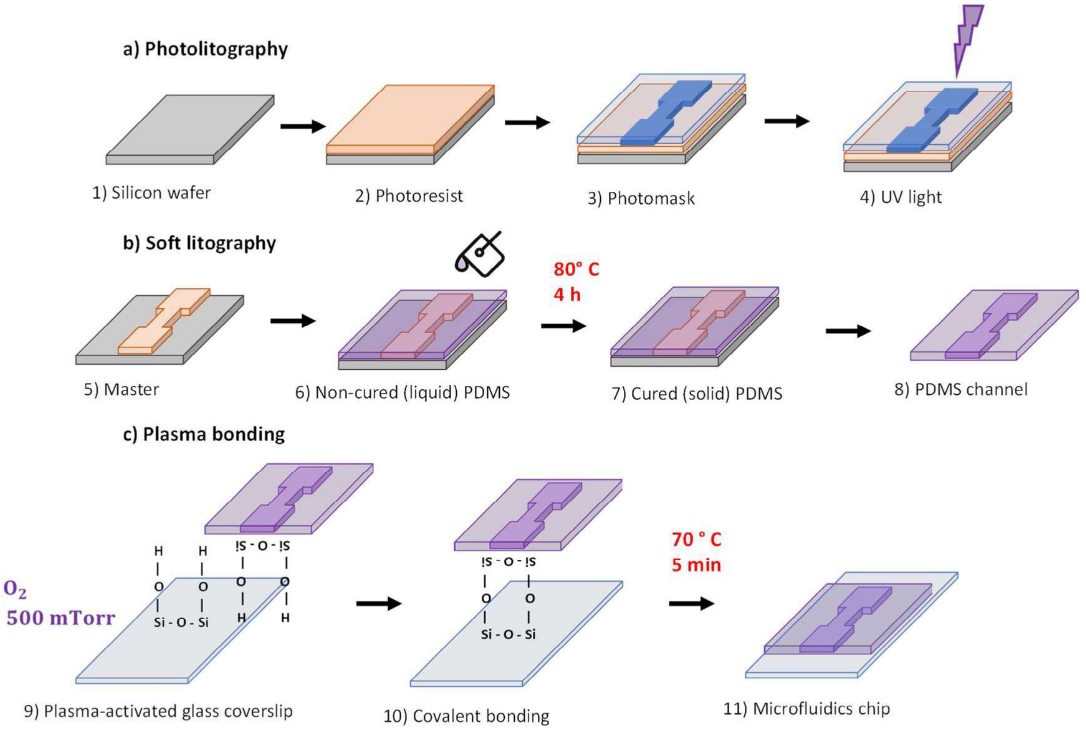

Fig. 27. Drawing of the three different steps employed for the microfluidic chip fabrication a) Photolithography, b) Soft lithography, and c) Plasma bonding. Adapted from [132].

2.5.2. Setup for aspiration experiments

The experimental device used for microfluidic aspiration was similar to the micropipette aspiration technique, which has been mentioned in Chapter 1. A graphical depiction of the setup is provided in Figure 28. In the experiments, the aggregates were placed inside a 100 μL reservoir in the inlet of the microfluidic chip with a 300 mOsm aqueous glucose solution containing 0.5 μm diameter particles (1) at a concentration of 0.5 % v/v (S37494 Invitrogen/Thermofisher scientific), which enabled to track the direction and velocity of the flow. Both aggregates and particles flowed from the inlet to the outlet of the microfluidic chip (2) by applying a pressure difference between these two points, and the aggregate experienced a deformation as it passed through the constriction. This pressure drop was provided by the balance between a positive and a negative pressure difference. The positive hydrostatic pressure was provided with a water column (3) placed at a certain height above the aggregate reservoir, which could be controlled by changing its height through a micrometric screw (4). The negative pressure was provided by a pressure controller (5) (MFCS-EZ by Fluigent) connected to a vacuum pump (6). The precision of the micrometric screw and the pressure controller was of $\pm$ 0.001 mbar and $\pm$ 0.01 mbar respectively. The water reservoir was connected to the pressure controller and to the microfluidic chip by means of a tubing system which was made of teflon and had a diameter of 0.5 mm (Scientific Commodities Inc., #BB311-24). The aspiration process was visualized by using an inverted microscope in phase contrast or epifluorescence mode (7), with objectives ×20 (NA = 0.4) and recorded with a Hamamatsu camera (8) (C13440 ORCA-flash 4.0). The camera enabled the tracking of the aggregate with time as it flowed through the constriction. The time between each frame of the sequence was equal to the exposition time. The typical frame rates for the phase contrast microscopy experiments was 80 frames per second (fps) and 5 fps for the epifluorescence ones. The maximum frame rate of the camera was 100 fps.

Aspiration protocol

Before starting the experiments, the pressure applied to the system was set to zero. To do so, the negative pressure provided by the controller and the positive pressure provided by the water column were manually adjusted until no flow in the channel was observed, making sure that the seeding particles were nearly at rest. The height and pressure were noted and set as $\Delta P = 0$. In order to perform the aspiration experiments, the aggregates were placed inside the channel through a micropipette tip inserted in the inlet of the chip. Then, the aggregates were aspirated towards the entrance of the constriction. We distinguish between two different protocols depending on how the pressure was applied: *Constant* pressure, or *Increasing* pressure steps. In the first protocol, the

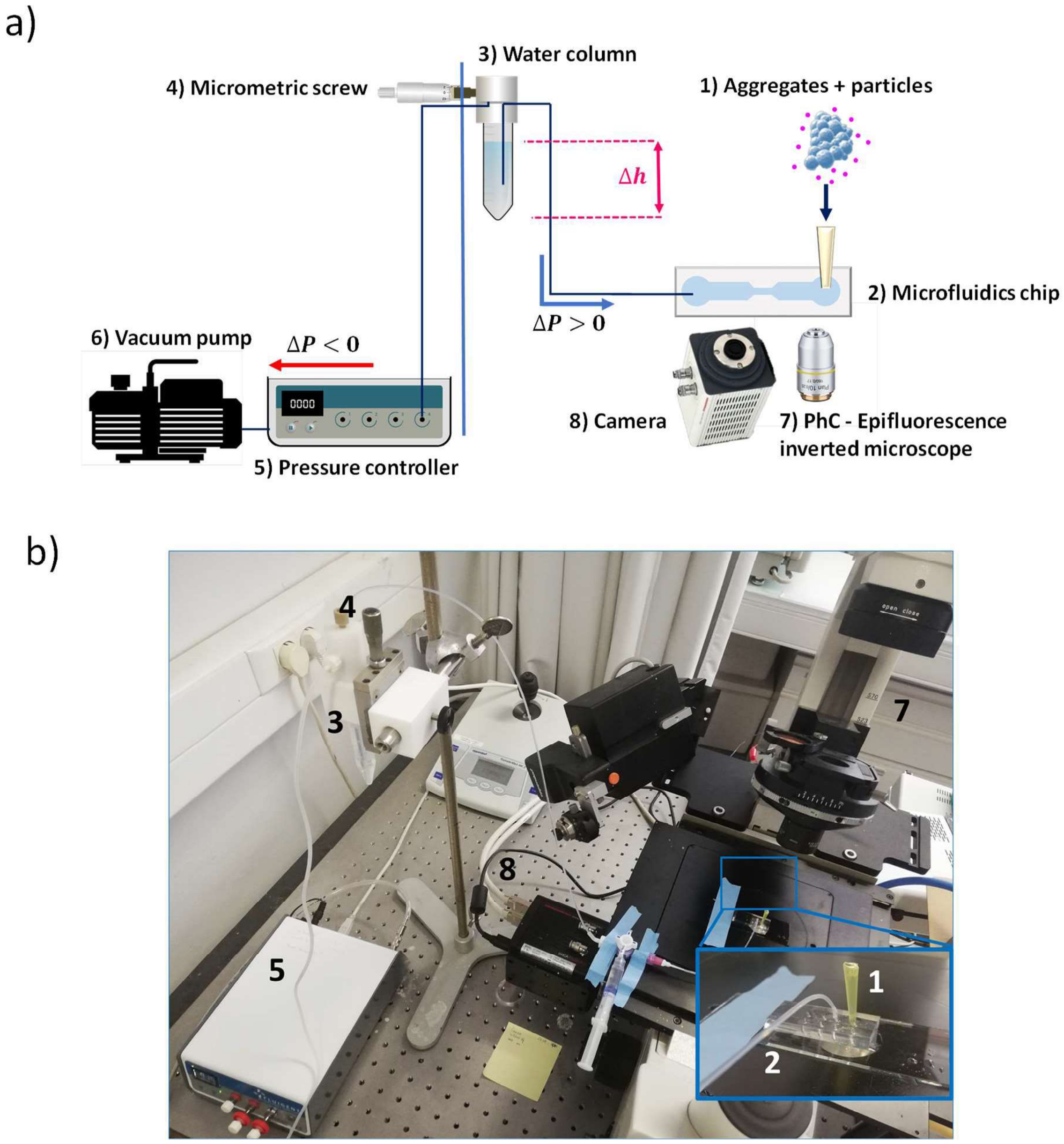

Fig. 28. A. Drawing of the microfluidics aspiration setup. B. Photography of the setup. 6, which is the vacuum pump, is not visible because it is located in another room.

pressure was increased manually in steps of 0.02 mbar until we observed that the aggregate started flowing inside the constriction. This value was set as the passage pressure (ΔP_{pass}). The pressure was set back to zero in order to bring the aggregate away from the constriction. Next, the pressure was increased to the ΔP_{pass}, which was kept constant during the aspiration experiment. This protocol was used to characterize the flow properties of aggregates with sizes comparable to that of the constriction width W_c . For larger aggregates, however, this protocol did not enable the aggregate to flow and exit the constriction; for this reason, we imposed increasing pressure steps. In this second flow protocol, the pressure was increased automatically with the pressure injector controller (Fluigent) in steps of 0.05, 0.1 or 0.2 mbar (starting at 0 mbar) every 10 s. The Fluigent Automation software allows to program automatic pressure changes for the pressure controller at regular time intervals: the duration of the step, its shape, amplitude and the number of repetitions were set by the user prior to the start of the protocol. The software also produced a file with the applied pressure values in real time with a resolution of 0.05 s. When the aspiration experiments were recorded, the camera software kept the start time of the recording with a precision of 1 s. By matching the information obtained with the pressure controlling software and the camera we were able to synchronize the applied pressure with the deformation of the aggregate, within an uncertainty of 1 s.

2.6. Image analysis

2.6.1. Vesicle count

In order to control the size of the vesicle aggregates and to get reproducible results, it was necessary to control the concentration of vesicles used for the assembly assay. Since the number of vesicles per unit volume produced for each batch of electroformation or cDICE was different, it was necessary to develop a method to count the vesicles. This allowed us to adjust the vesicle concentration to a reference concentration for each assembly experiment, thus making the aggregate production reproducible and controllable in size. To do so, we used 10 μL of the vesicle electroformed solution that we put in an observation chamber, previously filled with an aqueous glucose solution 300 mOsm. The sucrose-filled vesicles sedimented down to the bottom of the chamber, and they were visible through phase contrast microscopy, as shown in Figure 29A. We considered the vesicle distribution throughout the chamber was homogeneous. Five images of different regions of the chamber were taken in order to have a representative number of vesicles, and we applied a custom-made ImageJ routine treatment in order to extract the number of vesicles per image and their size distribution. The ImageJ treatment consisted in enhancing the contrast and the edge definition between the vesicles and the outer media, which facilitated the binarization of the image, as displayed in Figure 29B.In the binarization process the pixels of the image were classified depending on their intensity, and they were assigned a new pixel intensity of 0 (white) or 255 (black), as shown in Figure 29C. This last step allowed the routine to recognize the objects of the image whose pixel intensity was 255 and to extract a file with the number, area and coordinates of each vesicle as shown in Figure 29D. From the data obtained from each of the five images we estimated the number of vesicles per microliter, assuming a homogeneous distribution of vesicles in the solution. Calculating the number of vesicles and their size distribution allowed us to estimate the number of biotin molecules present in the vesicle's surface, which was necessary in order to calculate X.

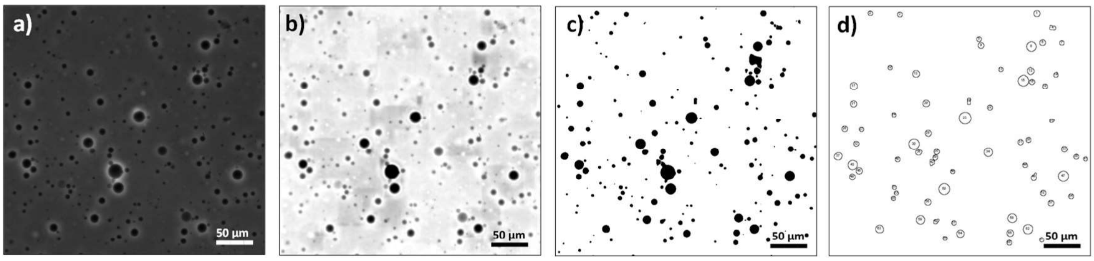

Fig. 29. Steps of the vesicle count ImageJ routine. A. Original phase contrast image. B. The Subtract Background and Bandpass Filter commands allow to smooth the background and to blur the objects that were below a certain size threshold (3 pixels in this image). C. Binarized image. The vesicles were assigned a pixel intensity of 255 and the background had a pixel intensity of 0. D. Object count. Each identified object in the count process is assigned a number, which allows its identification in the image. Objects below 2.5 µm radii and a circularity below 0.7 were excluded from the count to avoid identification of lipid debris. The vesicles displayed in this figure have been obtained through electroformation.

2.6.2. Radial profile analysis

The Radial Profile analysis tool provided by ImageJ allowed us to quantitatively assess the membrane fluorescence intensity. We used this analysis for two different purposes. First, we wanted to verify the incorporation of biotinylated lipids in the vesicle membrane. For this we prepared vesicles with a fluorescent analog of DSPE-PEG(2000)-biotin, which replaces biotin with a carboxyfluorescein group. Second, we quantified the fluorescence intensity of streptavidin molecules bound to the biotinylated lipids of the vesicle membrane. The fluorescence intensity from SA was measured both on the vesicle membrane and adhesion patch between adjacent vesicles forming vesicle doublets. The first part of the Radial profile Analysis consists in selecting a circular region of interest in an image, which in our case are fluorescent vesicles, as shown in Fig. 30A. The program then plots the integrated pixel intensity as a function of the distance to the center of the circle, as shown in Figure 30B. The pixel intensity values were divided by the perimeter of the circle, giving normalized values. Afterwards, the pixel intensity was integrated over the membrane width by using a MATLAB routine in order to obtain the absolute fluorescence intensity for each vesicle. This functionality allowed us to calculate the normalized pixel intensity of the transversal section of vesicles imaged by confocal microscopy, and the fact that the values were normalized enabled the comparison between vesicles of different sizes.

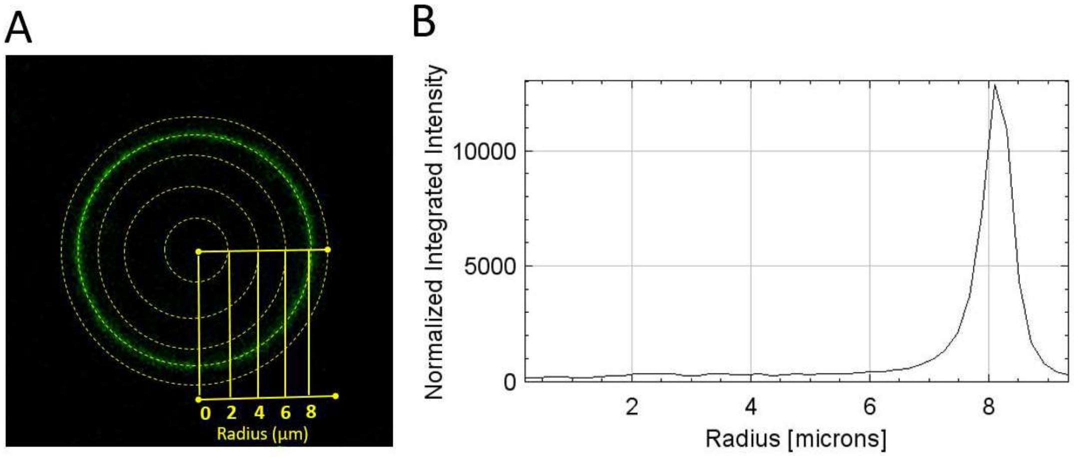

Fig. 30. A. Radial profile analysis with ImageJ in a transversal cut of a vesicle, imaged by confocal microscopy. B. Normalized integrated pixel intensity as a function of the vesicle radii. Each point of the graph corresponds to the sum of intensities of the pixels at a certain distance from the center, indicated by the yellow discontinuous lines in Figure A. All values are normalized by the perimeter of the circle.

2.6.3. Image analysis of the aspiration experiments.

In the aspiration experiments, vesicle aggregates flowed through the channel constriction upon the application of an external pressure. They advanced through the constriction forming a protrusion with a width equal to the constriction channel width, W_c , as shown in Fig. 31. We defined W_{agg} as the width of the aggregate orthogonal to the direction of the flow, and we used the ratio W_{agg}/W_c to express the normalized size of the aggregate. W_{agg} was the height of the smallest rectangle that enclosed the area of the aggregate just before entering the constriction. The forward displacement of the aggregate ΔL with time was measured as the difference between the position of the protrusion front inside the constriction L at time t and the entrance of the constriction, L_0. The advancement of the aggregate was recorded by a camera and the output was an image sequence with a known time interval between frames. The evolution of the protrusion length in time allowed us to compute the characteristic relaxation time of the prototissue, its viscosity and elastic modulus. Also, by tracking

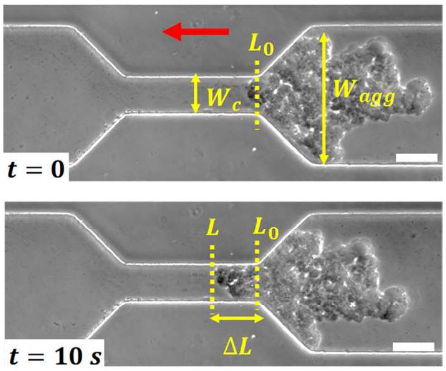

Fig. 31. Aggregate flowing through a constriction with width W_c at a constant pressure for a time interval of 10 s. The red arrow indicates the direction of the flow.

the velocity of the advancing front, we were able to calculate the hydraulic resistance of the aggregate. In order to analyze the images, we stablished an image treatment protocol. This protocol combined custom-made ImageJ and MATLAB routines and also ILASTIK, a deep learning image segmentation software. The image sequence, obtained by phase contrast or epifluorescence microscopy, was first treated with ImageJ in order to smooth out objects below a certain size threshold that might add noise to the image, and the borders of the channel were removed in a semi-automatic way, as shown in Figure 32A, steps a) to c). The image was rotated so the channel constriction was placed horizontally. The second part of the image treatment protocol consisted in segmenting the images. Segmentation is a process that classifies the pixels of an image depending on their intensity, texture, or color, and assigns them a new intensity value. For our images, the pixels were classified in two different categories: the pixels that belong to the aggregate, and the pixels that belong to the microfluidic channel. This allowed us to identify the aggregate as a single object and track its advancement and deformation along the image sequence. This classification of the pixels of the image was performed using the ILASTIK software. Since the intensity and colour of the pixels belonging to the aggregate and to the channel was very similar, we separated them based on differences in texture. Both classes of pixels were manually identified by marking the aggregate as one class of pixel, highlighted in yellow in Figure 32A d), and by marking the background as a different class of pixel, indicated in blue in the same Figure. This allowed the program to train itself to recognize the marked regions as different types of pixels and to classify them accordingly, as depicted in Figure 32A e). Once the program was trained, the classification algorithm was applied to the whole image sequence. In image sequences obtained by epifluorescence, the intensity of the aggregate was significantly different than that of the background. Therefore, the pixels were classified according to their intensity level as shown in Figure 32B. The next step consisted in binarizing the image by using ImageJ and to apply several functions that helped enhancing the quality of the segmentation, such as eroding the edges and filling the holes inside of the aggregate that had been recognized as part of the background. With this step, the pixels belonging to the aggregate were assigned an intensity value of 255 and the pixels of the background an intensity value of 0, as shown in Figure 32 A step f). Next, the Erode function was applied so the edges of the channel would diminish its size and separate into smaller, individual objects as depicted in Figure 32 A step g). The last step of the image treatment consisted in eliminating these individual objects by using the Analyze Particles tool provided by ImageJ. The tool filtered any object that was smaller than the aggregate, leaving only the aggregate in the image as displayed in Figure 32A step h). In the end, we obtained a data file with the coordinates of the center of mass, area, perimeter and circularity of the aggregate for each frame. For the large aggregates in which we wanted to measure the evolution of the protrusion length inside the channel constriction over time, we extracted the XY coordinates of every pixel of the aggregate for every frame of the stack in separate text file. Next, we applied a MATLAB routine that allowed us to identify the pixels corresponding to the advancing front of the aggregate inside the constriction and average them to get the mean position of the aggregate protusion front.

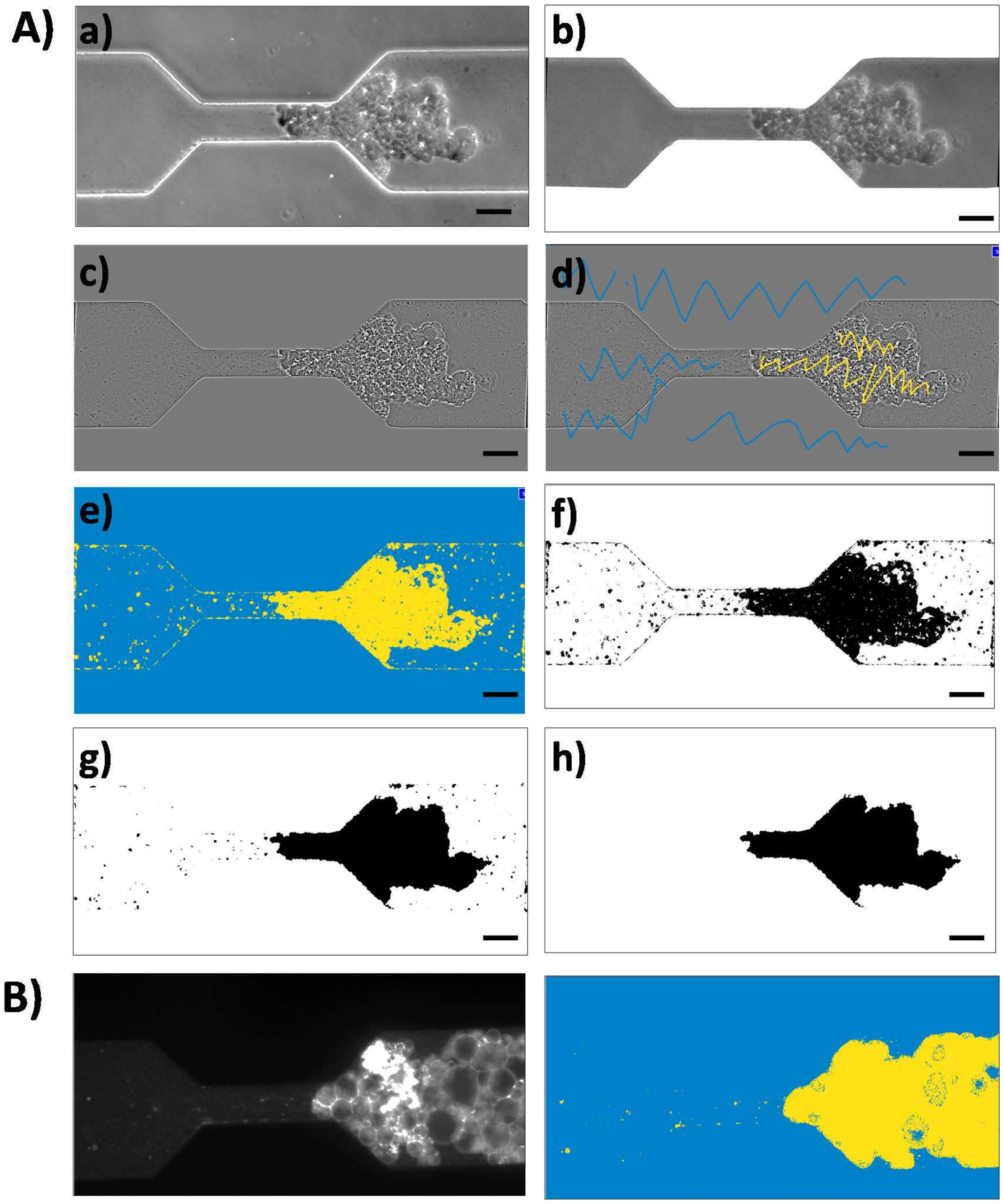

Fig. 32. A. Steps of the image treatment process. a) Original phase contrast image. b) Channel edge removal. c) Application of Convolve and Bandpass filters to increase the edge contrast of the aggregate and smooth out objects smaller than 10 pixels. d) Manually highlighting the regions corresponding to the aggregate (yellow) and to the background (blue). e) Pixel classification depending on their texture. f) Binarization of the image, in which the aggregate pixels are assigned a value of 255 and the background pixels are given a value of 0. g) Erosion of the channel edges and filling the holes inside of the aggregate. h) Filtering objects that are smaller than the aggregate. B. Epifluorescence image of an aggregate flowing through a constriction before (left) and after ILASTIK segmentation (right). The pixels are classified according to their intensity.

Chapter 3. Assembly of vesicle prototissues.

3.1. Conception of a vesicle prototissue.

In this Chapter we present an overview of the main results obtained for the controlled assembly of a biomimetic prototissue. This work has been published in *Soft Matter, 2021,17, 5061-5072* and is included in the end of this Chapter. The constituting units of the biomimetic tissue are giant unilamellar vesicles, and the mechanism to drive the assembly is based on the streptavidin-biotin pair. An assembly method based on the complementarity between DNA base pairs was employed as well, but only for comparative purposes. By changing the type and concentration of ligand, the incubation method, and the quantity of vesicles that we added to the preparation we were able to control the size, morphology and degree of compaction of the tissue. Biomimetic tissues with tunable mechanical properties are a valuable tool for understanding the role that the different components of cellular tissues such as adhesion molecules, cell cortex or cell membrane play in the assembly of cellular tissues.

The first parameter that we aimed to control was the size of the vesicle aggregates. We first controlled the aggregate size by changing the number of vesicles in solution, with which we obtained a range of aggregate volumes that went from $10^4\ to\ \ 10^8\ \mu m^3$. The aggregates were polydisperse and irregular in shape. Next, we tuned the aggregate size by changing X, as well as the biotin percentage in the vesicle membranes. By varying X, we obtained aggregates ranging from $10^3\ to\ \ 10^5\ \mu m^3$. Varying the biotinylated lipid molar percentage in the membranes enabled us to form aggregates that went only from $10^4\ to\ \ 10^5\ \mu m^3$. From the three methods, changing the total number of vesicles in solution was proven to be the most effective way to tune the size of the vesicle aggregates.

The next parameter that we aimed to control was the adhesion between the vesicles forming the aggregate. We achieved this objective by changing the biotinylated lipid molar percentage on the membranes and X. Quantitative measurements on how these two parameters affect the degree of adhesion between vesicles were performed in vesicle doublets, by measuring the contact angle between vesicles. We showed that by increasing X it was possible to increase the degree of adhesion between vesicles. However, if X was increased above a certain value, the contact angle between vesicles diminished. For a given X value, the contact angle varied depending on the biotinylated lipid molar percentage in the vesicle membranes: for vesicles with a high concentration of biotinylated lipids, the contact angle reached values up to 6 times larger than that found on vesicles containing a low concentration of biotinylated lipids.

The degree of cohesion was compared in both streptavidin-biotin and DNA adhesion-mediated vesicle aggregates by measuring the contact angle of the vesicles found in the outer side of the aggregate. In streptavidin-biotin aggregates, it was found that by changing the biotinylated lipid molar percentage in the vesicle membrane from 2.5 to 10% it was possible to change the contact angle between vesicles by 20°. In DNA adhesion-mediated aggregates, by varying the DNA tether concentration it was possible to achieve differences in the vesicle contact angle by 40°, and also to reach very high contact angles, up to 70 °. The last feature we wanted to control was the morphology of the aggregates. For this, we changed the method of incubation in which the aggregation of biotinylated vesicles occurred. In the presence of gravity as the main driving force, vesicles aggregated in a tridimensional structure. In order to achieve flat, 2D tissue-like structures, the incubation was performed inside of an incubation chamber and a slow in-plane rotation was applied, which favored the vesicle-vesicle encounters. Interestingly, the organization of the aggregates incubated by using this method resembles that of an epithelial tissue monolayer.

3.2. Aggregate size evolution with time.

In order to tune the physical properties of our biomimetic tissue it was necessary to set the incubation time period for vesicle assembly. We wanted to check that the resulting aggregate size did not vary significantly for the chosen timescale. For this, we incubated the vesicles for different incubation times: 0, 10, 30 minutes, 1, 2, 5, 15, 24, and 48 hours. In order to quantify the size of the aggregates, the 2D projection of the aggregate´s area was measured in images obtained by phase contrast microscopy. The number of aggregates averaged per time point was between 50 and 90, from a total of 3 different experiments. The vesicles contained 10% mol/mol biotin in the membrane and the streptavidin to biotin ratio was fixed at X=0.45. We performed the experiments at different time points in two different incubation conditions: Sedimentation (S) and Concentration (C). In the sedimentation method, a volume of vesicle solution in sucrose 290 mOsm was mixed with 1.5 times its volume of glucose solution 300 mOsm and the desired quantity of streptavidin. Due to the density contrast between glucose and sucrose the vesicles sedimented in the bottom of the Eppendorf thanks to gravity, bringing them together and enhancing the encounter between biotinylated vesicles. In the concentration method, the vesicle solution was mixed with 1.5 times its volume of glucose solution and centrifuged at 7g for 30 minutes. Afterwards, a part of the solution was removed until only 10 µl of solution are left. Next, the streptavidin was added. The diminished volume increased the

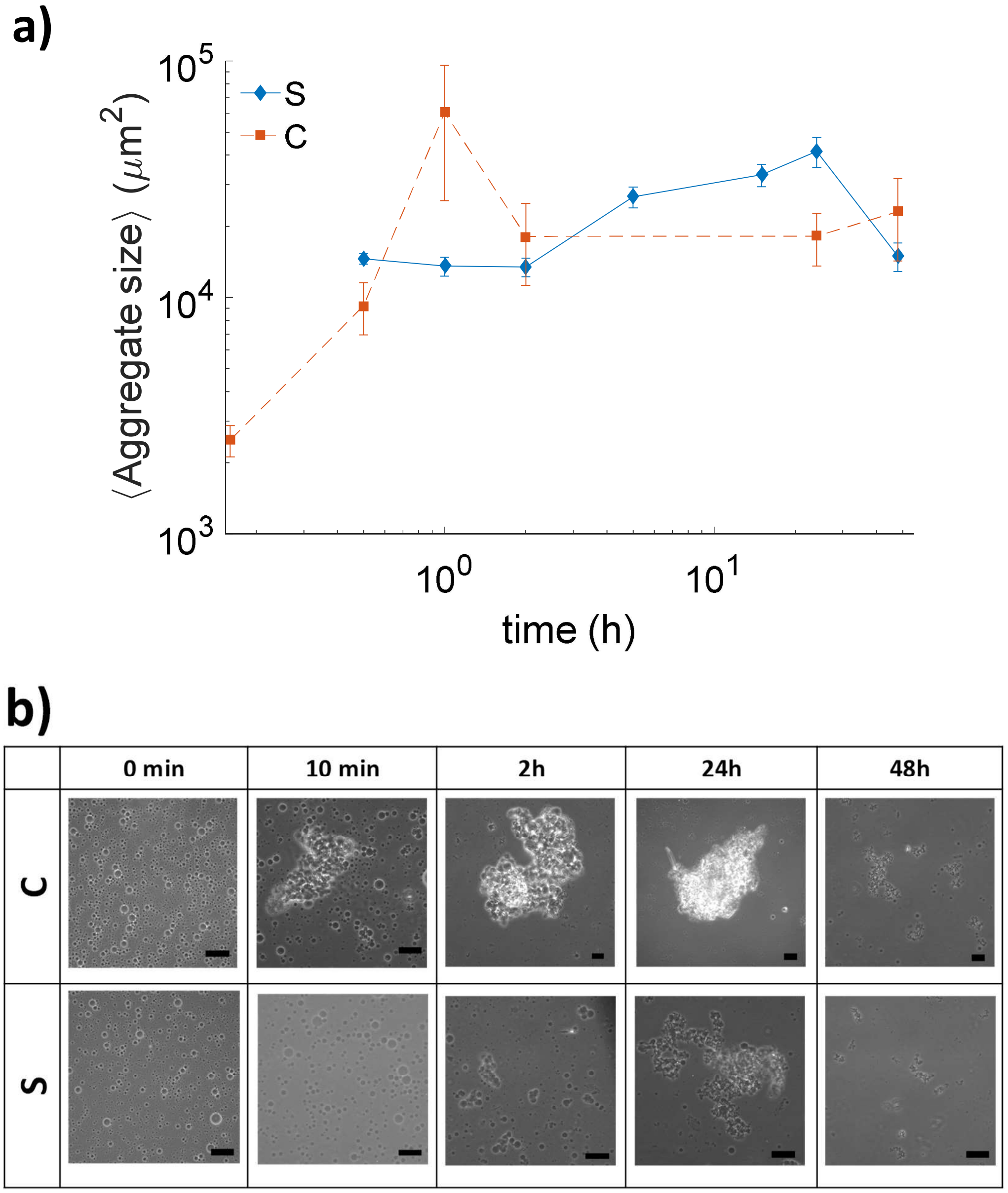

Fig. 33. A. Evolution of the average aggregate size with time. The first line displays the results from concentration experiments (C) and the second line the images from the sedimentation experiments (S). Fig. B. Phase contrast microscopy images showing the evolution of the aggregate size in time. The pictures show an example of the aggregates obtained at every time point.

chances of contact between vesicles and also diminished the volume in which streptavidin could diffuse, which yielded larger aggregates in shorter timescales. Figure 33A shows the change in the averaged aggregate area in time for sedimentation and concentration protocols. Based on the obtained quantitative information and observation of the aggregate evolution with time, we could hypothesize that the aggregates went through three different regimes: growth, steady state, and degradation. During the growth phase, the size of the aggregate increased with time and less free vesicles were found in solution. In the concentration protocol, the size of the aggregates started to increase at approximately 10 minutes after the start of the incubation, and lasted up to 2h. In the sedimentation protocol, the growth phase started at 30 minutes and lasted until 24h after the start of the incubation. In the steady-state phase, the aggregate size presented small variations with time, lasting from 2 to 48 h in the centrifugation method and from 5 to 24 h in the sedimentation method. The degradation phase occurred at approximately 5h after the start of the incubation and it set the end of the aggregate lifetime, which was characterized by shrinkage of the vesicles and appearance of debris, as shown in Fig. 33B. In perspective of the obtained results, it was decided that the optimal incubation timescale for centrifugation and sedimentation samples was 2h, since longer timescales did not provide significantly larger aggregates and added unnecessary time to the experiments. Even though the steady state phase for sedimentation protocol aggregates starts at 5h, we decided to set the incubation time to 2h, because at 5h aggregates started displaying signs of ageing and thus were not optimal for quantification purposes. For the same reason, the optical microscopy measurements were performed not later than 4h after the start of the incubation.

Soft Matter

PAPER

View Article Online
View Journal | View Issue

Cite this: *Soft Matter*, 2021, **17**, 5061

Design of vesicle prototissues as a model for cellular tissues†

Laura Casas-Ferrer, Amaury Brisson, ‡§ Gladys Massiera and Laura Casanellas *

Received 3rd March 2021,
Accepted 22nd April 2021

DOI: 10.1039/d1sm00336d

rsc.li/soft-matter-journal

Synthesizing biomimetic prototissues with predictable physical properties is a promising tool for the study of cellular tissues, as they would enable to test systematically the role of individual physical mechanisms on complex biological processes. The aim of this study is to design a biomimetic cohesive tissue with tunable mechanical properties by the controlled assembly of giant unillamelar vesicles (GUV). GUV–GUV specific adhesion is mediated by the inclusion of the streptavidin–biotin pair, or DNA complementary strands. Using a simple assembly protocol, we are capable of synthesizing vesicle prototissues of spheroidal or sheet-like morphologies, with predictable cell–cell adhesion strengths, typical sizes, and degree of compaction.

1 Introduction

Nature represents an endless source of inspiration for scientists. Biomimetic approaches have been developed with the aim of reproducing particular features displayed by living organisms for targeted functions. Synthetic biology gets inspiration from biological systems, with the goal of redesigning them or even conceiving new artificial biological systems displaying specific capabilities. Such bottom-up approaches led to the fabrication of artificial cells and tissues.[1–4] This approach can be beneficial in order to develop promising biomedical or pharmaceutical applications, but also very valuable for fundamental research. The manipulation of artificial cells can be suited for the study of cell properties or cellular mechanisms, which are challenging to tackle using living cells, due to their inherent complexity or its multifactorial nature.[5–7] In this context, a diversity of simplified biomimetic artificial cells has been developed, displaying a reduced degree of complexity. Whereas these cell models can be diverse in architecture (droplets, coacervates, liposomes, polymersomes[1,8]) giant unilamellar vesicles (GUVs) represent one of the most relevant biomimetic prototypes.[9]

GUVs are constituted of a phospholipid semi-permeable bilayer. The biochemical membrane composition can be enriched at will by using specific lipid mixtures and the inclusion of membrane proteins. However, GUVs are reductionist cell models since they are passive objects that cannot actively move, exchange, nor exhibit mechano-transduction mechanisms, reproduce, or die. Vesicles are soft objects with a membrane bending modulus of about tenths of k_BT, and are prone to display large membrane fluctuations due to thermal agitation. Their low lysis tension makes them susceptible to form membrane pores under moderate osmotic pressure differences between the inner and outer buffer. Over the last decades vesicles have been employed to model the biochemistry and biophysics of cells.[1] A huge effort has been done in the community in making GUVs akin to living cells, for example by reproducing lipid rafts on their membranes,[5] taking into account additional inner compartmentalisation (with the inclusion of smaller daughter vesicles),[10] or by arming the GUV membrane with an inner active shell of actin.[11] The goal of the present paper is not focused on the development of single cell features, but on the controlled assembly of an ensemble of vesicles for the formation of a vesicle prototissue, as a model for cellular tissues. Biological tissues are extremely complex systems. On top of the complexity of individual cells, tissues are formed from the interconnection between adjacent cells mediated by cell–cell adhesion sites enabling collective functions. Living tissues are inherently out-of-equilibrium systems. Cell-division and apoptosis are at play, as well as exchange of information between cells and the surrounding environment (through mechano-sensing systems), giving rise to a dynamic tissue reorganization. In addition, in specific biological processes, such as embryogenesis, tumor metastasis or wound healing, tissues are prone to migrate and reshape extensively over relative short time scales of minutes or hours, resulting into the occurrence of collective tissue flows.[12] Extraordinary progress on the understanding of biological mechanisms regulating living tissues has been achieved over the last decades, partly based on the development of animal models.[13–15] However, *in vivo* models it is extremely challenging to uncouple and elucidate the role of different underlying mechanisms.

Laboratoire Charles Coulomb (L2C), UMR 5221 CNRS-Université de Montpellier. Place Eugène Bataillon, 34095 Montpellier, France. E-mail: laura.casanellas-vilageliu@umontpellier.fr

† Electronic supplementary information (ESI) available. See DOI: 10.1039/d1sm00336d

‡ Present address: Max Planck Institute of Colloids and Interfaces, Am Mühlenberg 1, 14476 Potsdam, Germany.

§ Present address: Potsdam University, Karl-Liebknecht-Str. 24-25, 14476 Potsdam, Germany.

Biomimetic approaches, instead, offer the possibility to design experiments to selectively probe specific mechanisms involved in living tissues, and to get a quantitative insight.

In living cells, cell–cell adhesion is mediated by cell adhesion molecules (CAMs) present in the cell membrane bridging adjacent cells. Cell adhesion results from a combination of attractive interaction due to specific bonding of CAMs, repulsion originating from the outer cell glycocalyx, and membrane elasticity.[16,17] There is evidence of a large number of active mechanisms taking part in cell adhesion (*i.e.* a complex signaling network orchestrating CAMs, interaction of binding sites with cell cytoskeleton, mechano-sensing processes, *etc.*).[18] Nonetheless, an important part of cell adhesion is due to passive physical mechanisms involving lateral diffusion of binding molecules and cell elasticity.[16,19] These mechanisms can be investigated in depth making use of biomimetic cell models. The number of attempts to develop GUV-prototissues is, up to now, limited.[20,21] Amorphous 3D vesicle aggregates have been produced using vesicle constructs adhering thanks to a ligand–receptor pair such as streptavidin–biotin[22–26] or lectin-carbohydrates,[27] and thanks to the specificity between complementary DNA strands,[28–31] and also by means of non-specific adhesion mediated by electrostatic interactions.[32,33] The streptavidin–biotin pair, although it displays a bonding strength of $35k_BT$, well above biological bonds involved in cell–cell adhesion, has been greatly employed in mimicry studies and in biotechnological applications due to its robustness and well-characterized interaction.[34–36] Such large binding affinities makes vesicle–vesicle adhesion energetically favorable, overcoming unfavorable nonspecific interactions (Helfrich membrane fluctuations, electrostatics, or steric repulsion).[16] Further developments on biomimetic prototissues have been implemented with the goal of reproducing specific tissue functions: communication between compartments, by the formation of lipid nanotubes[37] or the inclusion of protein pores[38] on the membranes connecting the interior of adjacent vesicles; external manipulation of GUVs using optical tweezers[38] or magnetic fields[39] has also offered the possibility to fabricate predictable 3D spatial arrangements; and thermoresponsive functions of vesicles (or proteinosome) prototissues have been implemented using DNA-based technologies[40] (or thermoresponsive polymers[41]), leading to reversible compaction of tissues.

The goal of the present work is to design a prototissue by the assembly of GUVs in the presence of ligand and receptors at suitable concentrations. Two ligand–receptor systems have been implemented: the inclusion of the biotin–streptavidin complex and the adhesion based on the complementarity of single-stranded-DNA chains. Using a simple assembly protocol for which we only adjust the mixing method, as well as vesicle and ligand and receptor concentrations, we are capable of synthesizing vesicle prototissues of spheroidal or sheet-like morphologies with predictable cell–cell adhesion strengths, typical sizes, and degree of compaction. The tissue properties can be tuned independently, which opens the possibility to isolate the role of specific physical properties and unravel their individual role in complex physiological problems.

The article is organized in the following way. Section 2 includes details on Materials and Methods. Results and discussion are presented altogether in Section 3. First, the different regimes recovered for vesicle aggregation are qualitatively displayed in a phase diagram (Section 3.1). Next, we quantify the properties of adhesive vesicles (Section 3.2). We then characterize the size of vesicle prototissues (Section 3.3) and their morphology, 3d *vs.* 2d-structures and cohesion (Section 3.4). Finally the conclusions of our work are drawn in Section 4.

2 Materials and methods

2.1 Vesicle fabrication

Giant unilamellar vesicles were produced by electroformation.[42] The lipid mixture used was either Egg-PC (Sigma Aldrich, P3556) alone or Egg-PC and DSPE-PEG(2000)-Biotin (Avanti Lipids, 880129P) at molar fractions 1.25, 2.5, 5 and 10%. Fluorescence of the vesicle membrane was provided by adding either 16 : 1 Liss Rhodamine PE (Avanti Polar Lipids 810158, red marker, with λ_{abs} = 560 nm and λ_{em} = 583 nm) or NBD-PE (Avanti Polar Lipids 810141, green marker, with λ_{abs} = 460 nm and emission at λ_{em} = 535 nm) at 1% mol. The electroformation chamber was prepared by spreading 50 μL of the lipid mixture on two ITO slides (Sigma Aldrich, 636916), left under vacuum for at least 1 h 30 min to evaporate the solvent. The slides were then placed facing each other using a 1 mm thick PDMS spacer. The chamber was filled with a filtered 290 mOsm sucrose (Sigma Aldrich, S7903) solution prepared with ultrapure Milli-Q water. An alternative tension was applied between both slides at a frequency of 10 Hz, and the amplitude was gradually increased from 0.2 to 1.2 V for a total duration of 2 hours, with a final step at 4 Hz and 1 V for 30 minutes in order to enhance vesicle detachment from the slides. The electroformed vesicles were collected and stored in a plastic tube at 4 °C for a maximum of one week. In assembly experiments, vesicles were dispersed in a glucose solution at 300 mOsm. A difference in osmolarity between the outer and inner vesicle solutions was maintained constant to +10 mOsm, which enabled vesicles to slightly deflate.

In view of the assembly experiments, it was important to control the volume fraction of vesicles used in each experiment. Since the yield of vesicle production differed from one electroformation to another, we quantified the volume fraction of vesicles for each electroformation and dilute the solution in order to start assembly experiments at a concentration of reference that we set to $c_0 = (3.3 \pm 0.5) \times 10^3$ vesicles per μL. In order to estimate the concentration of vesicles in the electroformed solution we used a counting procedure: 10 μL of the vesicle solution were placed in an observation chamber filled with a glucose solution (less dense than the inner sucrose solution) so that all vesicles sedimented at the bottom of the chamber (at a same focal plane). We took several images of the vesicles in phase-contrast microscopy and used an ImageJ routine in order to count the number of vesicles per unit area to extrapolate the vesicle volume fraction, and estimate the overall vesicle concentration assuming homogeneous distribution of vesicles within the chamber. A size threshold for the vesicle radius, r_{min} = 1 μm, was set in order to disregard impurities in the counting procedure.

The computed average radius of the electroformed vesicles was $r = 6 \pm 3$ μm (an histogram with the typical size distribution of electroformed vesicles is provided in the ESI†).

2.2 Assembly protocol

2.2.1 Assembly with streptavidin–biotin. Streptavidin (SA) is a tetrameric protein that has four binding sites for biotin. Biotinylated lipids were present on vesicle membranes, enabling bridging between adjacent vesicles. In the following, we will refer to biotinylated lipids as receptors and to SA molecules as ligands. In our experiments we used fluorescent texas Red Streptavidin Conjugate (Fisher Scientific, 10338002), enabling the visualization and quantification of vesicle–vesicle contacts by confocal microscopy. SA was stocked in PBS (292 mOsm) at a concentration of 1 mg mL^{-1} and stored at 4 °C for one month. Necessary amounts of SA were added to the solution of biotinylated vesicles to match the X ratios. Experimentally, X was computed as the total number of SA molecules in solution (N_{SA}) to the total number of biotin molecules contained on the outer leaflet of vesicle membranes (N_{b}), according to the biotin molar ratio used in the lipid mixture for the electroformation, and taking into account the total number of vesicles present in the assembly mixture, so that $X = N_{\mathrm{SA}}/N_{\mathrm{b}}$. Since electroformed vesicles displayed an important polydispersity, we took into account the vesicle size distribution for the estimation of the mean vesicle surface. In our experiments, X values ranged from 0.4 to 40. Larger values of X could not be attained experimentally, as we observed vesicle degradation. After addition of SA, the samples were left incubating for approximately 2 h. For larger incubation times, the typical sizes of the aggregates did not increase significantly. After 24 hours of incubation, however, we observed degradation of vesicles (deflated vesicles, as well as the apparition of vesicle debris in solution).

We used three different modes of incubation: Concentration (C), Sedimentation (S), and in-plane Rotation (R), illustrated in Fig. 1. In the Concentration method, an initial volume of the electroformed-vesicles solution (ranging from 10 to 400 μL) was mixed with a volume of glucose solution (300 mOsm) 1.5 times larger, and centrifuged at 7g during 30 min. Due to the difference in density between the inner- and outer-vesicle solutions vesicles were driven to the bottom of the tube. Next, the upper supernatant solution (free of vesicles) was removed and only 10 μL were left, and then the necessary volume of SA solution was added (ranging from 0.1 to 10 μL). After an incubation period of 2 hours, the aggregate solution was gently pipetted and deposited into an observation chamber, which was then filled with glucose solution to a final volume of 100 μL. In the Sedimentation method a fixed volume of the vesicle solution (20 μL) was added to 80 μL of the glucose solution into a plastic tube. The centrifugation stage was omitted in this protocol and vesicles were driven towards the bottom part of the tube solely by the gravitational force. In the in-plane-Rotation method, 20 μL of the vesicle solution were added to 80 μL of the glucose solution directly in an observation chamber, so that the incubation step was performed in the chamber. During incubation, an in-plane rotation was applied by means of a rotating plate device at 60 rpm, in order to enhance in-plane vesicle–vesicle encounters. This method is used for cell culturing in wells, which are swirled on an orbital shaker in order to generate a flow inside the well.[43] Since the area of the observation chamber we used was about 3 times larger than the area occupied by the total number of vesicles in solution, vesicle assembled forming a 2D-vesicle layer. Concentration and Sedimentation protocols were favored in order to obtain 3D aggregates while the Rotating method led to the formation of 2D monolayers.

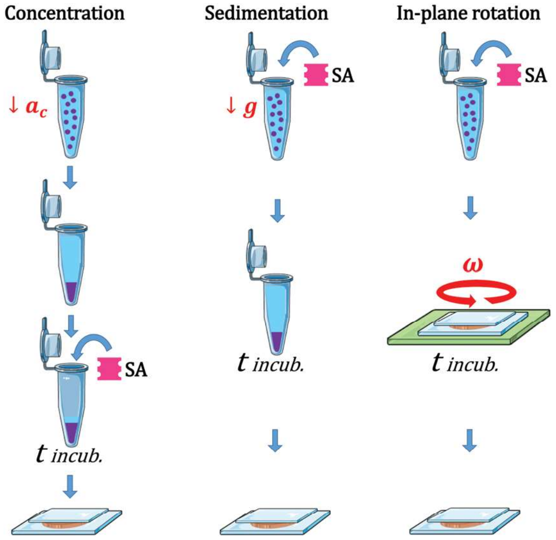

Fig. 1 Scheme representing the different protocols used for the vesicle assembly: Concentration (C), Sedimentation (S), and Rotation (R). In (C) vesicle–vesicle encounters were driven by a centrifugation step (at centripetal acceleration a_c = 7 g), while in (S) they were solely driven by the gravitational force. In (R), an in-plate rotation of 60 rpm was applied. In all protocols the incubation time (t_{incub}) was set to 2 h.

2.2.2 Assembly with DNA complementary strands. Vesicle assembly was also achieved using complementary DNA strands. The DNA linkers consisted of a cholesterol which anchored to the vesicle membrane, followed by a spacer made of a DNA double strand with a length of 43 base pairs, and were ended with a 9 bases sequence of single stranded DNA, that acted as sticky end.[40] The interaction of a sticky end with its complementary strand was the mechanism driving the assembly of the vesicles. This interaction is mediated by hydrogen bonding between complementary base pairs (A: T, C: G). We used the same DNA sequences designed by Parolini *et al.*[40] (IDT Company) with a binding energy of 18.3$k_{\mathrm{B}}T$. Equal amounts of DNA complementary constructs were added to the vesicle solution, at a total concentration of 32 or 644 nM. Fluorescence of the DNA was provided by adding 2 μM of the intercalating dye SYTO 64 (λ_{abs} = 599 nm, λ_{em} = 619 nm, Thermo Fisher). Further details on the fabrication of DNA constructs and DNA mediated assembly are provided in the ESI.†

2.3 Visualization of vesicle aggregates

For vesicle prototissue imaging, we prepared observation chambers with an Ace O-ring (Sigma Aldrich, Z504696) fixed to a glass coverslip using UV-glue (Norland), that we previously cleaned and functionalized with β-casein bovine (Sigma Aldrich, C6905).[11]

To prevent evaporation, samples were covered with a glass coverslip and sealed with grease before proceeding to image acquisition. Phase contrast and epifluorescence images were obtained with an inverted microscope (DMIRB, Leica) with objectives ×10 (NA = 0.25) or ×20 (NA = 0.4) and a Hamamatsu camera (C13440 ORCA-flash 4.0). The source of light for fluorescence imaging was a CoolLED pE-300 white LED lamp. Confocal images were obtained with a confocal microscope (Zeiss LSM880) and with a ×40 objective (water immersion, NA = 1.1). Signal acquisition was performed with two detectors (GaAsP and PMT) used respectively for an Argon laser (λ = 488 nm), and for an He/Ne laser (λ = 633 nm).

2.4 Quantification of aggregate properties

2.4.1 Membrane fluorescence. In order to assess quantitatively the concentration of fluorescent molecules on vesicle membranes, the equatorial plane of single vesicles or vesicles forming vesicle doublets was imaged using confocal microscopy. With the ImageJ Radial profile tool, a circle (or an arch) were placed to fit a whole vesicle (or a part of its membrane) to obtain the integrated fluorescence intensity, normalized by the perimeter (or arch length), as shown schematically in the inset of Fig. 3B. Analogously, in order to perform the fluorescence quantification of the adhesion patch we fitted a rectangle at the interface between the two vesicle membranes to obtain the integrated fluorescence intensity, normalized by the length of the patch. Both routines were applied to the red and green channels corresponding to the red SA and green lipid marker incorporated into the membranes.

2.4.2 Contact angle of vesicle doublets. Vesicle–vesicle adhesion was quantified by measuring the equilibrium contact angle (θ) between two vesicles of comparable vesicle sizes,[35,44–47] that we call a vesicle doublet. Vesicle doublets were prepared by adding necessary amounts of SA to a solution of biotinylated vesicles at a vesicle volume fraction of 0.25%, and incubating them for 2 h in a tube rotator at room temperature. This high dilution protocol favored the assembly of vesicles into doublets and minimized the formation of vesicle aggregates. The samples were imaged in confocal microscopy. A z-scan of each doublet was performed in order to identify the largest length of the adhesion patch (corresponding to their equatorial plane) which was used for the quantitative analysis. We analyzed doublets formed by two vesicles of comparable sizes (with a size difference below 20%) and a flat vesicle–vesicle interface. The contact angle was obtained by fitting a circle to each vesicle, and computed after the radii of the two vesicles (R_1, R_2), and the coordinates of their centers (see ESI† for further details). A sketch is shown in the inset of Fig. 3A. The number of doublets analyzed for all conditions was set to N = 20.

2.4.3 3d-aggregate sizes. The vesicle prototissues obtained using the Concentration and Sedimentation protocols had a 3-dimensional structure. 3d-imaging and quantification of object sizes was performed by confocal microscopy. Aggregate volumes were measured using Imaris Software (Oxford Instruments) which enables 3d-reconstitution of aggregates from 2d z-stacks obtained with confocal microscopy, with a final resolution along the *z*-axis of 1 μm. The software enabled the determination of the overall external surface and the enclosed volume of the aggregate, but did not identify possible inner voids contained within the structure.

3 Results and discussion

3.1 Aggregation phase diagram

Vesicle aggregation was shown to depend on the concentration of ligands (SA molecules) in solution and receptors (biotin-lipids) on vesicle membranes. In the phase diagram of Fig. 2 the different aggregation states can be distinguished. For very low SA concentrations (low X), and regardless of the lipid-biotin content, vesicle aggregation did not take place. In this situation the number of receptor–ligand–receptor bridges per vesicle was too low to enable the adhesion between adjacent vesicles (control experiments performed with no SA in solution led to no vesicle aggregation).

For a given biotin-lipid content, as the SA concentration was increased, vesicle–vesicle doublets were first obtained, and assemblies of multiple vesicles in aggregates formed at larger SA concentrations. In Fig. 2, we distinguish between small (size $< 4 \times 10^3$ μm^2), medium (4×10^3 μm^2 < size $< 2 \times 10^4$ μm^2) and large (size $> 2 \times 10^4$ μm^2) aggregates, which are depicted with different color intensities (as obtained from 2D images, sizes correspond to the maximal projection on the plane; more accurate 3d-quantitative data are provided in Section 3.3). By increasing the concentration of SA, most biotin-lipids got saturated by SA, preventing further vesicle–vesicle adhesion, and limiting the size of vesicle aggregates and eventually completely inhibiting vesicle aggregation. This trend is partly visible in Fig. 2, for 5% and 10% mol biotin, for which aggregate sizes decrease for the largest X values. Thus, the vesicle aggregation process was initiated but also inhibited by free SA in solution, in agreement with previous experimental works.[23,29,48]

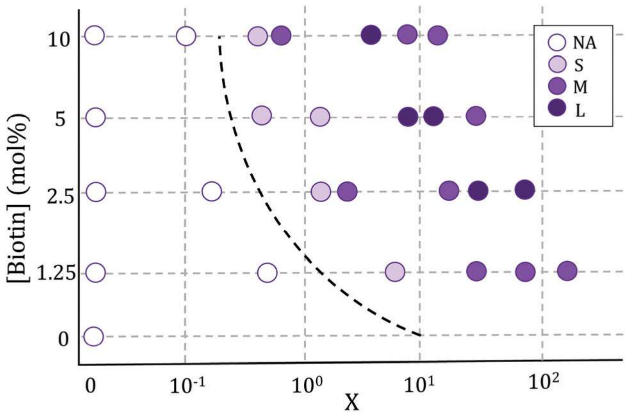

Fig. 2 Phase diagram of vesicle aggregation as a function of biotin concentration and $X = N_{SA}/N_b$, obtained using the Sedimentation (S) protocol. Maximal aggregate sizes for each condition are indicated as: S (small aggregates) $<4 \times 10^3$ μm^2; 4×10^3 μm^2 < M (medium-size aggregates) $<2 \times 10^4$ μm^2; L (large aggregates) $>2 \times 10^4$ μm^2. NA stands for 'no aggregation'.

For a constant X ratio, aggregate sizes increased with increasing biotin-lipid content, as this entailed an increasing number of available receptors and a larger potential number of bridges that could be formed between vesicles. The assembly protocol used for vesicle aggregation also played a relevant role in the aggregation phase diagram. The Concentration protocol systematically led to vesicle aggregates with typical larger sizes compared to the Sedimentation protocol, regardless of the X ratio and biotin content (not shown in the figure). We can rationalize the dynamics of vesicle assembly in terms of the time scale for vesicle–vesicle encounter ($t_{\text{ves–ves}}$). In the Sedimentation (S) protocol (used for results shown in Fig. 2) vesicle–vesicle collisions were only driven by sedimentation. Typical times for vesicle–vesicle encounters can be approximated by the sedimentation time of vesicles inside the incubation tube. Considering the Stokes regime and an incubation volume of 100 μL, this leads to $t_{\text{ves–ves}} \simeq 15$ min. Note however, that this is an overestimation as we disregard the possibility for vesicle–vesicle encounters to take place before reaching the bottom of the incubation tube. The adsorption of free SA in solution onto vesicle membranes takes place during this lapse of time before two vesicles encounter. Aggregation kinetics thus results from a combination of both vesicle–vesicle encounters and diffusion of free SA to vesicle membranes, which makes it difficult to control. Note that this competition will also be dependent on the X ratio. For large X values ($X \gg 1$) vesicle surfaces may become saturated by SA before encountering another vesicle, thus hindering further vesicle bridging. In order to gain control on the assembly process, we privileged the Concentration (C) protocol for which vesicles were brought to close contact by a centrifugation stage prior to the addition of SA, greatly reducing the vesicle encounter time. Kinetics play a minor role in this protocol, which makes it more suitable for the synthesis of aggregates of controlled sizes (we will use this protocol in Section 3.3 when controlling aggregate sizes).

In all incubation methods, the incubation volume for vesicle assembly was considerably larger than the volume fraction of vesicles. Thus, it is likely that not all SA molecules could reach the biotin groups on vesicles surfaces within the incubation time of 2 h, and that a fraction of SA could remain free in solution. As a consequence, the ratio X (computed as the number of SA molecules in solution over the biotin-lipids on vesicle membranes, $X = N_{\text{SA}}/N_{\text{b}}$) does not necessarily coincide with the average ligand-to-receptor ratio on vesicle membranes. In the following, however, we will refer to X as the ligand-to-receptor ratio. Vesicle–vesicle bridging should be maximized for $X = 0.25$, corresponding to a an equal number of receptors and ligand sites (4 sites per SA molecule).[48] In practice, and due to the presence of free SA molecules in solution, we obtained the largest aggregate sizes (Fig. 2), as well as maximal contact angles for vesicle doublets (in Fig. 3A), for $X > 0.25$. Analogously, $X \simeq 1$ corresponds to a situation in which there is one biotin per SA molecule, so that increasing X further would hinder vesicle–vesicle adhesion due to saturation of SA molecules. Experimentally, we recover such trends (decrease of aggregate sizes in Fig. 2, and the downturn in contact angle for vesicle doublets, Fig. 3) for $X \gg 1$.

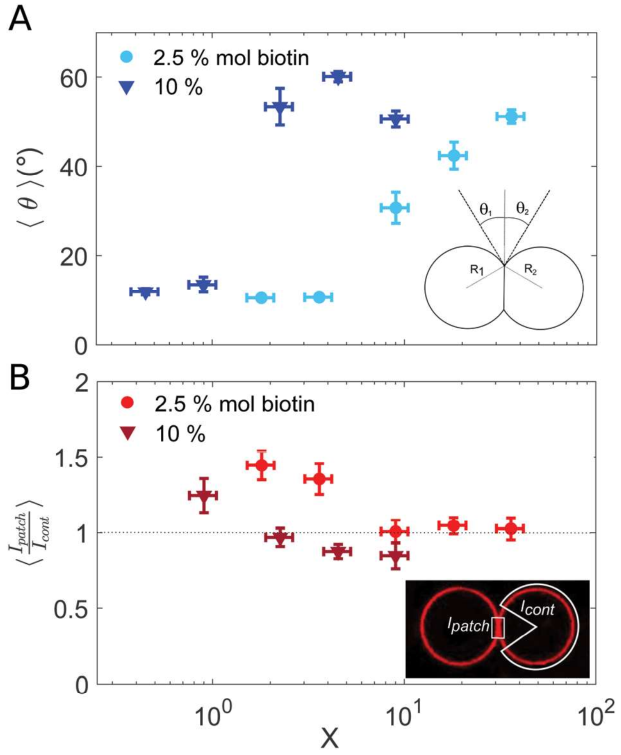

Fig. 3 Characterization of vesicle doublets, as a function of the ligand-to-receptor ratio, X. (A) Contact angle (θ) of vesicle doublets, as a function of X. The contact angle was computed by averaging the two contact angles of the doublet (θ_1 and θ_2). The number of doublets analyzed for all conditions was set to $N = 20 \pm 4$. The displayed values correspond to the mean, with the standard error as the error bars (error bars smaller than the symbol size are not displayed). In order to highlight the dispersion of the data a representation in a box-plot form is provided in the ESI.† (B) Fluorescence intensity at the vesicle–vesicle patch normalized by the intensity at the vesicle contour. The fluorescence was provided by SA molecules present on vesicle membranes. Doublets were imaged at their equatorial plane using confocal microscopy. Two different biotin contents were used: 2.5 and 10% mol. Vesicle volume fraction was set to 0.25% v/v (which corresponded to a total vesicle volume of 2.5×10^8 μm^3). The number of doublets analyzed for all conditions was set to $N = 10 \pm 4$. The displayed values correspond to the mean, with the standard error as the error bars. A horizontal line at $\langle I_{\text{patch}}/I_{\text{cont}} \rangle = 1$ is included as a guide to the eye.

3.2 Adhesive vesicle properties

3.2.1 Ligand–receptor density on vesicle membranes.

In order to ensure that the targeted molar fraction of biotin-lipids was effectively incorporated into GUV membranes, fluorescence quantification of vesicle contours was performed in confocal microscopy. For this, we prepared vesicles with a fluorescent analog of the biotin-PEG(2000)-DSPE molecule, in which the biotin head was replaced with a carboxyfluorescein (CF) group[30] thus enabling quantification with fluorescence imaging, using the same molar lipid percentages of 1.25, 2.5, 5 and 10% mol. Since CF is emitting at 515 nm (green), for this set of experiments we marked the vesicle membranes with Rhodamine-lipid, emitting at 583 nm (red), at a fixed Rhod-lip/EggPC molar ratio of 1%, and that we used as a reference intensity value. We measured the fluorescence intensity of both the CF-green molecule and the red

Rhodamine-lipid. The intensity ratio of both signals increased linearly with the CF molar percentage within experimental error (data is available at the ESI†). This suggests that the CF-lipid/Egg-PC ratio in the membrane corresponds to the lipid preparation used for the electroformation, and we expect the same behavior for biotinylated lipids.

Another important quantification concerns the number of (fluorescent) SA molecules bound to the outer membrane leaflet of the vesicles. For this, we quantified the fluorescence intensity of vesicle contours at SA saturating conditions, corresponding to the maximum fluorescence intensity obtained on the membrane when increasing the SA concentration in solution. The saturation intensity obtained for vesicles containing 10% mol biotin-lipid was only about two times larger than the values obtained for vesicles at 2.5% mol. In the following, we establish relation between this fluorescence intensity to the surface density of SA molecules bound to biotin-lipids on the vesicle membranes. We can estimate the surface density of biotin-lipids (Γ_b) taking into account the molar ratio of biotin-lipids used in the lipid mixture, and the surface of a phospholipid (65 Å^2). This leads to $\Gamma_b = 3.85 \times 10^4\ \mu\text{m}^{-2}$ and $15.4 \times 10^4\ \mu\text{m}^{-2}$ for vesicles containing 2.5% and 10% mol biotin respectively, or in other words, to a typical biotin-biotin distance on vesicle membranes of D_b = 5.1 nm and D_b = 2.5 nm respectively. The distance between biotin-lipids is, in both cases, comparable to the lateral size of SA molecules (of 4.8 nm and 5.5 nm, after the crystallographic data provided by Hendrickson *et al.*[49]). For 2.5% mol biotin, one or two biotin-lipids can bind to a SA molecule. For 10% mol biotin, the distance between biotins is smaller than the lateral size of SA. Thus, SA molecules are dimerized, with two biotins bound per SA, and a fraction of biotin-lipids remains unbound. This would explain why the saturation intensity obtained for vesicles with 10% mol biotin-lipid was only about two times larger than the values obtained for vesicles at 2.5% mol. We have excluded in our interpretation the possibility for loop formation, in which more than two biotin-lipids from a same vesicle would bind to a SA molecule. The lateral size of PEG-2000 polymers for 2.5% and 10% mol biotin vesicles is L_{PEG} = 3.5 nm and 6.5 nm, respectively (which correspond to polymers in the mushroom and in the brush regimes).[50] Since the smallest lateral size of the SA molecule is L_{SA} = 4.8 nm, loop formation is geometrically hindered.

3.2.2 Adhesion of vesicle doublets. Experimentally, we measured the degree of vesicle–vesicle adhesion by determining the equilibrium contact angle (θ) between vesicles forming a doublet. In Fig. 3A we show the results obtained for the contact angle as a function of the ligand-to-receptor ratio, and for two different vesicles compositions (2.5% and 10% mol biotin-lipid). The values of contact angle, obtained at a given X value, display a significant dispersion. This may partly be attributed to the variability of electroformed GUVs, in terms of excess area, which can notably influence the contact angle of GUV doublets. In order to show the distribution of the contact angle values we provide in the ESI† a box-plot representation of the data. For 2.5% mol biotin, the smallest values of contact angles are $\theta \simeq 10^\circ$, corresponding to $X \leq 4$. For very small contact angles ($\theta \leq 15^\circ$), however, it was difficult to unambiguously distinguish experimentally vesicle-doublets from neighboring vesicles in close contact (but with no adhesion patch). A continuous increase in contact angle is observed for $X \geq 9$. Doublets were clearly identified in this regime, as the vesicle membranes formed spherical caps. The largest values of the contact angles, $\theta \simeq 51^\circ$, correspond to the largest ligand-to-receptor ratios ($X \simeq 36$). For vesicles containing 10% mol biotin, the increase of the contact angle with X is steeper, and the curve is shifted towards smaller X values. The extent of the vesicle adhesion patch (and the contact angle) depends on the total number of bridges accumulated in it. At a given X ratio, vesicles with 10% mol biotin have four times more biotin available for bridges formation, and thus can display larger contact angles in vesicle-doublets than those containing 2.5% mol. For vesicles with 10% mol biotin, the maximum value obtained for the contact angle is slightly larger ($\theta \simeq 60^\circ$) than for 2.5%, which can also be attributed to a larger number of bridges formed in the adhesion patch. By increasing the SA concentration further ($X > 5$) the contact angle diminishes (this behavior is only observed for 10% mol biotin, since no larger X values could be reached experimentally for vesicles with 2.5%). We can interpret this downturn, as a situation being close to saturation of SA, for which almost all biotin sites would be bound to SA thus preventing further vesicle–vesicle adhesion and leading to a decrease in the extent of the adhesion patch.

Results for the fluorescence intensity of vesicle doublets are shown in Fig. 3B. The fluorescence signal corresponds to the SA fluorescent molecules attached to the vesicle membrane, so that we can relate the fluorescence intensity to the surface density of SA. The intensity of the adhesion patch (I_{patch}) is normalized by the fluorescence of the vesicle contour (I_{cont}). As shown in Fig. 3B, only for the lowest X values ($X < 4$ for 2.5% mol biotin and $X < 1$ for 10% mol), the intensity ratio is larger than one (X = 1.4 and 1.2, respectively). This implies that the intensity at the adhesion patch is larger than at the vesicle contour. These values correspond to slightly bound vesicles, with very small contact angles (Fig. 3A). In such conditions, only a few ligands are attached to membrane receptors, which can diffuse through the lipid membrane and get recruited at the adhesion patch, depleting the vesicle contour from ligands (fluorescent SA). This process is driven by the large binding affinity of the SA–biotin pair. The enrichment of the adhesion patch is in agreement with previous experimental results obtained using micropipette aspiration for small biotin molar percentages (up to 5% mol).[35] For larger X, the membrane coverage with fluorescent ligands was homogeneous all over the vesicles, with comparable values at the adhesion patch and at the vesicle contour. In this regime, the concentration of SA molecules may become sufficient to saturate all biotin sites (both on vesicle contours and in the adhesion patch), thus leading to intensity ratios close to one. Furthermore, Fenz *et al.*[51] showed that biotin-lipids mobility was reduced when SA molecules are attached to them. In the limit of a high number of SA bound to biotin-lipids, an external high-viscosity layer of SA molecules might be formed increasing the hydrodynamic resistance to lipid mobility, limiting their recruitment at the contact zone in this regime. Unfortunately, our experimental setup does not allows us to assess the possible role of these kinetic effects. For 10% mol biotin vesicles and when $X \geq 4$, the surface density of ligands in the vesicle contour may even exceed the density within the adhesion patch ($I_{\text{patch}}/I_{\text{cont}} < 1$). This X value corresponds to the downturn in contact angle (Fig. 3A), for which there exists a saturation of ligands in solution. We think this enhanced brightness observed for vesicle contours may be attributed to free ligands in solution attaching to vesicle contours at long time scales, after doublet formation. When the surface density of SA at the patch reaches its maximal (due to geometrical packing), any further diffusion of SA through the lipid membrane towards the patch is prevented. Note however that this argument is based on a time-dependent behavior which cannot be tested with our experimental setup. Alternatively, we could interpret this result based on additional entropic penalties experienced by linkers in the adhesion patch due to reduction of available configurational space, which has been described for DNA mediated adhesion.[31] Compression of linkers within the adhesion patch upon vesicle–vesicle binding would lead to a decrease in their surface density in the patch, compared to the vesicle contour, which would result into a patch-to-contour intensity ratio lower than 1.

In the following, we address vesicle adhesion in the framework of thermodynamic equilibrium. This description, however, does not take into account dynamical process, which may play a non-negligible role in vesicle assembly. We can write the total free energy variation upon the formation of a vesicle doublet (ΔF) as the sum of an adhesion term (ΔF_{adh}) and an elastic term (ΔF_{el}) associated to membrane deformations,[40,52,53]

$$\Delta F = \Delta F_{\text{adh}} + \Delta F_{\text{el}} \tag{1}$$

The adhesion term comprises a negative enthalpic contribution accounting for the formation of new ligand–receptor bonds in the adhesion patch and it is balanced by an entropic cost, related to the loss of degrees of freedom (translational and configurational) of surface-tethered receptors upon binding.[40,52,54] There exist, nonetheless, a negative entropic term associated to binding state multiplicity in multivalent systems, which favors binding[40,53,54] and which can strengthen the interaction. This combinatorial term is calculated by estimating all possible combinations of bounds formed between ligands and receptors. In our assembly experiments, binding multiplicity is provided by highly adhesive vesicles (which contain a large number of membrane receptors) and by the tetramic nature of SA molecules. The combinatorial term in multivalent biding increases faster than a simple linear addition of the binding energies of monovalent binders, due to a larger number of possible combinations between ligand and receptors.[54] Therefore, in our experiments this term may become significant for vesicles with a large content of biotinylated lipids. In particular, it may partly account for the steep increase in contact angle observed for 10% mol-biotin vesicles (Fig. 3A), compared to the smooth increase obtained for 2.5% mol-biotin ones. Membrane elastic deformations (ΔF_{el}) comprise both bending and stretching modes, and repulsion due to thermal membrane fluctuations. The latter can be neglected in the limit of strong adhesion.[55]

In order to find the equilibrium doublet shape (and the equilibrium contact angle, θ_{equil}) the total free energy should be minimized with respect to the size of the adhesion patch. Solving the minimization problem is a challenging task, which is generally addressed numerically, or for limiting behaviors.[52,56] Ramachandran *et al.*[55] described vesicle–vesicle (LUV–LUV) adhesion theoretically in the strong adhesion limit, by introducing an interaction potential between two planar bilayers (W_{P}), which accounted for the binding energy density in the adhesion patch, and which was balanced by the elastic stretching of vesicle membranes (the bending energy term was neglected in this strong adhesion limit, and entropic contributions were not explicitly included in the model). Even though we use GUVs (instead of LUVs) we will discuss our results obtained for the contact angle (Fig. 3A) in the framework of this work.[55] The authors distinguished two main regimes for vesicle–vesicle adhesion: vesicles with constant volume and osmotically equilibrated deflated vesicles. Equilibrium contact angle was found to be independent of vesicle radii and to increase monotonically with the energy density, in the constant volume approach. In the osmotically equilibrated approach instead, the increase of contact angle with energy density was faster and was dependent on vesicle radius. We recovered small contact angles ($\theta < 15^{\circ}$) for low concentration of ligands (low X). We may interpret these low contact angles as corresponding to the constant volume approach, since vesicles are only slightly deformed, so that they can maintain their initial volume. By increasing the energy density (whether by increasing the biotin content on vesicle membranes or the number of ligands in solution, and thus X), we observed an increase of the equilibrium contact angle. This larger dependence could be attributed to the osmotically equilibrated regime. For such larger deformations, the increase in vesicle area leads to an increase of the vesicle pressure due to membrane tension, which is released by generating a flow of water through the semi-permeable membrane.

3.3 Controlling aggregate sizes

Setting a suitable ligand-to-receptor ratio is crucial for favoring the formation of prototissues of large sizes. As discussed in Section 3.2.2 for vesicle doublets, intermediate ligand-to-receptor ratios led to efficient vesicle–vesicle binding and should be thus also favored when designing vesicle prototissues with maximal sizes. This is shown in Fig. 4, where the mean size of vesicle aggregates ($\langle V_{\text{aggr}} \rangle$) is shown (in log–log scale) as a function of X, for a constant number of vesicles in solution. The results of aggregate volumes provided in the figure are obtained from confocal microscopy images, after 3D-reconstruction. For these experiments, we used the Concentration method which favors vesicle–vesicle encounters and thus the formation of larger aggregates (compared to the Sedimentation protocol). As shown in Fig. 4, the mean aggregates size increases with X, until reaching a maximum aggregate value (for $X \simeq 1$). Increasing X further may result into a decrease of aggregate sizes caused by saturation of receptors by an excess of ligands in solution (as shown in the figure for vesicles containing 1.25% mol biotin-lipids). Biotin-lipid content on vesicle membranes also favored

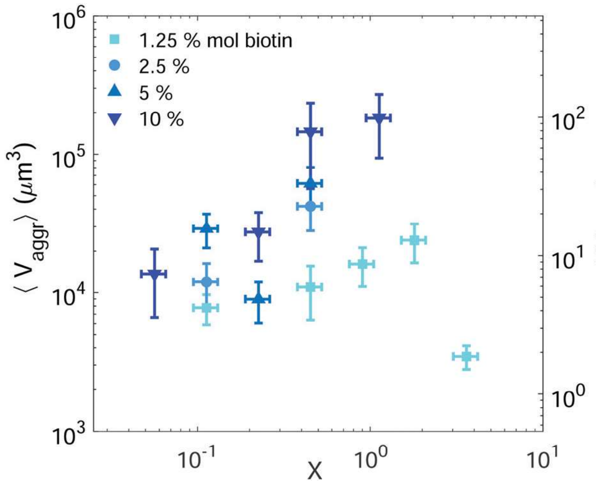

Fig. 4 Mean vesicle volume as a function of the ligand-to-receptor ratio, X. Different colors and symbols correspond to different biotin molar percentages on vesicle membranes (darker colors correspond to larger contents). Vesicle volume fraction was set to 5% (corresponding to a total vesicle volume of 5×10^8 μm^3). For all tested conditions the number of analyzed aggregates was set to $N = 10 \pm 4$. The displayed values correspond to the mean and the error bars to the standard error.

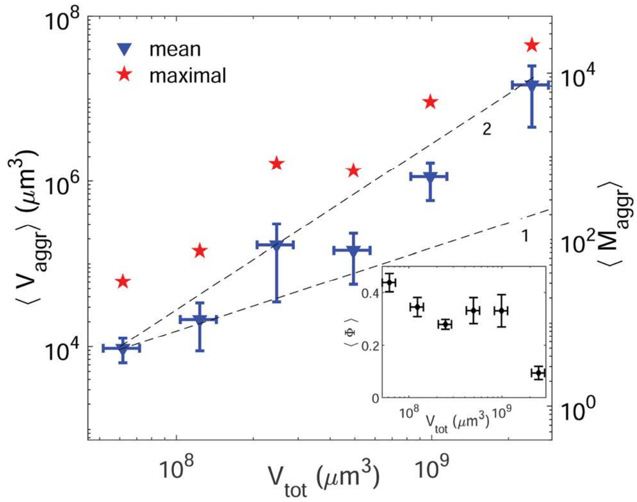

Fig. 5 Mean (blue triangles) and maximal (red stars) aggregate sizes as a function of the total vesicle volume in solution (V_{tot}). Vesicle contained 10% mol biotin-lipids, and the ligand-to-receptor ratio was set to $X = 0.45$. For all tested conditions the number of analyzed aggregates was set to $N = 15 \pm 4$. The displayed values correspond to the mean and the error bars to the standard error. Two lines with slopes 1 and 2 are included as guides to the eye. Inset: Mean sphericity (Φ) of the aggregates as a function of the total vesicle volume (V_{tot}).

vesicle–vesicle adhesion, as it allowed a larger number of bridges to be formed between adjacent vesicles, and thus led to larger aggregate sizes, as observed in Fig. 4 for vesicles containing 1.25% up to 10% mol biotin. By using vesicles containing 10% mol biotin-lipid, we could reach aggregate sizes ranging on one order of magnitude (from 1.4×10^4 μm^3 up to 1.8×10^5 μm^3). We can estimate, as a first approximation (and disregarding interstitial fluid in between adjacent vesicles), the mean number of vesicles contained within the aggregates ($\langle M_{aggr} \rangle$) by dividing the mean aggregate volume ($\langle V_{aggr} \rangle$) by the mean vesicle volume (V_{ves}). We computed V_{ves} by taking into account the vesicle size distribution. This led to a mean aggregate number of $7 \leq \langle M_{aggr} \rangle \leq 98$ vesicles (shown in the right axis of Fig. 4).

The most effective way to control aggregate sizes was achieved by tuning the number of vesicles present in the assembly mixture. We show in Fig. 5 (in log–log scale) the mean (as well as the maximal) aggregate sizes as a function of the volume occupied by the total number of vesicles (V_{tot}), computed as the estimated total number of vesicles in solution times the mean vesicle volume (V_{ves}). In these experiments the assembly volume was kept constant, and the vesicle volume fraction was increased by increasing the total number of vesicles in solution. In order to maximize vesicle aggregate sizes we used vesicles containing 10% mol biotin-lipid, a ligand-to-receptor ratio favoring optimal binding ($X = 0.45$), and assembled them with the Concentration assembly protocol. For all conditions tested, we always obtained an ensemble of aggregates with diverse sizes. Aggregates of small sizes, and even single vesicles were always present. As the number of vesicles was increased, the maximal aggregate size was also increased, and so was the mean average size. By changing the total number of vesicles, mean aggregate sizes extended over more than three decades, 10^4 μm^3 $\leq \langle V_{aggr} \rangle \leq 1.5 \times 10^7$ μm^3, which corresponded to a mean aggregate number $5 \leq \langle M_{aggr} \rangle \leq 8.1 \times 10^3$. As the number of vesicles increased, aggregate sizes became larger because the number of building units was larger, but also because the vesicle–vesicle collision rate was increased. In the hypothetical case where all vesicles would be assembled into a unique aggregate, we would observe $V_{aggr} \simeq V_{tot}$. It is clear, that $\langle V_{aggr} \rangle \ll V_{tot}$. The mean aggregate volume increases more rapidly than linearly with the total vesicle volume (which corresponds to a power-law scaling with an exponent equal to 1), specially for large mean aggregate volumes ($\langle V_{aggr} \rangle > 1.5 \times 10^5$ μm^3). Overall, the increase is compatible with a power-law scaling with exponent 2. In Fig. 5 we have included two lines with slopes 1 and 2, as guides to the eye. To the best of our knowledge, there is no theoretical framework available in the literature capable of rationalizing the observed trends. Vesicles assemble forming several aggregates of diverse sizes (as it is represented in Fig. 4 and 5). The size of vesicle aggregates may result from an intricate combination of different mechanisms, including kinetic effects taking place in vesicle assembly, or shearing forces which may eventually be exerted to the aggregates when removing them from the incubation tube by gentle pipetting, among others. Overall, this makes it difficult to predict theoretically the tendency of the mean aggregate size in terms of the total vesicle volume. We measured the sphericity (Φ), $\Phi = \pi^{1/3}(6V_{aggr})^{2/3}/S_{aggr}$, of vesicle aggregates (where S_{aggr} and V_{aggr} are the aggregate outer surface and the enclosed volume, respectively). $\Phi = 1$ corresponds to a perfect sphere. As shown in the inset of Fig. 5, aggregates became more irregular in shape by increasing the total number of vesicles in solution. The increase of internal void regions, led to irregular 3d-aggregate morphologies, and could also partly account for the large increase observed for the mean aggregate size. Vesicle polydispersity is likely to have a role on the formation of irregular structures.[57,58] Besides, very large aggregates display planar shapes, which may be induced by their own weight, and which lead to small values of Φ.

In cell–cell adhesion, the biological activity, and in particular, active acto-myosin cortex is known to play a fundamental role which cannot be reproduced in our simplified biomimetic prototissue. Cortex contractility has an antagonistic effect to cell adhesion as it favors cell surface minimization (both mechanisms being interdependent), leading to different degrees of tissue compaction.[59,60] Attempts to perform cell aggregates have been addressed with the aim of modeling tumor progression,[61] or for tissue engineering purposes in order to develop artificial organs or tissue transplants. Cell aggregates are constituted by the self-assembly of dispersed cells in suspension. Multicellular spheroids can grow up to typical volumes of 10^9 μm^3.[61] As shown in Fig. 5, we can tune the GUV-aggregate sizes to attain the typical sizes of cellular spheroids, making them potential convenient biomimetic models. However, GUV aggregates display more irregular shapes. In multicellular aggregates round shapes are ensured by cell activity, allowing to explore more configurations and to reach more spherical shapes, minimizing their energy. Additionally, many biological tissues are constituted of cohesive cell monolayers. This is the case of epithelial tissues,[59] or germ layers.[62] There is, therefore, an interest in developing 2d-biomimetic analogs, which enables to reproduce essential ingredients of these complex biological systems (which is addressed in the following section).

3.4 Prototissue morphology

3.4.1 3d-aggregates *vs.* 2d-monolayers. Aggregate morphology was qualitatively tuned by changing the incubation protocol. While Sedimentation and Concentration protocols led to rather globular shapes, in-plane Rotation during incubation induced the formation of vesicle monolayers. The formation of such artificial monolayers represents a simplified model system for epithelial cell monolayers (Fig. 6A). In panel B we show an example of a 2D-vesicle layer, analyzed with the Imaris Software. The reconstruction using this software shows that the prototissue is constituted of one single layer of vesicles. For comparison, we display in panel C a globular aggregate obtained at equivalent volume fraction.

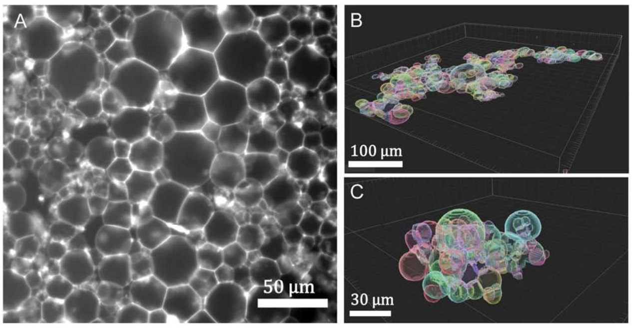

Fig. 6 Prototissue morphologies: (A) 2d-epifluorescence image of a GUV monolayer, ressembling a tissue monolayer (2.5% mol biotin, X = 72.16, (R) assembly protocol). (B) 3d-reconstructed volume obtained from confocal images corresponding to a 2d-GUV-monolayer (10% mol biotin, X = 4.5, (R) assembly protocol). (C) 3d-reconstructed volume obtained from confocal images corresponding to a GUV globular aggregate (10% mol biotin, X = 0.45 (S) protocol). The vesicle volume fraction was set to 0.25% v/v in all assays.

3.4.2 Prototissue cohesion. Changing the number of receptors (biotin-lipids) on vesicle membranes also had an impact on aggregate cohesion. For a given X ratio, increasing the biotin content led to larger aggregates (as previously described for Fig. 4), which were in turn more compact. This trend can be observed in Fig. 7(A–D), in which two aggregates obtained with

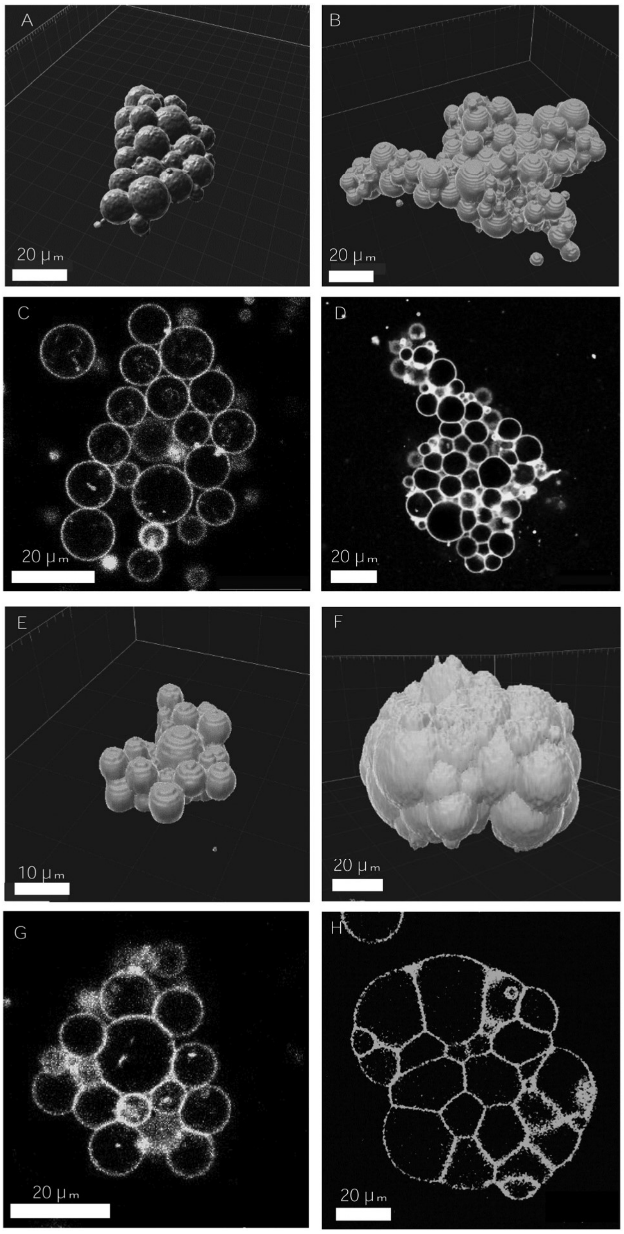

Fig. 7 Examples of 3d-aggregates obtained with the SA–biotin pair (A–D) and DNA complementary strands (E–H) displaying different degrees of cohesion. 3d-reconstructed volume obtained from confocal images, using Imaris software (A, B and E, F), and 2d-confocal images (C, D and G, H). The concentration of receptors and ligands used in the assembly assays were the following: 2.5% mol biotin, X = 0.45 (A and C), 10% mol biotin, X = 1.12 (B and D), [DNA] = 32 nM (E and G), [DNA] = 644 nM (F and H). The volume fraction was set to 0.25% in A–D and to 0.125% in E–G.

vesicles containing different biotin content are displayed. The change in aggregate cohesion is evidenced by the presence (or not) of interstitial voids between adjacent vesicles (as shown qualitatively in the 2D transverse slices of Fig. 7(C and D)). For 2.5% mol biotin vesicle–vesicle contacts were point-like. For 10% mol biotin vesicle contacts were larger (similarly to the behavior described for vesicle doublets) and the interstitial fluid was reduced. Experimentally, measuring the interstitial fluid in the interior of the aggregates was a challenging task. Instead, we measured the contact angle at the aggregate boundaries (θ_{out}) on a transverse slice, which is another indicator for aggregate cohesion.[18,60] $\theta_{\text{out}} = (11.1 \pm 1.2)^\circ$ for vesicles with 2.5% mol biotin and $\theta_{\text{out}} = (30 \pm 11)^\circ$ for 10% mol. The latter, corresponds to the largest values of the outer contact angle that we observed for SA–biotin mediated vesicle aggregation (for all tested biotin contents and X ratios). We use this measure only as a qualitative indicator, as the contact angle may vary with the topology of the aggregate (coordination number of vesicles) and also due to vesicle polydispersity. A complete quantitative characterization of aggregate packing would require the full description of the topology of the microstructure (coordination number of each vesicle, number of neighbours, local packing fraction) based, for example, on space tessellation methods,[57,58] which is out of the scope of the present paper. Interestingly, vesicle–vesicle aggregation mediated by DNA complementary chains enabled the formation of aggregates with larger degrees of cohesion. Vesicle–vesicle adhesion was tuned by varying the concentration of the complementary DNA strands (in equimolar proportions) for a given vesicle volume fraction of vesicles of 0.125% v/v. The contact angles measured for vesicle doublets increased with DNA concentration up to maximal values comparable for those obtained when using the SA–biotin pair (Fig. 3). The cohesion of the vesicle aggregates was found to greatly vary with DNA concentration. In Fig. 7(E–H) we show two representative examples of two aggregates obtained at different DNA concentrations (32 nM, panels E and G, and 644 nM, panels F and H). At low DNA concentration the contacts between vesicles are of reduced size ($\theta_{\text{out}} = (32 \pm 3)^\circ$) and interstitial voids are visible between neighboring vesicles. At larger DNA concentrations, the contacts are larger with almost no interstitial voids and the boundaries of the aggregate become smoother ($\theta_{\text{out}} = (68 \pm 6)^\circ$). Such degrees of prototissue cohesion were never achieved with the biotin-SA pair.

In DNA-mediated assemblies there is a larger number of degrees of freedom for vesicle–vesicle binding. First, the typical binding energies of DNA complementary strands are half the energies for SA–biotin (35 *vs.* $18.3k_BT$ for the binding affinity in solution), and the length of the DNA spacer is three times larger than for PEG (14.5 nm *vs.* 6 nm) enabling to reach a larger number of accessible sites. Second, the anchoring of binders to lipid membranes is less strong (a cholesterol of 27 carbon groups *vs.* a DSPE with 41), favoring the detachment and reattachment of DNA strands from lipid bilayers.[48] In addition, the number of ligands per vesicle that can be reached using DNA strands is considerably larger, as there are no geometrical constraints caused by the presence of SA molecules around vesicle membranes, so that a larger number of bonds could be formed (disregarding the formation of loops). Altogether, we conceive that the larger flexibility offered by the DNA-mediated strategy allows ligands to rearrange in time, favoring larger intra-aggregate adhesion, and ultimately, more cohesive prototissues. Furthermore, DNA technology would be advantageous for the development of vesicle prototissues displaying programmable spatial heterogeneities. Recently, experiments based on the specificity and thermal reversibility of DNA interactions have made possible the synthesis of colloidal structures,[63] oil-in-water emulsions[64] and vesicle networks[31] with programmable architectures. In particular DNA technology would be relevant for the development of heterotypic biomimetic 2D-monolayers displaying heterogeneities in both cell types and cell adhesions, with the aim of reproducing heterotypic boundaries observed, for example, in embryonic tissues separating ectoderm and mesoderm layers.[62]

4 Conclusions

We have reported in this article the design of vesicle prototissues based on the controlled assembly of giant unilamellar vesicles, with the possibility of tuning their physical properties. Vesicle aggregation is mediated by specific adhesion interaction based on the streptavidin–biotin pair and its strength is tuned by changing the relative concentration of total SA molecules in solution to the total number of biotin molecules contained on vesicle membranes. We have identified an intermediate range of SA-to-biotin concentrations suitable for the formation of vesicle aggregation, which enables bridging between adjacent vesicles but low enough to prevent SA saturation of binding sites and consequently aggregation. By increasing biotin content on vesicle membranes, we have enhanced vesicle–vesicle adhesion and have favored the formation of aggregates of large sizes. Kinetics have a crucial role in the vesicle assembly process, as different dynamical mechanisms may take place simultaneously (frequency of vesicle–vesicle collisions, diffusion of free ligands in solution, and lateral diffusion of bound-ligands). For the range of high ligands and receptors concentrations that we have used, lateral diffusion through vesicle membranes is reduced and is not determinant for vesicle aggregation. We have shown, instead, that enhancing the probability for vesicle collisions, by bringing vesicles closer to each other, aggregate sizes can be efficiently controlled. Mean aggregate sizes can range from several vesicles up to 10^4 vesicles. GUV-aggregates display an important degree of polydispersity in size and shapes. This polydispersity could be reduced making use, for example, of micropatterns with convenient geometries. The incubation method has also allowed us to control the geometry of prototissues, and in particular, to produce 2d-vesicle monolayers, which resemble the morphology of 2d-cell monolayers. Cohesion of vesicle prototissues increases with the number of receptors on vesicle membranes, and it has been maximized by using an alternative binding method, based on complementary DNA strands. We presume higher mobility of such ligands favors intra-aggregate organization of binders, leading to larger degrees of cohesion.

We believe designing biomimetic prototissues with significant sizes, an adjustable degree of cohesion, and different spatial configurations represents a promising tool for the study of cellular tissues. In particular, the vesicle prototissues designed in the present work could be used as biomimetic analogs for the modeling of multicellular spheroids or 2d-cell monolayers, which may help to deepen the understanding of tumor metastasis and morphogenesis.

Conflicts of interest

There are no conflicts to declare.

Acknowledgements

We acknowledge R. Merindol, F. Fagotto, F. Graner and L. L. Pontani for fruitful discussions, and M. In for a critical reading of the manuscript. We thank L. DiMichele for helpful advice on DNA vesicle assembly. We thank the assistance provided by E. Jublanc and V. Diackou from the microscopy platform of the University of Montpellier (MRI). This project is supported by the Labex NUMEV incorporated into the I-Site MUSE. The project has received additional funding from the Ecole Doctorale I2S (U. Montpellier).

Notes and references

1 A. Salehi-Reyhani, O. Ces and Y. Elani, *Exp. Biol. Med.*, 2017, **242**, 1309–1317.
2 J. W. Szostak, D. P. Bartel and J. W. Luisi, *Nature*, 2001, **409**, 387–390.
3 P. Schwille, *Science*, 2011, **333**, 1252–1254.
4 P. Schwille, J. Spatz, K. Landfester, E. Bodenschatz, S. Herminghaus, V. Sourjik, T. J. Erb, P. Bastiaens, R. Lipowsky, A. Hyman, P. Dabrock, J. C. Baret, T. Vidakovic-Koch, P. Bieling, R. Dimova, H. Mutschler, T. Robinson, T. Y. Tang, S. Wegner and K. Sundmacher, *Angew. Chem., Int. Ed.*, 2018, **57**, 13382–13392.
5 S. L. Veatch and S. L. Keller, *Biophys. J.*, 2003, **85**, 3074–3083.
6 S. Kretschmer, K. A. Ganzinger, H. G. Franquelim and P. Schwille, *BMC Biol.*, 2019, **17**, 1–10.
7 V. Noireaux and A. Libchaber, *Proc. Natl. Acad. Sci. U. S. A.*, 2004, **101**, 17669–17674.
8 L. L. Pontani, I. Jorjadze, V. Viasnoff and J. Brujic, *Proc. Natl. Acad. Sci. U. S. A.*, 2012, **109**, 9839–9844.
9 S. F. Fenz and K. Sengupta, *Integr. Biol.*, 2012, **4**, 982–995.
10 T. Trantidou, M. S. Friddin, A. Salehi-Reyhani, O. Ces and Y. Elani, *Lab-on-a-Chip*, 2018, **18**, 2488–2509.
11 L.-L. L. Pontani, J. van der Gucht, G. Salbreux, J. Heuvingh, J.-F. F. Joanny and C. C. Sykes, *Biophys. J.*, 2009, **96**, 192–198.
12 D. Gonzalez-Rodriguez, K. Guevorkian, S. Douezan and F. Brochard-Wyart, *Science*, 2012, **338**, 910–917.
13 F. Fagotto, *Development*, 2014, **141**, 3303–3318.
14 T. Lecuit and L. Le Goff, *Nature*, 2007, **450**, 189–192.
15 B. Aigouy, R. Farhadifar, D. B. Staple, A. Sagner, J. C. Röper, F. Jülicher and S. Eaton, *Cell*, 2010, **142**, 773–786.
16 A. S. Smith and E. Sackmann, *ChemPhysChem*, 2009, **10**, 66–78.
17 E. Sackmann and A. S. Smith, *Soft Matter*, 2014, **10**, 1644–1659.
18 J. L. Maître and C. Heisenberg, *Curr. Opin. Cell Biol.*, 2011, **23**, 508–514.
19 H. Delanoë-Ayari, J. Brevier and D. Riveline, *Soft Matter*, 2011, **7**, 824–829.
20 S. Mantri and K. Tanuj Sapra, *Biochem. Soc. Trans.*, 2013, **41**, 1159–1165.
21 H. Bayley, I. Cazimoglu and C. E. Hoskin, *Emerging Top. Life Sci.*, 2019, **3**, 615–622.
22 S. Chiruvolu, S. Walker, J. Israelachvili, F. J. Schmitt, D. Leckband and J. A. Zasadzinski, *Science*, 1994, **264**, 1753–1756.
23 E. T. Kisak, M. T. Kennedy, D. Trommeshauser and J. A. Zasadzinski, *Langmuir*, 2000, **16**, 2825–2831.
24 P. Vermette, S. Taylor, D. Dunstan and L. Meagher, *Langmuir*, 2002, **18**, 505–511.
25 K. A. Burridge, M. A. Figa and J. Y. Wong, *Langmuir*, 2004, **20**, 10252–10259.
26 N. Stuhr-Hansen, C. D. Vagianou and O. Blixt, *Bioconjugate Chem.*, 2019, **30**, 2156–2164.
27 S. Villringer, J. Madl, T. Sych, C. Manner, A. Imberty and W. Römer, *Sci. Rep.*, 2018, **8**, 1–11.
28 P. A. Beales and T. Kyle Vanderlick, *J. Phys. Chem. A*, 2007, **111**, 12372–12380.
29 P. A. Beales and T. Kyle Vanderlick, *Adv. Colloid Interface Sci.*, 2014, **207**, 290–305.
30 M. Hadorn and P. E. Hotz, *PLoS One*, 2010, **5**, e9886.
31 M. Mognetti, P. Cicuta and L. Di Michele, *Rep. Prog. Phys.*, 2019, **82**, 116601.
32 P. Carrara, P. Stano and P. L. Luisi, *ChemBioChem*, 2012, **13**, 1497–1502.
33 T. P. De Souza, G. V. Bossa, P. Stano, F. Steiniger, S. May, P. L. Luisi and A. Fahr, *Phys. Chem. Chem. Phys.*, 2017, **19**, 20082–20092.
34 M. Wilchek, E. A. Bayer and O. Livnah, *Immunol. Lett.*, 2006, **103**, 27–32.
35 D. A. Noppl-Simson and D. Needham, *Biophys. J.*, 1996, **70**, 1391–1401.
36 P. Ratanabanangkoon, M. Gropper, R. Merkel, E. Sackmann and A. P. Gast, *Langmuir*, 2003, **19**, 1054–1062.
37 A. Karlsson, R. Karlsson, M. Karlsson, A. S. Cans, A. Stromberg, F. Ryttsen and O. Orwar, *Nat. Commun.*, 2001, **409**, 150–152.
38 G. Bolognesi, M. S. Friddin, A. Salehi-Reyhani, N. E. Barlow, N. J. Brooks, O. Ces and Y. Elani, *Nat. Commun.*, 2018, **9**, 1–11.
39 Q. Li, S. Li, X. Zhang, W. Xu and X. Han, *Nat. Commun.*, 2020, **11**, 1–9.
40 L. Parolini, B. M. Mognetti, J. Kotar, E. Eiser, P. Cicuta and L. Di Michele, *Nat. Commun.*, 2015, **6**, 1–10.
41 P. Gobbo, A. J. Patil, M. Li, R. Harniman, W. H. Briscoe and S. Mann, *Nat. Mater.*, 2018, **17**, 1145–1153.
42 M. I. Angelova and D. S. Dimitrov, *Faraday Discuss. Chem. Soc.*, 1986, **81**, 303–311.
43 C. M. Warboys, M. Ghim and P. D. Weinberg, *Atherosclerosis*, 2019, **285**, 170–177.

44 G. I. Bell, M. Dembo and P. Bongrand, *Biophys. J.*, 1984, **45**, 1051–1064.
45 E. A. Evans, *Biophys. J.*, 1985, **48**, 185–192.
46 F. Brochard-Wyart and P. G. De Gennes, *Proc. Natl. Acad. Sci. U. S. A.*, 2002, **99**, 7854–7859.
47 V. Caorsi, J. Lemière, C. Campillo, M. Bussonnier, J. Manzi, T. Betz, J. Plastino, K. Carvalho and C. Sykes, *Soft Matter*, 2016, **12**, 6223–6231.
48 O. A. Amjad, B. M. Mognetti, P. Cicuta and L. Di Michele, *Langmuir*, 2017, **33**, 1139–1146.
49 W. A. Hendrickson, A. Pähler, J. L. Smith, Y. Satow, E. A. Merritt and R. P. Phizackerley, *Proc. Natl. Acad. Sci. U. S. A.*, 1989, **86**, 2190–2194.
50 P. G. de Gennes, *Macromolecules*, 1980, **13**, 1069–1075.
51 S. F. Fenz, R. Merkel and K. Sengupta, *Langmuir*, 2009, **25**, 1074–1085.
52 A. S. Smith and U. Seifert, *Phys. Rev. E: Stat., Nonlinear, Soft Matter Phys.*, 2005, **71**, 1–11.
53 A. S. Smith and U. Seifert, *Soft Matter*, 2007, **3**, 275–289.
54 F. J. Martinez-Veracoechea and M. E. Leunissen, *Soft Matter*, 2013, **9**, 3213–3219.
55 A. Ramachandran, T. H. Anderson, L. G. Leal and J. N. Israelachvili, *Langmuir*, 2011, **27**, 59–73.
56 U. Seifert and R. Lipowsky, *Phys. Rev. A*, 1990, **42**, 4768–4771.
57 I. Jorjadze, L.-L. Pontani, K. A. Newhall and J. Brujic, *Proc. Natl. Acad. Sci. U. S. A.*, 2011, **108**, 4286–4291.
58 K. A. Newhall, L. L. Pontani, I. Jorjadze, S. Hilgenfeldt and J. Brujic, *Phys. Rev. Lett.*, 2012, **108**, 268001.
59 H. Turlier and J. L. Maître, *Semin. Cell Dev. Biol.*, 2015, **47-48**, 110–117.
60 M. L. Manning, R. A. Foty, M. S. Steinberg and E. M. Schoetz, *Proc. Natl. Acad. Sci. U. S. A.*, 2010, **107**, 12517–12522.
61 K. Alessandri, B. R. Sarangi, V. V. Gurchenkov, B. Sinha, T. R. Kiessling, L. Fetler, F. Rico, S. Scheuring, C. Lamaze, A. Simon, S. Geraldo, D. Vignjevic, H. Domejean, L. Rolland, A. Funfak, J. Bibette, N. Bremond, P. Nassoy, T. R. Kießling, L. Fetler, F. Rico, S. Scheuring, C. Lamaze, A. Simon, S. Geraldo, D. Vignjević, H. Doméjean, L. Rolland, A. Funfak, J. Bibette, N. Bremond and P. Nassoy, *Proc. Natl. Acad. Sci. U. S. A.*, 2013, **110**, 14843–14848.
62 F. Fagotto, *Curr. Top. Dev. Biol.*, 2015, **112**, 19–64.
63 M.-P. Valignat, O. Theodoly, J. C. Crocker, W. B. Russel and P. M. Chaikin, *Proc. Natl. Acad. Sci. U. S. A.*, 2005, **102**, 4225–4229.
64 L. Feng, L.-L. Pontani, R. Dreyfus, P. Chaikin and J. Brujic, *Soft Matter*, 2013, **9**, 9816.

Electronic Supplementary Material (ESI) for Soft Matter.

Supplementary Information: Design of vesicle prototissues as a model for cellular tissues

Laura Casas-Ferrer, Amaury Brisson, Gladys Massiera, and Laura Casanellas

1 Size distribution of vesicles obtained by electroformation

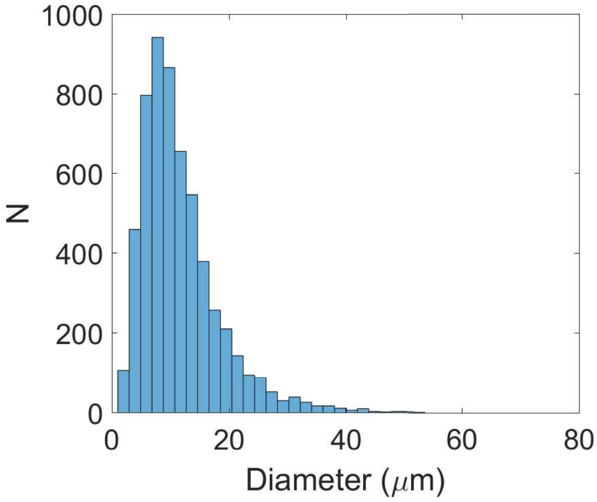

Fig. S 1: The average radius of the electroformed vesicles is $r = 6 \pm 3$ μm.

2 Details for DNA assembly

The DNA linkers consisted in a cholesterol-TEG anchor which enabled the grafting of the molecule to the vesicle membrane, followed by a backbone made of DNA double strand (DNAds) with a length of 43 base pairs that acted as a spacer and was ended with a 9 base pair sequence of single stranded DNA (DNAss), also called *sticky end*. The interaction of a sticky end (a) with its complementary strand (a') composed of complementary base pairs was the mechanism driving the assembly of the vesicles. We used the following DNA sequences (ds) designed by Parolini *et al.* [1] and were synthesized by Integrated DNA Technology:

- (a) 5-GGATGGGCATGCTCTTCCCGTTTTTATCACCCGCCATAGTAG A [Sticky End]-3
- (b) 5-CTACTATGGCGGGTGATAAAAACGGGAAGAGCATGCCCATCC AAAA [Cholesterol TEG]-3

Upon arrival, the lyophilized samples were diluted in IDTE pH 8.0 1X TE Solution (IDT) at a concentration of 100 μM, and stored at -20 °C for a maximum of one year. To prepare the DNA linkers for the assembly, we first hybridized the molecule containing the DNAss-sticky end (a) with the molecule containing the cholesterol-TEG anchor (b). To hybridize the DNA strands, we diluted them to 1.6 μM in the same TE buffer with 100 mM NaCl (Sigma Aldrich, S9888) and mixed to a ratio 1:1 sequences (a) and (b) for one assay, and (a'):(b) for the other one. A temperature ramp was performed from $90°$C down to $20°$C for a duration of 5h. By diminishing the temperature, the complementary base pairs of both (a or a') and (b) bond together forming the DNAds part of the molecule (a-b and a'-b). The hybridized DNA strands were stored at 4 °C and used for a maximum of one month. To bind the hybridized DNA molecules to the membrane of the vesicles and enable the assembly of neighboring vesicles in aggregates, equal quantities of DNA complementary strands (a-b) and (a'-b) were mixed at concentrations 32 nM and 644 nM in a mix containing IDTE pH 8 buffer, a vesicle volume fraction of 0.125%, glucose 70 mM, NaCl 80 mM, and SYTO 64 2 μM (Thermo Fisher, $\lambda_{abs} = 599$ nm, $\lambda_{em} = 619$ nm).

3 Fluorescence intensity of vesicle membranes

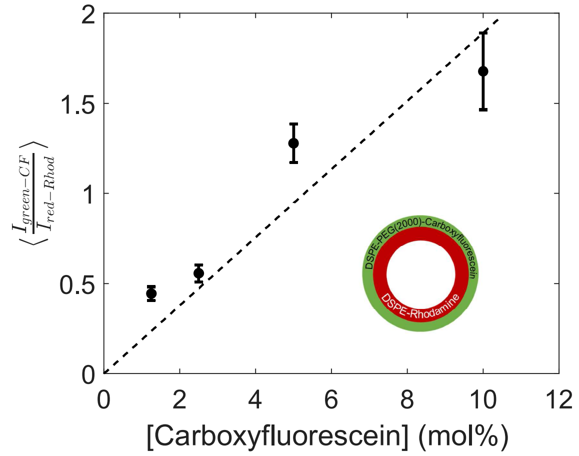

Fig. S 2: Quantification of the fluorescence intensity of vesicles containing a varying content of green fluorophore Carboxyfluorescein (from 1.25 to 10 % molar) and a constant content of DSPE-Rhodamine (red) of 1 %. The fluorescence intensity is reported as the ratio of the green over the red intensities. A linear fit is represented with a dashed line ($I_{\frac{green-CF}{red-rhod}} = 0.19[CF]$). The number of vesicles analyzed for all conditions was set to N=20. The displayed values are the average, with the standard error as the error bars.

4 Calculation of contact angle for vesicle doublets

In order to calculate the contact angle of vesicle doublets two circles were manually fitted to the vesicles forming each doublet, from which the position of their centroids (x_1, y_1 and x_2, y_2) as well as their radii (R_1, R_2) were identified (a sketch of a vesicle doublet is shown in Fig. 3). The distance between the centroids of the circles is d. The contact angle (θ) between the two overlapping circles was computed according to:

$$x = x_2 - x_1 \; ; \; y = y_2 - y_1 \tag{1}$$

$$d = \sqrt{x^2 + y^2} \tag{2}$$

$$h = \frac{1}{2d}\sqrt{4d^2{R_1}^2 - (d^2 - {R_2}^2 + {R_1}^2)^2} \tag{3}$$

$$\theta_1 = \arcsin\left(\frac{h}{R_1}\right)\ ;\ \theta_2 = \arcsin\left(\frac{h}{R_2}\right) \tag{4}$$

$$\theta = \frac{\theta_1 + \theta_2}{2} \tag{5}$$

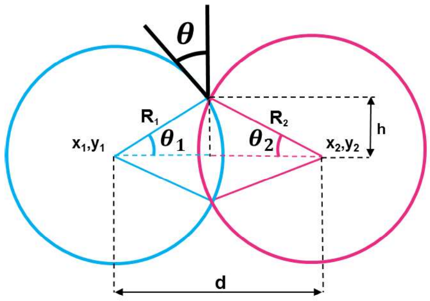

Fig. S 3: Sketch of a vesicle doublet.

5 Contact angle of vesicle doublets

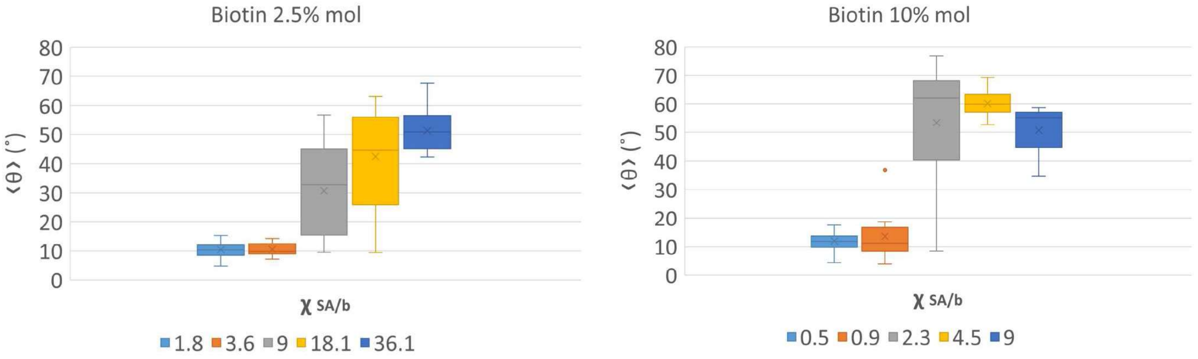

Fig. S 4: Contact angle (θ) of vesicle doublets, displayed in Fig. 3A, represented in the form of box-plots. Contact angle as a function of X, and for 2.5 % (left) and 10 % (right) mol biotin contents. The contact angle was computed by averaging the two contact angles of the doublet. The number of doublets analyzed for all conditions was set to $N = 20 \pm 4$.

References

[1] L. Parolini, B. M. Mognetti, J. Kotar, E. Eiser, P. Cicuta and L. Di Michele, *Nature communications*, 2015, **6**, 1–10.

Chapter 4. Flow behavior of the vesicle prototissue.

In this Chapter the aspiration microfluidic experiments performed using vesicle prototissues will be presented. In Table 3 there is a summary of all the experiments performed, with the experimental conditions used for the aspiration, as well as the typical size of the aspirated aggregates. ΔP_{pass} is the pressure at which the aggregates flowed through the microfluidic constriction, and Δt_{pass} corresponds to the time required for the aggregate front to advance from the entrance to the exit of the constriction. W_{agg}/W_c is the width of the aggregate W_{agg} (in the direction orthogonal to the flow) before entering the constriction relative to the width of the constriction W_c. Depending on how the pressure was applied to the system we distinguished between two protocols: *Constant*, in which the pressure was not changed during the aspiration experiment, and *Increase*, in which the pressure was periodically increased throughout the experiment. The perimeter and area of the aggregates before entering the constriction are also indicated for the *Constant* pressure protocol. The aggregates that were treated with the *Increase* protocol were too large to fit inside the field of the camera and therefore their area and perimeter could not be measured. In the last column, a summary of the characteristic rheological behaviors listed from 1 to 6 observed for each aggregate is provided. (1) corresponds to Elastic deformation (4.2.3.), (2) to Stick-and-slip behavior (4.1.4), (3) to Viscoelastic behavior (4.1.1), (4) to Plastic deformation and rearrangements (4.1.2), (5) to Rupture and filaments (4.1.3) and (6) Oscillatory behavior (4.1.4). The number between parenthesis is the section of the Chapter in which the behavior is detailed. In all the experiments, the vesicles had 10% mol/mol biotin-lipid on their membranes, the streptavidin-biotin ratio X was 0.90 and the vesicle volume was set to $4 \cdot 10^8\ \mu m^3$. The samples were incubated by using the centrifugation protocol and left for 2h at room temperature before performing the aspiration experiments. The width of the constriction W_c was 50$\pm$2 µm and the height of the channel h was 40 µm. The resulting flow responses will be qualitatively and quantitatively characterized in sections 4.1 and 4.2 of the Chapter, respectively.

4.1. Phenomenology of the flow.

In this section a qualitative description of the different types of behaviors observed for the flow of vesicle prototissues will be presented: viscoelastic response, plastic irreversible deformation, and the occurrence of vesicle-vesicle rearrangements. Other phenomena that accompany these main flow responses are the rupture of aggregates, the formation of filaments, and the oscillatory motion which can be periodic or intermittent (stick-and-slip).

	ΔP_{pass} (mbar)	Δt_{pass}(s)	W_{agg}/W_c	Perimeter $\cdot 10^2$ (µm)	Area $\cdot 10^4$ (μm^2)	Protocol	Behaviors observed
	0.26	1.3	1.3	3.4	1.7	Constant	1
	0.34	12.5	1.5	2.9	1.7	Constant	1
	0.36	4.5	1.6	3.5	2	Constant	1,2
	0.34	8.1	1.7	4.5	2.5	Constant	1
	0.28	4.3	2	4.4	2.8	Constant	1
	0.35	1.9	2.1	4.9	2.9	Constant	1
	0.36	4	2.5	3.6	2.6	Constant	1,2
	0.20	0.2	3.3	4.6	3	Constant	1,2
	0.17	2.9	3.4	5	3.7	Constant	1
F	0.27	54	3			Increase	3,4,6
E	1.49	145	3.4			Increase	3,4
D	0.50	50.4	3.6			Increase	3,4
C	0.80	37.2	3.8			Increase	3,4,5
B	1.33	104.9	3.9			Increase	3,4,6
A	0.37	78.4	4			Increase	3,4,5

Table. 3. Table displaying the main parameters of the aggregate aspiration experiments. For all of them, the vesicles had 10% mol/mol biotin-lipid on their membranes, the SA-biotin ratio X was 0.90 and the vesicle volume was set to $4 \cdot 10^8\ \mu m^3$. The samples were incubated by using the centrifugation protocol and left for 2h at room temperature before performing the aspiration experiments. The different observed aggregate behaviors are: (1) Elastic deformation (4.2.3.), (2) Stick-and-slip behavior (4.1.4), (3) Viscoelastic behavior (4.1.1), (4) Plastic deformation and rearrangements (4.1.2), (5) Rupture and filaments (4.1.3), (6) Oscillatory behavior (4.1.4).The experiments are ordered in increasing values of W_{agg}/W_c. The letters on the first column correspond to the panels displayed in Figure 43 of this Chapter.

4.1.1. Viscoelastic response

The response of a viscoelastic material to a constant applied stress is a fast elastic deformation followed by a slow viscous flow, as mentioned in Chapter 1. The viscoelastic response of a vesicle aggregate upon application of an external pressure is shown in Figure 34. At t = 0, an aggregate with a vertical width W_{agg} is placed in the entrance of the constriction, which has a width W_c . There is no applied pressure and the aggregate is not deformed. Once a pressure step of 0.1 mbar was applied, the aggregate front advanced inside the channel forming a protrusion with a width equal to W_c. The length of the protrusion was defined from the entrance of the constriction L_0 to the maximal advancement for a given applied pressure L. Right after applying the stress, it was possible to observe a fast, slight advancement of the aggregate front, which corresponded to the elastic deformation regime. A quantitative analysis of this viscoelastic response will be provided in section 4.2.4. This behavior was observed in aggregates with a typical size W_{agg} significantly larger than that of the microfluidic constriction W_c. Aggregates with typical sizes comparable to W_c displayed a predominantly elastic response, which will be detailed in section 4.2.3.

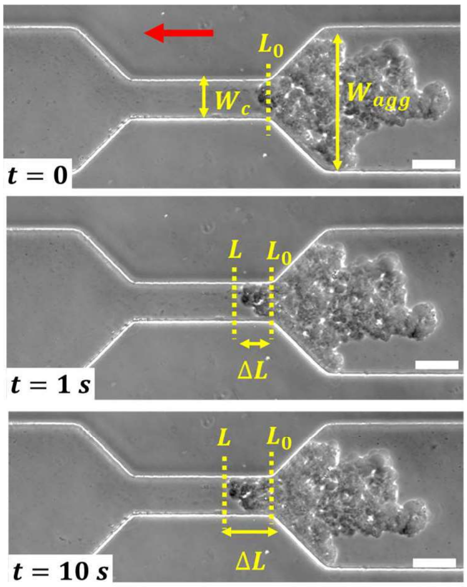

Fig. 34. Example of a vesicle prototissue with size $W_{agg}/W_c = 3.7$ flowing through a microfluidics constriction by applying a pressure *Increase* protocol. The red arrow indicates the direction of the flow. A pressure of 0.1 mbar was applied at t=0 s and held for a time interval of 10 s. Scale bar 50 μm.

4.1.2. Vesicle rearrangements and prototissue plastic response.

A plastic response occurs when a material has been deformed beyond its elastic response limit, which takes place above a certain stress value. Such plastic deformation implies topological changes in the microstructure of the material. In the case of cellular materials, such as foams or tissues, those changes correspond to cell rearrangements, also known as T transitions, which have been reviewed in Chapter 1. The consequence of rearrangements at the macroscopic scale is the irreversible deformation that we are able to observe in large aggregates after passing through the constriction. We have been able to identify T1 rearrangements in the microfluidic flow of vesicle prototissues thanks to epifluorescence video-microscopy. Figure 35 shows a T1 transition. In a T1 transition vesicles 2 and 3 are initially in contact by one edge. Upon application of an external stress, vesicles 1 and 4 displace vesicles 2 and 3 further apart, until they lose their contact. A new edge between vesicles

1 and 4 is generated, giving place to a new organization of the material. The timescale of the rearrangement observed in our experiments is of about 0.5 s.

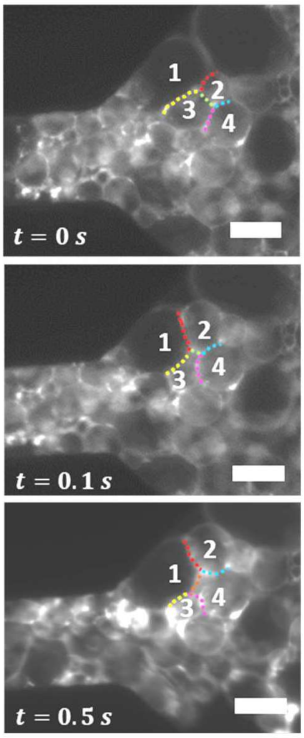

Fig. 35. Example of a vesicle rearrangement observed in the biomimetic tissue flowing through the microfluidic constriction. In a T1 transition, the edge between vesicles 3 and 2 (green) disappears to give place to a new edge between vesicles 1 and 4 (orange).

As described in Chapter 1, the microstructure of the vesicle prototissue consists in vesicles with a lipidic membrane containing a fraction of biotinylated phospholipids which can attach to each other via streptavidin. The molecular mechanisms leading to vesicle rearrangements may thus be attributed to the breaking and renewal of new streptavidin-biotin bonds, or to the detachment of biotinylated phospholipids from the lipid bilayer and reinsertion into a new position within the membrane. Epifluorescence video-microscopy allows us to identify rearrangements but this process is difficult as the fluorescence coming from the out-of-plane parts of the aggregate blurs the visualization of the vesicles, complicating the process of clearly identifying their respective edges and neighbors. Confocal microscopy, with its ability to illuminate a smaller volume of the sample and collect only the light of the in-plane vesicles, would provide a more accurate analysis of rearrangements and would allow us to perform quantitative measurements of, for example, the rearrangement rate, or to correlate the deformation of vesicles with the occurrence of rearrangements. This is, however, out of the scope of the Thesis and will not be further discussed.

As mentioned, rearrangements produce an irreversible change in the structure of a material. These changes are visible in large aggregates, as shown in Fig. 36. This figure shows an example of two vesicle aggregates displaying an irreversible deformation after passage through the constriction. As the aggregates flow through the constriction they deform, giving place to an elongated shape, and after the imposed stress is released (the aggregate exits the constriction), the aggregates do not regain their original shape but they keep the typical size of the channel constriction. There is a negligible size recovery in time, for at least 20 s. In Fig. 36A, the relative change on the aggregate´s deformation can be estimated as the difference of the vertical axis of the aggregate before (W_i) and after (W_f) passing through the constriction as $\Delta W_{agg} = \frac{W_{agg}f - W_{agg}i}{W_{agg}i} \cdot 100$. The calculation of this value reveals a loss of the 63% of the aggregate width upon deformation, which means that the aggregate remains largely deformed after the stress is released.

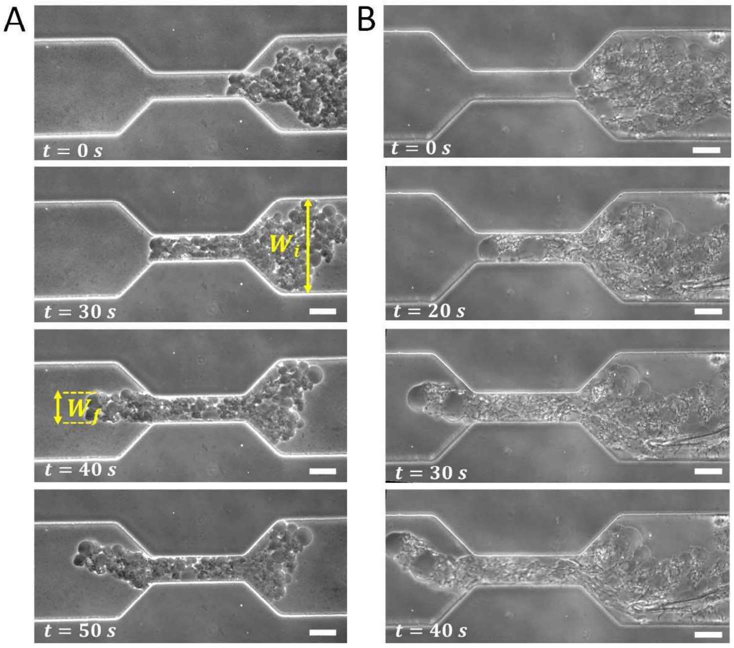

Fig. 36. Image sequences displaying the deformation of two aggregates with dimensions (A) $W_{agg}/W_c = 3.5$ and (B) $W_{agg}/W_c = 4$, in intervals of 10 s. Scale bar 50 μm.

4.1.3. Aggregate rupture and filament formation.

Rupture is the process by which a material splits in two or more parts because it is unable to deform, neither elastically or plastically, as a response to an applied stress. Aggregate rupture has been observed in some of the microfluidic aspiration experiments, as exemplified in Fig. 37A. The figure shows an aggregate fragmenting in two different parts as it is aspirated through the constriction. We had observed aggregate rupture in large aggregates compared to the constriction size, and especially aggregates which had vesicles with large diameters (> 40 μm) within their structure. Aggregate rupture occurred at long time scales (80 - 100 s after the start of the aspiration) which correspond to high-pressure values (> 0.6 mbar). When subjected to these conditions, aggregates might reach a critical stress for tissue failure. Along with rupture, it was also possible to see the formation of filaments connecting the two parts of the aggregate, which was visible in epifluorescence microscopy thanks to the fluorescently labelled streptavidin molecules that coat the surface of the vesicle membrane. For this reason, we hypothesize that that the rupture of the aggregate is due to the pulling of biotinylated lipids out of the vesicle membrane rather than to the breaking of streptavidin-biotin bonds.

In the microfluidic experiments, the typical length scales observed for these filaments range from 20 to 50 μm, as shown in Figure 37 A and B respectively. Membrane tubes or tethers are naturally formed in cells during processes involving motility and membrane remodeling, like endo and exocytosis, division, migration, and substance transport, and they are a tool for intra and intercellular communication [133]. Membrane tethers can also be used as a tool to measure the bending rigidity and membrane tension of vesicles. Such studies have been pursued by using a combination of micropipette aspiration and optical tweezers [59] or by combining micropipette aspiration and hydrodynamic flow [134]. The underlying interest of using these methods is their high sensitivity, which allows them to probe energies as low as 10-20 k_BT.

Tissue rupture is a crucial event in biology. In pathology, tissue rupture can be a result of a traumatic event generated by external or internal forces. As a result of an externally applied force, the tissue might tear, giving place to a malfunctioning and possible death of the organism. For this reason, there are tissues like the epithelium of the urinary bladder or the lungs that become specialized in avoiding rupture, since they have to withstand large strains and stresses in physiological conditions. An example of rupture by an internally applied force that gives place to a pathological condition is tumor fragmentation, which usually implies an imminent metastasis [105]. In a normally functioning tissue, rupture is a process that is sometimes necessary in order to maintain the correct homeostasis of the organism. For example, in morphogenetic development, the partitioning of the tissue into different units is a crucial step that organisms need to overcome in order to advance in the embryogenesis process [135].

4.1.4. Stop-and-go motion

The stop-and-go motion occurs when an object that is dragged along a surface at a constant force displays cycles of advancement and rest. This behavior can result from the friction forces between the surface and the object that is being displaced on it. We observed two different kinds of stop-and-go motion: periodic oscillations and stick-and-slip. In periodic oscillations, the aggregate advanced and retracted approximately the same length in regular time intervals. In stick and slip, the aggregate moved a certain distance for a brief period of time and then stopped, and did so in irregular time and space intervals. Note that in order to avoid interaction of the aggregates with the channel walls, we treated the surfaces with β-casein prior to the aspiration experiments. This treatment avoided unspecific interactions between the vesicles and the surfaces which could induce an additional friction between the channel walls and the aggregate. Without the β -casein treatment, we observed that aggregates indeed sticked to the channel walls and their advancement through the constriction was heavily impaired. The stop-and-go motion described in this section was observed even when the surface treatment was performed.

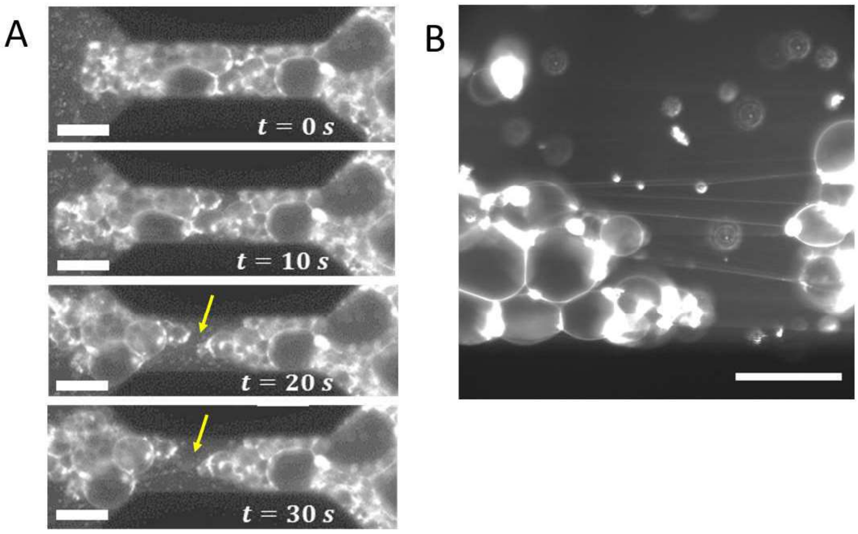

Fig. 37. Image sequences displaying filaments in aggregates during the process of aggregate rupture. A. Time lapse displaying the rupture of an aggregate in two parts, which remain linked by a filament, with a length of 40 µm when t= 30 s. The filament is indicated with a yellow arrow. Scale bar 50 µm. B. Multiple filaments between two parts of a teared aggregate, with a typical lengthscale of 50 µm. Scale bar 25 µm.

Whereas periodic oscillations were visible when the aggregate entered the constriction, stick-and-slip phenomena occurred when the aggregate was inside the constriction. Fig. 38A shows an example of the oscillations observed for an aggregate entering the channel constriction, exploring a distance of 5 μm with a frequency of approximately 10 s^{-1}. Fig. 38B displays an example for an aggregate with stick-and-slip behavior. The aggregate advanced intercalating static (stick) and dynamic (slip) phases. For this particular example, the static phase lasted for approximately 100 ms, and in the dynamic phase the aggregate advanced fast, exploring a distance of 50 μm in a time interval of 75 ms. Stick and slip motion is a common phenomenon in adhesive systems, either passive or active. Cells advancing on an adherent substrate are an example of an active system displaying this type of behavior: the counterforce between actin retraction and extension of the membrane lamellipodia towards the direction of movement produces intermittent advancing cycles [136]. Leucocytes advancing through the blood vessel endothelium before extravasation into the target tissue also display this type of behavior [137].

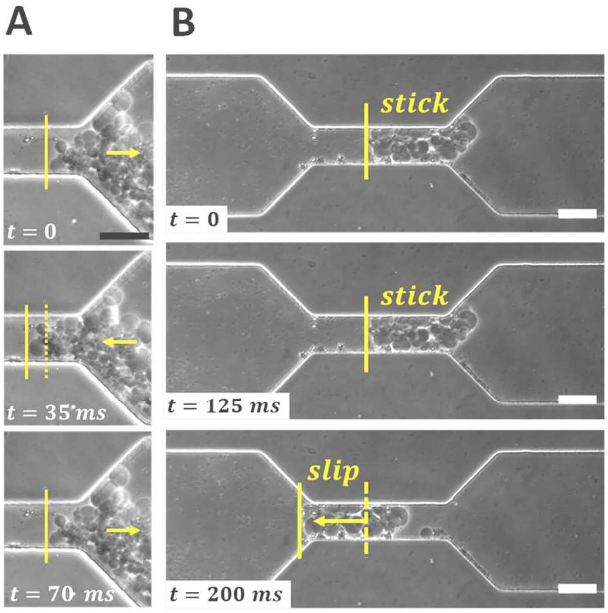

Fig. 38. Aggregates displaying two types of stop-and-go motion: A. Periodic oscillations and B. Stick and slip. The dotted lines represent the starting position of the front of the aggregate, and the filled lines the displacement of the aggregate front. The arrows represent the direction in which the aggregate moves. Scale bar 50 μm.

4.2. Quantitative analysis of the flow behavior.

We aim to characterize the rheological properties of vesicle prototissues and to understand the role of the aggregate size on their flow behavior. First, we quantified the necessary pressure for the aggregates to pass through the constriction (4.2.1) and their hydraulic resistance (4.2.2). Second, we determined the change in shape and area of aggregates with moderate sizes before and after passage through the microfluidic constriction (4.2.3). Last, in section 4.2.4, we determined the rheological properties of large aggregates by analyzing the advancement of the aggregate protusion in time and for increasing pressure steps.

4.2.1. Influence of the aggregate size in the pressure of passage.

The first parameter that we quantified was the pressure needed to make the aggregates flow through the microfluidic constriction, that we name ΔP_{pass}. We used two different protocols depending on the size of the aggregate. As described in Chapter 2, for aggregates with moderate sizes we used the *Constant* pressure protocol, and for aggregates with larger sizes we used the pressure *Increase* protocol. Fig. 39A shows the pressure of passage ΔP_{pass} as a function of the area of the aggregate A_{agg} normalized by the section of the constriction S_c. A_{agg} is measured as the 2D projection of the aggregate before it enters the constriction, and S_c is the section of the channel constriction calculated as the product of the height of the channel (h) and the constriction width, W_c. Circles correspond to the experiments performed at constant pressure and triangles to the ones at increasing pressure steps. Since we can observe that the values obtained for ΔP_{pass} are scattered and there is no clear trend with the rescaled aggregate area, we decided to characterize the size of the aggregate in terms of the vertical axis W_{agg}. This parameter gives a quantification of the size of the aggregate orthogonal to the flow, which is the spatial dimension that is more likely to limit its passage through the constriction of width W_c.

In Fig. 39B the pressure of passage is thus plotted as a function of W_{agg}/W_c. Note that the maximal possible value for W_{Agg}/W_c was set by the ratio between the width of the channel (prior to constriction) and the width of the constriction, since the aggregates were confined inside the channel. This maximal value corresponds to $W_{Agg}/W_c = 4$. Aggregates with widths ranging from 1 to 3.5 W_{Agg}/W_c display a low pressure of passage, below 0.5 mbar. As the width of the aggregate approaches its maximal value ($W_{Agg}/W_c > 3.5$) the pressure values become scattered, and we obtained a range of ΔP_{pass} going from 0.5 to 1.5 mbar. Small aggregates would need lower ΔP_{pass} values because they needed to deform slightly to flow through the constriction. Contrarily, large aggregates would need higher ΔP_{pass} values in order to partially compress and get inserted inside the constriction. However, the flow behavior observed for some particular aspiration experiments do not follow this general trend. The data highlighted in a blue circle in Fig. 39B correspond to aggregates which have a large size, with W_{Agg}/W_c values 3.3 and 3.4, but display low pressure of passage.

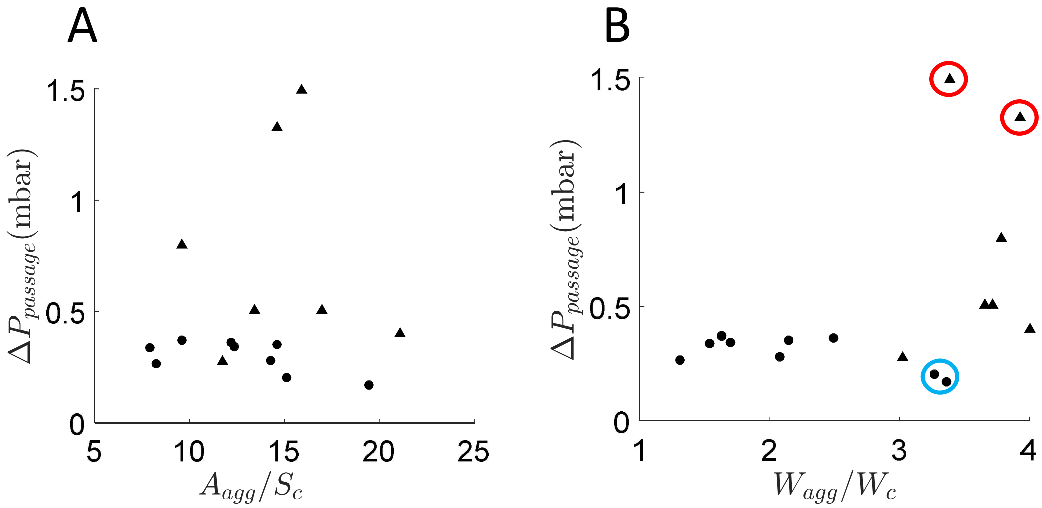

Fig. 39. Graph displaying the pressure of passage ΔP_{pass} as a function of the size of the aggregates, in terms of the rescaled area (A) or width (B). Circles correspond to experiments performed at *Constant* pressure and the triangles to experiments performed at *Increasing* pressure steps. The aggregates which display behaviors that do not follow the general trend are highlighted with colored circles. Red circles correspond to large aggregates that display an abnormally high ΔP_{pass} and blue circles indicate large aggregates with an unusually low ΔP_{pass}. The error of ΔP_{pass} corresponds to the precision of the pressure control system and is of ± 0.01 mbar (error bar not shown).

For these particular experiments, it was possible to observe that even though the aggregates had a large vertical dimension (W_{Agg}), their horizontal dimension was small compared to the constriction size. This irregular morphology allowed the aggregates to fold inside the constriction as soon as they entered it without creating any plug. Thus, these aggregates managed to flow easily through the constriction despite their large W_{Agg} value. This behavior is illustrated in Figure 40.

As mentioned before, the values for ΔP_{pass} belonging to large aggregates is scattered. Most values are comprised between 0.4 and 0.8 mbar, but there are two outliers with a pressure of passage of 1.5 and 1.25 mbar, highlighted in red in Fig. 39B. In these aspiration experiments a significant background flow was in place, which could be visualized by the motion of particles of the surrounding fluid which passed through the channel constriction. If the aggregates did not completely plug the constriction it could result in a loss of effective pressure through the background fluid, requiring a higher ΔP_{pass} in order to force their passage through the constriction. This topic will be further developed by comparing the aspiration experiments results and the background fluid velocity calculated for each of these experiments in section 4.2.4 of this Chapter.

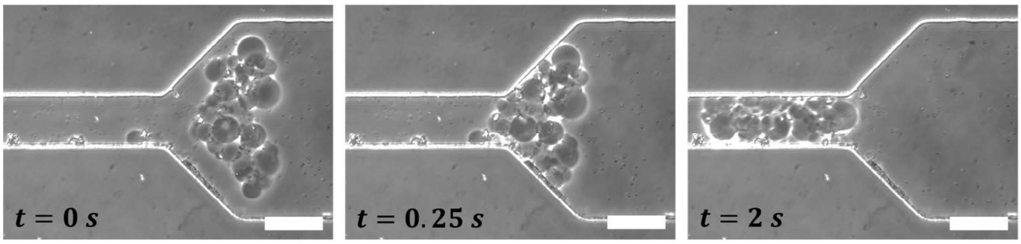

Fig. 40. Image sequence of an aggregate with W_{Agg}/W_c =3.4 that flows with a ΔP_{pass} of 0.22 mbar. The morphology of the aggregate allows to fold inside the constriction despite its large size in the vertical axis. Scale bar 50 µm.

4.2.2. Influence of the aggregate size in the time of passage and hydraulic resistance.

In the following analysis, we determine the time that aggregates took to travel through the whole constriction length. It is defined as Δt_{pass}, which corresponds to the time that it takes for the front of the aggregate to go from the entrance of the constriction L_0 to its end. At this point, the length of the protrusion L equals the length of the constriction L_c. The time of passage is indicative, together with the pressure of passage, of the resistance offered by the vesicle aggregate to flow through the constriction. Figure 41A displays Δt_{pass} as a function of the aggregate size, expressed as W_{agg}/W_c. The right vertical axis, in red, displays the ΔP_{pass} value for each aggregate. The circles correspond to the aggregates aspirated with the *Constant* pressure protocol and the triangles to the aggregates aspirated with the *Increase* pressure protocol. In general, aggregates with sizes comparable to that of the constriction width, W_c, have lower Δt_{pass} values than large aggregates ($W_{agg}/W_c > 3.5$). In a similar way, we can observe that aggregates that have a lower Δt_{pass} also present a lower ΔP_{pass}. Small aggregates need less time and a lower pressure value to pass through the constriction because they have a smaller volume to deform, whereas large aggregates have a higher volume and need longer times and higher pressure values to flow through the same constriction.

In order to take into account both the time and pressure of passage we compute the hydraulic resistance R_{hyd}. The hydraulic resistance is the resistance offered by a liquid with a certain viscosity to flow through a channel with a given geometry. This resistance is due to dissipation caused by the flow of the liquid itself and the friction of the liquid with the channel walls, and it is defined by Eq. (8) [138]:

$$R_{hyd} = \frac{\Delta P}{Q} = \frac{\Delta P_{pass} \cdot \Delta t_{pass}}{L_c \cdot S_c} \quad (8)$$

Where Q is the volumetric flow and ΔP is the pressure difference needed to make the fluid flow through the constriction (which in this case equals ΔP_{pass}). L_c and S_c are the length and cross-section of the channel constriction. For the microfluidic channel we used, L_c and S_c are 200 μm and 2000 μm^2 respectively. In Fig. 41B R_{hy} is represented as a function of the aggregate size W_{agg}/W_c. It is clear from the figure that the resistance to flow for large aggregates is higher than that of small aggregates. The outliers highlighted in red from the previous figure have been excluded in order to better visualize the differences between R_{hyd} from *Constant* and *Increasing* pressure experiments. In general, the hydraulic resistance R_{hyd} remains constant for aggregates with $W_{agg}/W_c < 3$, under $2 \cdot 10^{15}\ Pa \cdot s/m^3$. However, for aggregates with sizes $W_{agg}/W_c > 3$, the hydraulic resistance R_{hyd} increases linearly with the size of the aggregate, and all the values are above $3 \cdot 10^{15}\ Pa \cdot s/m^3$. The two outliers highlighted in blue correspond to the same aggregates discussed previously, which have a distinctive morphology that allows them to squeeze through the constriction at a low ΔP_{pass} despite having a large W_{agg}/W_c. In conclusion, the results show that for aggregates with moderate sizes, the hydrodynamic resistance remains practically constant, while for aggregates with sizes significantly larger than the constriction, the flow resistance increases substantially.

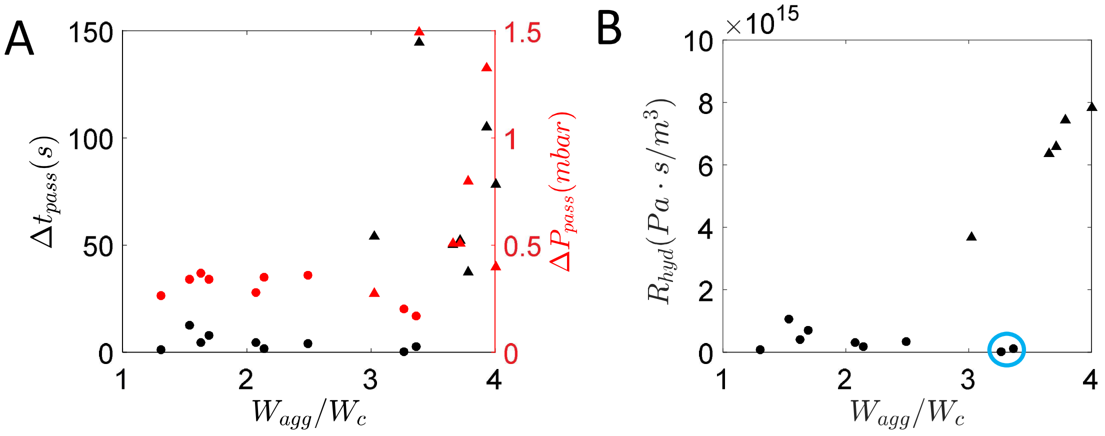

Fig. 41. A. Time of passage Δt_{pass} as a function of the aggregate size. B. Hydraulic resistance of the aggregates as a function of the aggregate size W_{agg}/W_c. Dots correspond to the experiments performed at constant pressure and the triangles to the experiments performed at increasing pressure steps.

4.2.3. Role of the size in the compression and deformation of the aggregates.

After flowing through the constriction, the aggregates may undergo a change in size and shape. A change in size would be indicative of a change in the degree of compaction of the aggregate. A change in shape would imply that the response of the aggregate is not purely elastic, which would be attributed to an irreversible plastic deformation due to occurrence of vesicle rearrangements. We are interested in tracking the changes in size and shape of aggregates of moderate size, as depicted in Fig. 42A. From right to left, the aggregate enters the constriction with an initial area and perimeter A_i and per_i. Upon passage, the aggregate squeezes and afterwards it is released from the constriction with a final area and perimeter A_f and per_f. The quantification of the size and shape changes were made by calculating the variation of area and perimeter respectively. An increase in the area of an object implies that it has expanded, whereas a decrease indicates its compaction. An increase in the perimeter of an object would imply that it displays a more elongated shape, whereas the opposite would mean that the object has become more rounded. The area and perimeter of the aggregates were measured by manually outlining the images of five aggregates before and after passing through the constriction. The mean and standard deviation were calculated and expressed as error bars in the graph. The variation in size is calculated as the difference between the area of the aggregate before (A_i) and after (A_f) passing through the constriction, normalized by the initial aggregate area ($\Delta A/A_i = \frac{A_f - A_i}{A_i}$). The change in shape is computed by measuring the differences of the perimeter before (per_i) and after (per_f) passage through the constriction ($\Delta per/per_i = \frac{per_f - per_i}{per_i}$). We make these estimations in 2D because we can assume the aggregates occupy the entire height of the channel in the z direction, since the volume of the aggregates is large enough to fill the space between the microfluidic channel and the glass coverslip.

Fig. 42B shows the relative difference in the area of the aggregates $\Delta A/A_i$ as a function of the aggregate size, expressed as W_{agg}/W_c. The range of values displayed is very small, with size variations going from -10 % to +5%. Negative variations of the area imply that the aggregate has diminished its size; in other words, that it has been compressed. A positive change in area would mean that the aggregate has expanded its volume after passage through the constriction. We assume the latter has no physical meaning in the context of our experiments, since it is not plausible that aggregates expand after being compressed. Since the values in the area variation are within the error bars, we can assume that positive area changes stem from the error due to the manual outlining of the aggregates. The fact that it is a 2D analysis may also involve some additional errors, as eventual variations in shape and size in the vertical direction are not taken into account. It is possible that, before or after

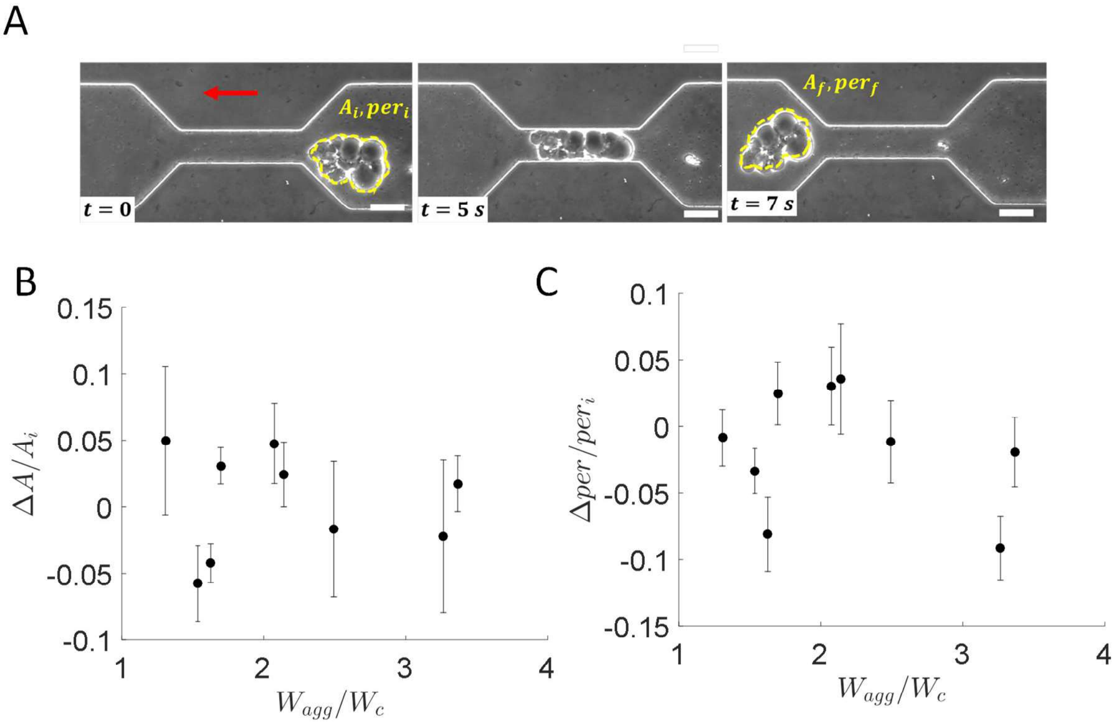

Fig. 42. A Small aggregate ($W_{agg}/W_c = 1.6$) deforming and recovering its initial shape after exiting the constriction, while applying a constant pressure of 0.22 mbar. A_i and per_i are the initial area and perimeter of the aggregate. A_f and per_f the aggregate area and perimeter after passage through the constriction. The arrow indicates the direction of the flow. Scale bar 50 µm. B. Difference on the relative mean aggregate area ($\Delta\, A/A_i$) as a function of the aggregate size. C. Differnce on the relative perimeter ($\Delta\, per/per_i$) as a function of the aggregate size.

passing through the constriction, some aggregates rotate slightly in the z direction of its axis, giving an area or perimeter which appears smaller in the XY plane. Fig. 42C shows the relative perimeter variation $\Delta per/per_i$ as a function of the aggregate size. In that case the range of values goes from -5% to +10%, which indicates a very low variation in the perimeter before and after passage through the constriction. Some negative perimeter values are found. A negative change in the perimeter would mean that the aggregate has become more rounded upon passage through the constriction, something that seems unphysical, and that we attribute once more to the error of the manual outlining of the aggregates. Taking the quantitative results and the observations into account, we can assume that the vesicle aggregates do not experience a significant change in size or shape after being deformed by passing through the constriction. Their ability to regain their initial shape after the stress is released is indicative of an elastic-dominated behavior.

In this section we have focused on aggregates of moderate sizes, ranging from 1.5 to 3.5 W_{agg}/W_c. As discussed in section 4.1.2, large aggregates display plastic behavior, which means that they experience an irreversible shape change upon application of an external stress above a certain threshold. These results highlight the plastic behavior of large aggregates (with irreversible deformation) compared to the elastic-dominated behavior of small aggregates (with reversible deformation). The reason why we were not able to analyze the change in size and shape systematically in large aggregates is because the experimental aspiration protocol used was not designed for this purpose. The video-microscopy data was obtained using a magnification of 20x, which allowed us to image the constriction but left little space for determining the total size of large aggregates before and after passing through the constriction. Another limitation of the setup was the camera speed. Large aggregates experience a pressure build-up due to the application of increasing pressure steps, which made them get ejected from the constriction at a high speed. The temporal resolution of the camera was not enough to capture events below 0.01 seconds. Therefore, the images of large aggregates exiting the constriction were blurred, leaving them unsuitable for quantification purposes. The protocol for measuring large aggregate deformation after passage through the constriction could be improved by lowering the microscope magnification to 10x or 5x, and by implementing a fast camera which would allow us to track the exit of the aggregate from the constriction at a higher frame rate.

4.2.4. Rheological characterization of the vesicle prototissue.

Progression of the protrusion length at increasing pressures

In this section, an analysis of the rheological properties of the aggregates is presented, which has been possible due to the aspiration of large aggregates at increasing pressure steps. The results obtained for the aspiration experiments are shown in Fig. 43. The figure displays the advancement of the aggregate front inside the constriction, ΔL, as a function of time for six different vesicle aggregates with sizes ranging from 3 to 4 W_{agg}/W_c. The panels are displayed in decreasing order of the aggregate size. The applied increasing pressure steps as a function of time are displayed in red. The precision of the pressure controller used is of $\pm$ 0.01 mbar. Panels A, C, E display the aspiration curves that were obtained by using epifluorescence microscopy, and Panels B, D and F show the aspiration curves obtained by phase contrast microscopy. Since the quality and the contrast of the phase contrast images is lower than the ones obtained by fluorescence microscopy, the curves obtained by using this method display larger fluctuations in the measurement of the aggregate front due to the image treatment process.

The first remarkable property of the aggregate aspiration curves is their variability. We observe a different behavior for each aggregate, which will be described in the following paragraphs. We attribute this heterogeneity to the size and morphology differences between aggregates, and also to the size polydispersity of the vesicles that form the aggregates. Panel 43C shows, for example, the curve for an aggregate with a width 3.8 times larger than the constriction size. We can see that upon application of the first pressure step, a very small increase of the protrusion length occurs, followed by a stationary phase in which the length of the protrusion front does not increase with time within the experimental resolution. In the second pressure step, however, the shape of the curve is slightly different: there is a larger, fast increase at short times, and then the length of the aggregate increases linearly with time. This curve shape is indicative of a viscoelastic behavior, which will be discussed in the following section. The third step follows the same trend as the second and, upon application of a fourth pressure step, the aggregate advances very fast until it reaches the end of the constriction, at $\Delta L = 200\ \mu m$, and then it is ejected from it.

In Panel 43A we can see a similar response to that of Panel 43C upon the application of the first pressure step. In this curve, however, a significant advancement of the front does not occur until reaching a pressure value of 0.3 mbar, in the third step. It is also important to note that the increase does not happen immediately after the pressure increase, but while it is kept constant, after approximately 8 s from the beginning of the pressure step. This might be a consequence of the stick-slip phenomena that has been discussed earlier in the Chapter. Abrupt length increases upon application of a pressure step are also observed in panels 43B, 43E and 43F at times 75, 10 0, 35 s respectively. Upon inspecting the recordings of the aspiration experiments, it was possible to observe that these increases occurred after large parts of the aggregate shifted their position, suggesting that some aggregates might need to reach a minimal pressure value in order to continue flowing through the constriction.

The aspiration curves displayed in Panels 43B and 43E are characterized by a significant number of pressure steps compared to the rest of aspiration experiments, which go up to 1.5 mbar. These aggregates did not experience a significant forward motion through the constriction until higher pressure values were reached, of 0.8 and 1 mbar respectively. When examining the video-microscopy

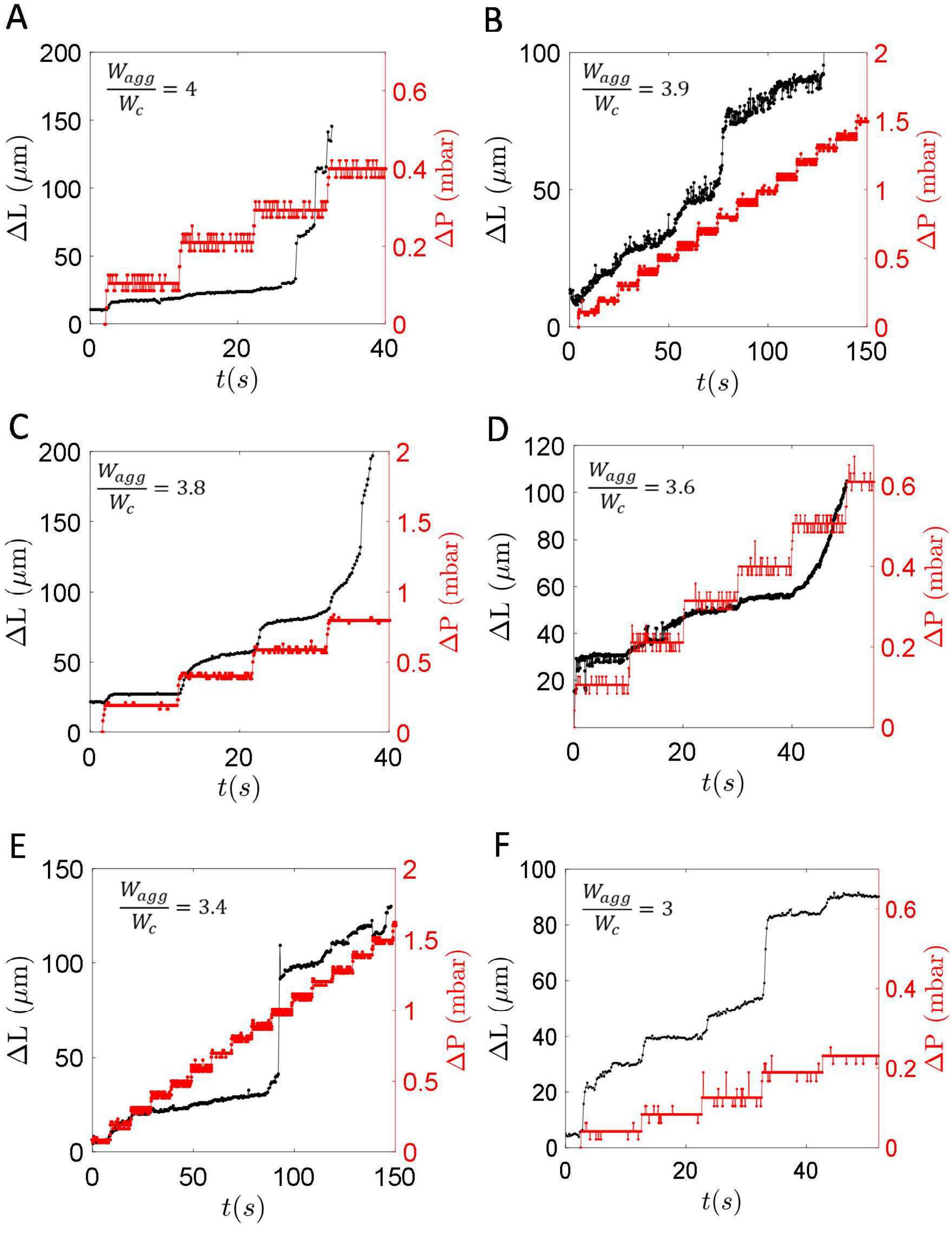

Fig. 43. Curves displaying the advancement of the aggregate front inside the constriction (ΔL) with time (t). The right axis, displays the applied pressure steps in time (red). The width of the aggregate normalized by the width of the constriction is displayed in the left upper corner of the panels. The panels are ordered in decreasing order of the aggregate size. From A to F, the velocity of the background fluid at the axis of the channel constriction is estimated to 30±10 μm/s, 30±10 μm/s, 6±4 μm/s, 70±30 μm/s, 50±20 μm/s, 60±10 μm/s.

images of the experiments, we noticed that the aggregates did not effectively plug the constriction, and when the flow in the first pressure step was measured by manual particle tracking, we did not see any significant differences compared to the other experiments. Contrarily, the video-microscopy images of the experiment displayed in Panel 43C revealed an effective plugging of the constriction, with little background flow, on only 6 μm/s. This value is significantly lower than the flow velocity of the rest of the experiments, which ranges between 30 and 70 μm/s. This reveals that an effective plugging of the constriction might be needed in order to obtain analyzable aspiration curves. One must note that the measurements performed by manual particle tracking are not completely accurate since the z position of the camera focus varies slightly on each experiment. The flow of the aqueous solution inside the constriction follows a Poiseuille profile, as explained in section 2.5. of Chapter 2, which means that in order to have comparable velocity measurements, all the experiments should have been imaged at the same z position and at the same distance from the center of the channel.

Quantification of the viscoelastic time-dependent response

In this section, a study of the viscoelastic behavior of the biomimetic tissue is presented. The properties of viscoelastic materials and the analysis of viscoelastic cell aggregates and cell monolayers have been previously discussed in Chapter 1. Therefore, only a brief explanation of how viscoelastic materials respond to an applied stress will be provided in order to facilitate the interpretation of the obtained results. The analysis is performed in the first and second aspiration steps of the curves of Fig. 43C and the first step of Fig. 43A and 43F, in order to make sure that the volume of the aggregate outside of the constriction did not change significantly.

Fig. 44A displays schematically the deformation of a viscoelastic material γ in response to an applied stress τ_0 for a time interval from 0 to t_{r0}. The deformation of a rubber, which displays an elastically dominated behavior, is displayed in a dashed line for comparison. In the viscous response regime, the deformation increases proportionally with time. A linear equation with slope $\dot{\gamma_\infty}$ and intercept γ_0 can be fitted. These parameters will allow us to calculate the viscosity (η), compliance (J), and relaxation time (t_{relax}) of vesicle aggregates, and compare them to those found in the literature for other biomimetic or biological tissues. The deformation of the vesicle aggregate to an applied stress is shown in Fig. 44B, and it corresponds to the second pressure step of Fig. 43C. We can reproduce the time-dependent response with a viscoelastic expression that takes into account a fast elastic (exponential) recovery and a creep behavior at long times, which is predicted by the simple Maxwell model (Eq.(9)):

$$\Delta L(t) = \Delta L_0 + \Delta L_{max}\left(1 - e^{\frac{-(t-t_0)}{t_{elastic}}}\right) + (t - t_0)\Delta\dot{L}_\infty \quad (9)$$

The first term of the equation corresponds to the initial length of the aggregate respect to the constriction entrance ΔL_0.The second term of the equation accounts for the elastic behavior. ΔL_{max} is the maximal deformation that the aggregate front reaches due to elastic deformation, and t_0 is the time offset between the start of the pressure ramp and the start of the aggregate deformation. The elastic time $t_{elastic}$ defines the rising time of the elastic deformation, and it is indicative of the timescale at which the aggregate transitions from elastic to viscous behavior. The third term of the equation accounts for the viscous deformation of the aggregate, $\Delta\dot{L}_\infty$ is the slope of the linear increase. The equation was fitted to the curves belonging to Fig. 43A, C and F, and the values obtained for each parameter are shown in Table 4A. The rest of the curves were not suitable for analysis because they did not show any clear deformation upon application of the first pressure step, or displayed significant fluctuations due to the image analysis treatment. The first pressure step of Fig. 43C is displayed in Fig. 44C for comparison. In this case, the response is characterized by a fast increase in the deformation upon pressure application, but after this phase the deformation does not increase linearly with time. Therefore, the deformation has a very dominant elastic component and might indicate that we are not measuring the viscoelastic properties of the aggregate.

Both the slope and the intercept of the linear equation that define the viscous deformation of the aggregate were normalized by the constriction width W_c, in order to obtain $\dot{\gamma_\infty}$ and γ_0 respectively. The applied stress τ_0 was calculated by considering a force balance between the applied pressure between the opposite ends of the constriction (times the constriction section), and the shear stress experienced on the channel walls by applying Eq. (10). :

$$\tau_0 = \frac{\Delta P W_c h}{2\,\Delta L(W_c + h)} \quad (10)$$

ΔP is the applied pressure, W_c and h the width and the height of the channel constriction, and ΔL the protrusion length of the aggregate inside of the constriction. $\dot{\gamma_\infty}$, γ_0 and τ_0 are shown in columns 3, 4 and 5 of Table 4B, respectively. Having obtained the fitting parameters from Eq. (9), we then calculated the viscosity, compliance and relaxation time of the aggregates. The viscosity η is given by the ratio between the applied stress and the terminal strain rate (Eq. (11))[139]:

$$\eta = \frac{\tau_0}{\dot{\gamma_\infty}} \quad (11)$$

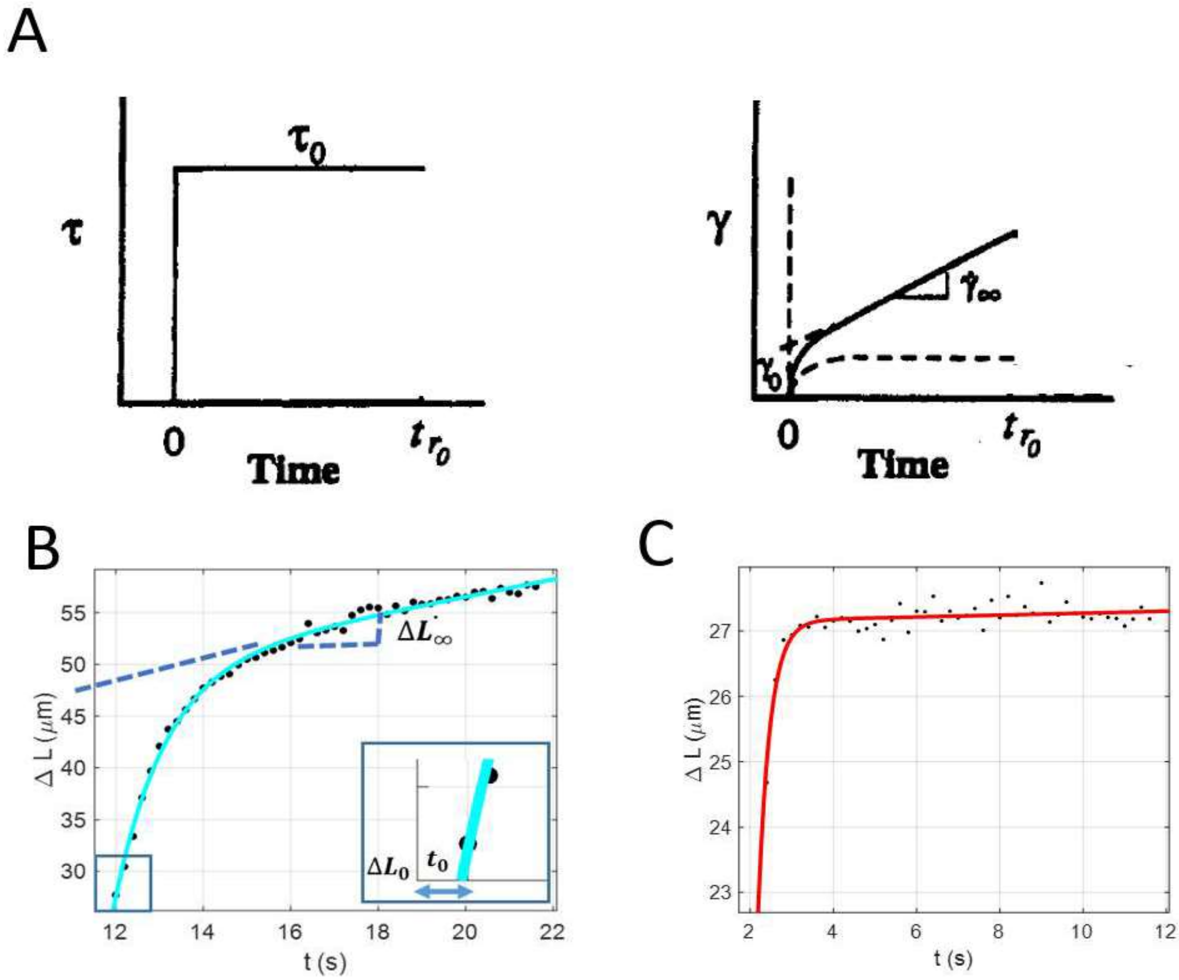

Fig. 44. A. Deformation γ of a viscoelastic material as a function of time upon application of a constant stress τ_0 from t=0 to t=t_{r0}. $\dot{\gamma_\infty}$ is the slope of the linear regime and γ_0 the intercept with the vertical axis. From [139]. B. Evolution of the aggregate front with time $\Delta L(t)$. ΔL_0 is the initial length of the aggregate with respect to the constriction entrance, t_0 is the time offset between the start of the pressure ramp and the start of the aggregate deformation, and $\Delta\dot{L}_\infty$ is the slope of the linear increase phase of the curve. The blue solid line represents the fit of Eq. (9) to the experimental data, which corresponds to the second deformation step of the aggregate displayed in Fig 43C. The applied pressure is of 0.4 mbar, and lasts for a time interval of 10 s. C. First aspiration curve of aggregate displayed in Fig. 43C, with an applied pressure of 0.2 mbar held during 10 s. The red solid line represents the fit of Eq. (9) to the experimental data.

The relaxation time t_{rela} sets the timescale necessary for the material to flow like a viscous fluid, and can be associated to vesicle rearrangements within the aggregate. It is given by Eq. (12), and it is obtained as the intercept divided by the terminal strain rate [139]:

$$t_{relax} = \frac{\gamma_0}{\dot{\gamma_\infty}} \quad (12)$$

The compliance J_0 of the material was calculated as the ratio between the intercept and the applied stress, which is given by Eq. (13) [139]. We can approximate the elastic modulus (E) as the inverse of the compliance (Eq. (14)):

$$J_0 = \frac{\gamma_0}{\tau_0} \quad (13)$$

$$E \sim \frac{1}{J_0} \quad (14)$$

A

# step	panel	$\Delta L_0\ (\mu m)$	$\Delta L_{max}(\mu m)$	$t_{elastic}\ (s)$	$t_0\ (s)$	$\Delta \dot{L_\infty}(\mu m/s)$	R-square
1st	A	10.2	6.1±(0.5)	0.5±(0.2)	2.1	0.2±(0.1)	0.8808
1st	C	22.9	4.3±(0.1)	0.3±(0.1)	2.2	0.01±(0.03)	0.9356
2nd	C	27.7	22.1±(0.8)	1.2±(0.1)	12	0.8±(0.1)	0.9956
1st	F	6.5	16.2±(2.9)	0.3±(0.1)	2.9	1.0±(0.2)	0.8535

B

# step	panel	$\dot{\gamma_\infty}\ (s^{-1})$	γ_0	$\tau_0\ (Pa)$	$\eta\ (Pa \cdot s)$	$t_{relax}\ (s)$	$J_0\ (Pa^{-1})$	$E\ (Pa)$
1st	A	0.0040	0.12	6.1	1517	31	0.02	50
1st	C	0.0002	0.09	8.1	40399	428	0.01	95
2nd	C	0.02	0.44	7.7	483	28	0.06	17
1st	F	0.02	0.32	1.7	89	17	0.19	5

Table 4. A. Table displaying the different parameters obtained for the fit of Eq. (9). B. Table showing the rheological parameters calculated from the values in panel A.

The numerical values obtained for viscosity, relaxation time, compliance, and elastic modulus are displayed in the last 4 columns of Table 4B. We can observe a large variability on these values for the different curves, revealing a very heterogeneous rheological behavior. The values of viscosity range from 89 $Pa \cdot s$ up more than $4 \cdot 10^4$ $Pa \cdot s$. The relaxation time varies within tenths up to hundreds of seconds; and the elastic modulus from a few up to about a hundred Pa. This large variability may be partly due to the fact that in some occasions during the first aspiration step (panels A and C, Fig. 43) only few vesicles penetrate inside the constriction. Fig. 44C shows the first pressure increase step of the aspiration curve of Fig. 43C. Indeed, in the first step, the aspiration is limited by the presence of two large vesicles, with a diameter $D_{vesicle}$ comparable to that of the constriction width so $D_{vesicle}/\ W_c \cong 0.7$. In the first pressure step, only a few vesicles were aspirated inside the constriction. It was not only until the application of the second pressure step that the aggregate got effectively aspirated inside the constriction. Our observations suggest that the viscoelastic response may be influenced by the inner structure of the aggregate, in which the mechanical properties of individual vesicles may come into play. The same behavior has been observed in the aspiration experiment displayed in Fig. 43A. In this case, however, there is only one single vesicle in the front, with a $D_{vesicle}/\ W_c \cong 0.8$. Altough we chose the constriction width of the channel to be larger than the vesicle diameter (Sec. 2.5.1, Chapter 2), due to the large polydispersity of the sample some vesicles had diameters comparable to the constriction width. Therefore, these vesicles could interfere in the measurement of the global rheological properties of the aggregates.

We can compare the results obtained for vesicle prototissues to those reviewed in section 1.2.4 from Chapter 1. Even though they are different systems with different mechanical properties, comparing their values can contribute to gain more insight in the role that the different components of the cell play in the rheological behavior of tissues. For Guevorkian *et al.* [13], the value of the viscosity and the relaxation time obtained for their murine sarcoma cell aggregates measured by micropipette aspiration were of $1.9 \pm 0.3 \cdot 10^5\ Pa \cdot s$ and 44$\pm$7 min respectively. The elastic modulus E was also calculated, with a value of $700 \pm 100\ Pa$. Kashkooli *et al.* [92] obtained values in the order of $10^3\ Pa \cdot s$ for their ectoderm and mesoderm *Xenopus* explants, measured also by micropipette aspiration. Tlili *et al.* [112] obtained a relaxation time of 70$\pm$15 min for the Stokes flow of migrating epithelial MDCK monolayer in microfluidic confinement. The flow of a cellular tissue is determined by several factors, the most important being the rheological properties of individual cells, their energy of adhesion, their rearrangements, and cell division. The last term, however, will be excluded from the discussion because the cellular systems reviewed either use a drug to inhibit cell divisions or have proof that cell divisions do not affect the flow of the tissue studied. The most important difference between the systems reviewed in the literature and the vesicle prototissue is that cells have an acto-myosin cortex under their membrane, while vesicles do not. Such cell cortex allows cells to deforms elastically after a stress is applied to them for a short period of time, yet it is viscous enough to flow when this stress is kept for longer timescales. Vesicles do not have an actomyosin cortex and therefore their rheological properties will be given by their phospholipid membrane and the fluid contained inside their inner compartment. Since the viscosity of the cell cytoplasm and water are roughly the same, the presence or not of an actomyosin cortex plays a very important role in determining the differences in the individual rheological properties between cells and vesicles, which certainly accounts for the low elastic modulus obtained for the vesicle biomimetic tissue in comparison to that obtained by, for example, Guevorkian *et al.* [13] in their murine sarcoma cell aggregates.

The second most important difference is the timescale of rearrangements. The cell rearrangements and the timescale in which they occur directly influence the viscosity of the tissue and its relaxation time t_{relax}. In our vesicle prototissue, the observed rearrangements take place in a timescale in the order of 0.5 s, as shown in section 4.1.2. However, this value should be taken with caution, since it is intended to give an estimated value only and further quantification should be done to obtain more reliable values. For comparison, the duration of a T1 transition in a soap foam flowing through an obstacle is of 0.05 s [79]. The same event in streptavidin-biotin functionalized emulsion droplets flowing through a constriction occurs within a timescale of 2.5 s [118]. The rearrangements occurring in a migrating cell monolayer calculated by Tlili *et al.* [112] were estimated to have a duration of 1h. This difference in the duration of the rearrangements is reflected in the relaxation time: the values obtained in our vesicle prototissue are of approximately 30 s whereas the values obtained by Guevorkian *et al.* [13] and Tlili *et al.* [112] for their cellular tissues is of 44 and 70 minutes respectively. The need for longer rearrangement timescales in living systems can be explained not only by their mechanical properties, but also by the active response of cells to stress, which does not occur in vesicle prototissues or adhesive emulsions because they are passive systems. Cellular tissues need longer timescales to orchestrate a response to an external mechanical stimulus, in both intra and intercellular level. Through mechanosensory mechanisms, the mechanical input triggers a signaling cascade that prepares the cell for deformation. The output of the signaling cascade involves changes in the cell cortex structure and in the translocation of cadherin molecules to the membrane through exocytosis, which occurs within a timescale of tenths of seconds and minutes respectively [142,143]. At the same time, they also need to transmit this information to their neighboring cells to synchronize their collective movement and avoid potential disruptions of the tissue structure.

Finally, when comparing the results in the literature with the one obtained in our experiments, one must also take into account the differences between the experimental setups used for the measurements. Even though the experiments performed with micropipette aspiration and our microfluidic constriction are very similar, they still present some differences that may introduce variations in the observed results. Their main difference is that the micropipette aspiration allows the measuring of tissue properties in an open setup, in which the sample is not under any spatial confinement. In microfluidic aspiration, however, the setup is closed and the sample is under 2D confinement. Also, while both the micropipette and microfluidic aspiration experiments probe the properties of 3D-shaped aggregates by applying an external pressure, the experiment performed by Tlili *et al.* [112] studies the migration of a 2D monolayer of cells without any externally applied force.

Characterization of the maximal deformation as a function of the applied pressure

In this section, we aim to characterize the prototissue response at increasing applied pressures. For this, we set the maximal advancement of the aggregate protusion inside the constriction channel for each pressure step, that we call ΔL_{step}^{max}. This parameter is represented as a function of the applied pressure ΔP in Fig. 45, for the aspiration curves displayed in Fig. 43. It is possible to observe that in most cases the deformation of the aggregate follows a linear increase with the applied pressure for the first pressure steps, but this trend is lost at larger pressures. This behavior can be observed in all panels except C, in which the response of the aggregate to the applied pressure is proportional in every step. The linear fits performed in the linear regime obtained at low pressures are displayed in the caption of Fig. 45. There is an important heterogeneity in the observed responses, with slopes ranging from 80 to 490 µm/mbar. In some occasions (panels A and B), immediately after the loss of linearity occurs, there is a sharp increase on the aggregate deformation. In other cases (panel E), however, the deformation barely increases with the applied pressure until it reaches the value of approximately 1 mbar, and then it deforms from 30 to 90 µm in 10 s. The loss of linearity in the response to the applied stress may be due to reorganization of the inner structure of the prototissue, through the rearrengements of vesicles, that may occur only above a critical applied stress.

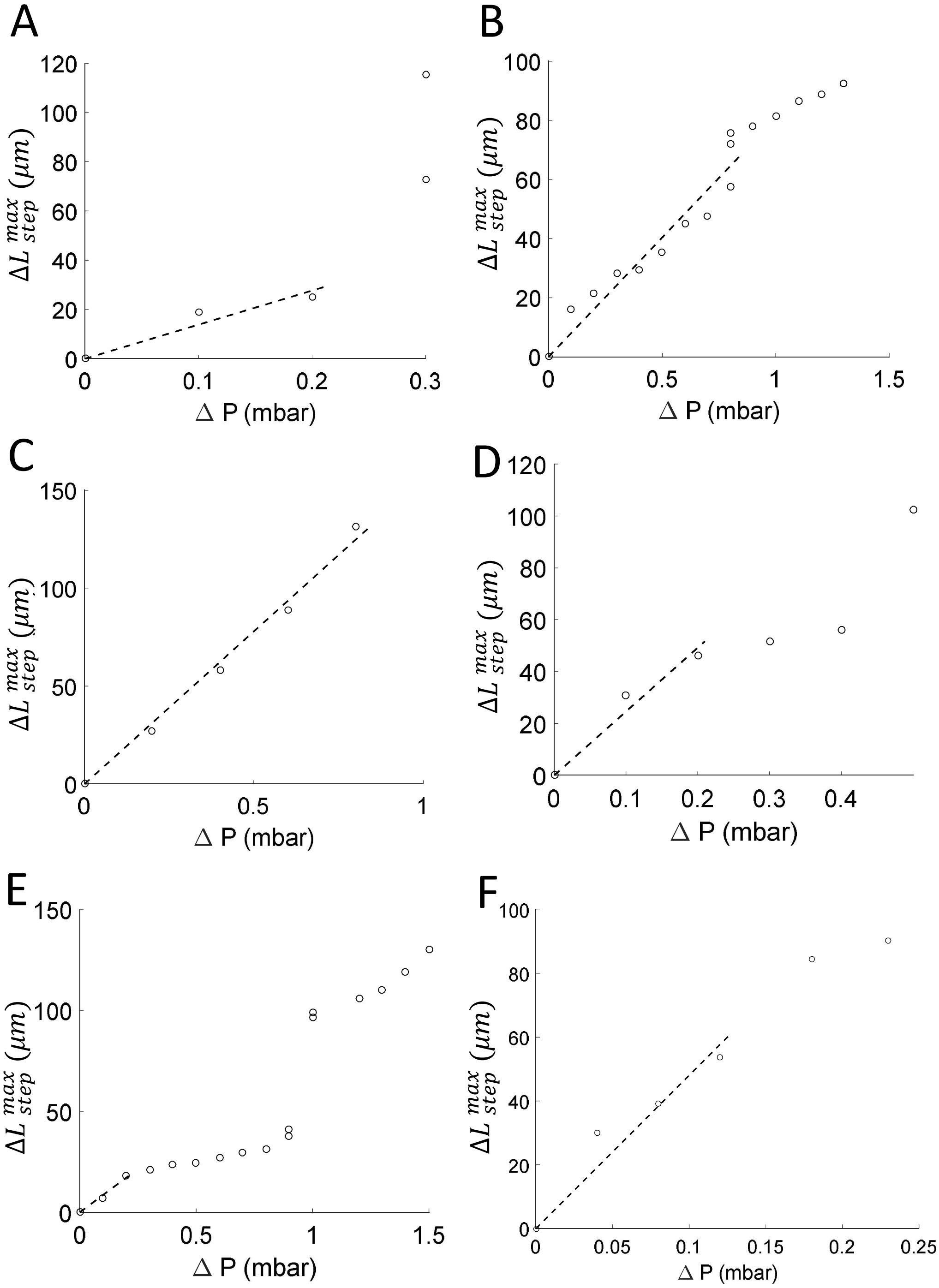

Fig. 45. Graphs displaying the maximal deformation of the aggregate for each step as a function of the applied pressure. For some steps, two values of ΔL_{step}^{max} can be found, which correspond to intermediate deformations. The slope of the linear fit and the R-square values are, from A to F: 139±(75) μm/mbar; R-square=0.9119, 81±(11) μm/mbar; R-square=0.9052, 156±(75) μm/mbar; R-square= 0.9903, 246±(13) μm/mbar; R-square= 0.9547, 86±(26) μm/mbar; R-square= 0.9779, 481±(141) μm/mbar; R-square= 0.9144.

Chapter 5 - Conclusions and perspectives.

5.1. Conclusions.

The main goals of this Thesis were (1) the conception of a biomimetic vesicle prototissue and (2) the characterization of its rheological properties by means of a microfluidic device.

The first part of the Thesis focused on the conception of a vesicle biomimetic prototissue with controllable mechanical properties. For this, two methods of vesicle production were used: electroformation and cDICE. Even though cDICE provides monodisperse size and enables fluid encapsulation, electroformation was the technique we chose for obtaining vesicles because of its high yield of production. Two strategies for driving vesicle-vesicle assembly were also used: streptavidin-biotin pair and DNA tethers. By changing the molar percentage of biotinylated lipids in the membranes and the streptavidin-biotin ratio it was possible to tune the size and compaction of the vesicle aggregates. However, we showed that the most effective way to tune the aggregate size was by modifying the total number of vesicles in solution. DNA tethers were also used as an alternative method for aggregation, which proved to be very effective in achieving high compaction degrees between vesicles. The last parameter that we aimed to control was the morphology of the aggregates. Finally, by modifiying the protocol of vesicle incubation we managed to obtain aggregates with a 2D morphology, which contrasted with the tridimensional shape obtained with a regular incubation method.

The second part of the Thesis focused on the rheological properties of the vesicle prototissues by using a microfluidic constriction device. The deformation of the vesicle aggregates as they passed through the constriction was recorded and analyzed, both qualitatively and quantitatively. We were able to identify different behaviors such as elastic and plastic deformation, rupture of the aggregates, formation of filaments and oscillatory behaviors, both periodic and intermittent. On the quantitative side, we characterized the rheological response of the aggregates depending on their size. We first determined the hydraulic resistance of aggregates with large and moderate sizes, and we found that large aggregates offer more resistance and therefore need higher pressure values in order to flow through the constriction. For aggregates with a moderate size, the change in shape and compaction was analyzed after passage through the constriction. No significant changes were observed, revealing that these aggregates display a predominantly elastic behavior. In order to probe the rheological properties of large aggregates a different approach was used, which consisted in analyzing the advancing front of the aggregates inside the constriction with time for increasing pressure steps. The data was fitted with a simple Maxwell viscoelastic model, which allowed us to determine their elastic modulus, viscosity and relaxation time. These results were compared to the values obtained for *Xenopus* embryonic tissues, epithelial MDCK tissue, and murine sarcoma cell aggregates. In all cases, the values for the elastic modulus, viscosity and relaxation time were larger in the biological systems than in the vesicle prototissues, mainly due to the absence of an acto-myosin cortex. The timescale for topological changes in the structure as cell rearrangements were also compared, both with epithelial and biomimetic tissues such as streptavidin-biotin functionalized emulsions and foams. The differences in these timescales can help interpreting the differences in the values obtained for the rheological parameters between cellular tissues and biomimetic tissues. Finally, the maximal deformation of the aggregate with the applied pressure was measured for increasing pressure steps. A first regime at low pressure values which was linear, followed by a loss of linearity at high pressure values. We believe that changes in the tissue microstructure, namely through vesicle-vesicle rearrengements, may account for this non-linear flow behavior.

Several complementary approaches were tested in order to produce the vesicle prototissues, which have opened new venues for improving the complexity and biomimetic potential or the prototissues. These strategies will be described in the following Perspectives section, which includes the role of vesicle activity, tissue compaction, and vesicle polydispersity.

5.2. Perspectives.

5.2.1. Conception of an active biomimetic tissue.

The aim of pursuing this encapsulation was to make vesicles which are capable of internal activity and bind them together forming an aggregate, by using the streptavidin-biotin pair. By doing so, we want to probe how the activity of the vesicles changes the conditions for their aggregation into a tissue-like structure and what new properties this activity might confer to such tissue. This encapsulation would represent an increasing step in the complexity of the system, in which activity would bring it closer to mimicking real tissues. The ultimate goal of this encapsulation would be to elucidate how the inner activity of the vesicles affects the rheological behavior of the aggregate under microfluidic flow. A detailed description on the active reconstitution and its encapsulation by using cDICE is given in Chapter 2.

Following a successful encapsulation, the active vesicles were imaged with epifluorescence microscopy. Upon observation of the samples, we were able to distinguish between three types of microtubule distribution within the vesicle interior. These structures have already been described by Keber *et al.* [74] in 2014:

- Network-like: Fig. 46A. The filaments were homogeneously distributed throughout the inner surface of the vesicle, forming a mesh underneath the lipid membrane.
- Ring-like: Fig. 46B. Filaments assembled in one or multiple rings around the inner surface of the vesicle.
- Clumped filaments: Fig. 46C. Microtubule filaments were found in the center of the vesicle, without a defined structure.

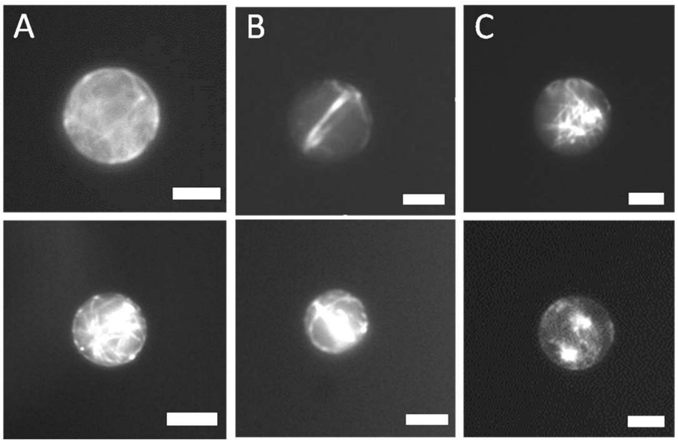

Fig. 46. Image displaying three types of microtubule distribution within the vesicles. The mean vesicle diameter was 15±3 μm. A. Network-like structure, B. Ring-like structure, C. Clumped filaments. Exposition time 1.5 s. Scale bar 10 μm.

Active vesicles were recorded to observe how the microtubule configuration changed with time. We observed movement within the microtubules inside the vesicles in both ring-like and network-like configurations, shown in Fig. 46A and B respectively. It was also possible to observe how the vesicles displayed translation motion along the duration of the film. Such movement could have been propelled by the inner activity of the vesicles or by currents formed in the observation chamber. These displacements typically occurred at a velocity of about 1 μm/s. Vesicles with clumped filaments inside them had no internal or external movement. This loss of activity could potentially be caused by a lack of microtubules, or the formation of pores in the vesicle membrane that resulted in the loss of cofactors and enzymes necessary for regenerating the ATP system. Also, vesicles that had diameters smaller than 10 μm did not display the necessary space for the nematic phase to form in the vesicle membrane, therefore resulting in a global loss of activity and microtubule functionality. This dependency of the vesicle activity with its diameter is in agreement with the results obtained by Keber *et al.* [74].

Despite having successfully obtained active vesicles, both the encapsulation setup and the biomimetic system itself present some constraints that limit the scope of the experiments. The first and most important limitation is the low yield of vesicle production: the small number of vesicles obtained per experiment makes it difficult to obtain statistically significant results. According to our experimental conditions and as reported by Loiseau *et al.* [121], it is not surprising, since encapsulation by cDICE experiences a decrease in efficiency when working with solutions with high osmolarity. A reduction in the yield and an increase in the size polydispersity of the vesicles has also been reported, for vesicles with diameters above 60 µm, which are the size ranges that we expected to obtain with our protocol. Another important issue that contributes to the lowering of the encapsulation efficiency is the clogging of the capillary. The biomimetic mixture has a very fast polymerization time, which starts as soon as their different components are mixed, so the loading of the solution to the capillary and the injection to the continuous phase should be performed as efficiently as possible to avoid clogging. If the obstruction occurs, one can increase the pressure of injection, which might result in the loss of a significant amount of the sample volume. Another limitation of our experiments arises from the visualization setup. In order to have a correct visualization of the active vesicles with epifluorescence microscopy it was necessary to use high exposition times, around 1 or 2 seconds, which limited the timescale of registering the vesicle activity. This implies that phenomena taking place below these typical timescales could not be recorded, and also that the fluorescent components of the vesicle experienced photobleaching if the recordings lasted longer than approximately 10 seconds. This

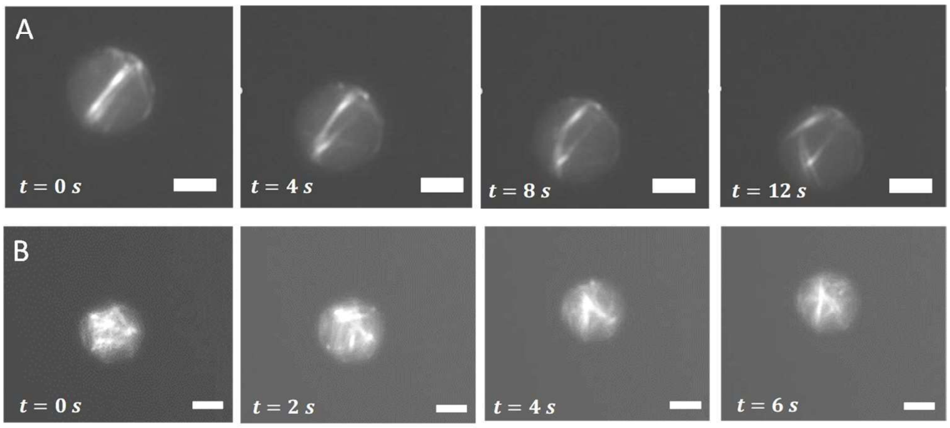

Fig. 47. Time lapses displaying the dynamic behavior of active vesicles. Fig. 47A shows a vesicle with a ring-like structure that vanishes at a time interval of 12 s. The vesicle displays a translational movement from top to bottom. In Fig. 47B it is possible to see changes in the inner microtubule network at a time interval of 6 s, along with a displacement of the vesicle towards the upper part of the image. Scale bar 10 µm.

allowed us to get limited information on their dynamics, since it has been reported that these active vesicles should be active up to more than 30 minutes after encapsulation [74]. This last limitation could be partially overcome by using confocal microscopy, enabling us to limit photobleaching and visualizing phenomena below the timescale of seconds.

5.2.2. The impact of vesicle polydispersity on the biomimetic tissue rheology.

One of the main characteristics of living tissues is the uniformity of the cell size or, in other words, their low size polydispersity [144]. We produced vesicles using electroformation, which guarantees good yield and reproducibility, but with the downside of having a vesicle population with high size polydispersity (see Fig,. 18, Chapter 2). The cell size polydispersity of a tissue is an important parameter to take into consideration, since it impacts its rheological properties. For example, Pontani *et al.* [118] reported changes in the flow behavior of adhesive biomimetic emulsion droplets depending on their polydispersity, in a system which resembles the structure of the vesicle prototissue conceived in this Thesis. It was seen that monodisperse emulsions presented a higher number of droplets involved in a rearrangement event as they flowed through a microfluidic constriction, suggesting that they were more prone to displaying plastic behavior under stress. The cDICE technique allows to generate vesicles with low polydispersity (<11%) [55]. We successfully

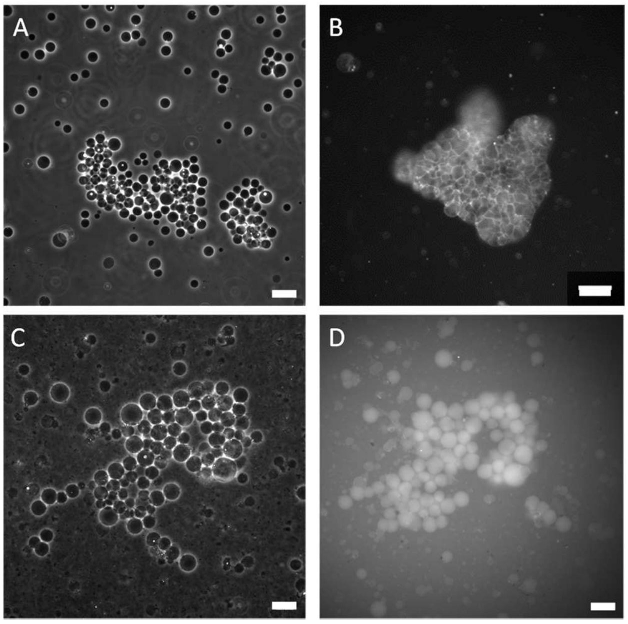

Fig. 48. Figures A and B display aggregates made with cDICE vesicles and DNA linkers at a concentration of 64 and 161 *nM* respectively. Figures C and D display the same Streptavidin-biotin bound aggregate in phase contrast (C) and epifluorescence microscopy (D). The vesicles contain 2.5% mol/mol biotin in their membranes and X=0.45. The fluorescence in Fig. 4.D is provided by fluorescent beads that have been encapsulated with cDICE. Scale bar 50 μm.

synthesized a few aggregates with cDICE vesicles, for which vesicle adhesion was driven using DNA or the streptavidin-biotin pair, as shown in Figure 48. The next step would be to study the flow behavior of monodisperse-vesicle prototissues using microfluidic confinement, and compare it to the results obtained for polydisperse vesicle prototissues, which would conttibute to the understanding of the role that polydispersity plays in the rheological properties of cellular materials.

5.2.3. The role of cohesion on the biomimetic tissue rheology.

The implications of adhesion between cells have not been explored quantitatively in this Thesis, but they undoubtedly play in important role in the rheological properties of tissues, as highlighted in sections 1.1 and 1.2 of Chapter 1. The expression levels of cadherin molecules in cells forming a tissue determines its degree of cohesion, which has a direct impact on its flow behavior [145]. In order to probe more extensively how changing the cohesion of the biomimetic tissue affects its flow behavior, it would be necessary to reproduce the microfluidic aspiration experiments but changing the ratio, concentration or type of linker used for the vesicle aggregation process. When working with the streptavidin-biotin pair, we showed it was possible to change the degree of adhesion between vesicles by changing two parameters: the streptavidin to biotin ration (X) or the biotin percentage in the membrane. Since changing any of the two would result in a change in the average aggregate size, one should also adjust the total vesicle volume added in order to keep the size of the aggregates constant. Another possibility to tune the degree of adhesion between vesicles is by using DNA tethers. While the adhesion properties of the tissue have been explored mainly using the streptavidin-biotin pair, we have observed that with DNA we can access a larger range of aggregate cohesiveness. Our observations are in agreement with the findings of Feng *et al.* [33], which highlight that the degree of adhesion between DNA-functionalized biomimetic emulsion droplets increases with the DNA coverage in the droplet surface. Similar observations have been reported by Golovkova *et al.* [82], which studied the phenomena of adhesion in 2D-packings of oil-in-water emulsion droplets functionalized with streptavidin-biotin and DNA tethers. It was seen that for comparable adhesiveness values calculated as the number of adhesion patches within a droplet, DNA emulsions displayed higher average droplet deformation than that of streptavidin-biotin emulsions, which could be indicative of a more elastic-dominated behavior when exposed to an external stress. The mechanical properties of vesicle aggregates with DNA tethers are different from the mechanical properties of the aggregates obtained with the streptavidin-biotin pair; in particular, they display a larger degree of cohesion. Thus, it would be interesting to test the rheological properties of the two types of aggregates in the microfluidic device that we have conceived, in order to elucidate the role of vesicle-vesicle adhesion on their rheological response.

Bibliography

1. Morange M. Physics, biology and history. *Interdisciplinary Science Reviews*. 2013;32(2):107–12.
2. Thompson DW. On Growth and Form. Cambridge: At the University Press; 1917.
3. Foty RA, Steinberg MS. The differential adhesion hypothesis: a direct evaluation. *Developmental biology*. 2005;278(1):255–63.
4. Erdemci-Tandogan G, Clark MJ, Amack JD, Manning ML. Tissue Flow Induces Cell Shape Changes During Organogenesis. *Biophysical Journal*. 2018;115:2259–70.
5. Aigouy B, Farhadifar R, Staple DB, Sagner A, Röper JC, Jülicher F, et al. Cell flow reorients the axis of planar polarity in the wing epithelium of Drosophila. *Cell*. 2010;142(5):773–86.
6. Ranft J, Basan M, Elgeti J, Joanny JF, Prost J, Jülicher F. Fluidization of tissues by cell division and apoptosis. *Proceedings of the National Academy of Sciences of the United States of America*. 2010;107(49):20863–8.
7. Winters BS, Shepard SR, Foty RA. Biophysical measurement of brain tumor cohesion. *International Journal of Cancer*. 2005;114(3):371–9.
8. Alberts B, Johnson A, Julian Lewis, Morgan D, Raff M, Roberts K, et al. Molecular Biology of the Cell: Sixth International Student Edition. *Garland Science*. 2018;1106.
9. Canty L, Zarour E, Kashkooli L, François P, Fagotto F. Sorting at embryonic boundaries requires high heterotypic interfacial tension. *Nature Communications*. 2017;8(1).
10. Pitulescu M, Adams R. Eph/ephrin molecules--a hub for signaling and endocytosis. *Genes & development*. 2010;24(22):2480–92.
11. Manning ML, Foty RA, Steinberg MS, Schoetz EM. Coaction of intercellular adhesion and cortical tension specifies tissue surface tension. *Proceedings of the National Academy of Sciences of the United States of America*. 2010;107(28):12517–22.
12. Kalluri R, Weinberg RA. The basics of epithelial-mesenchymal transition. *The Journal of Clinical Investigation*. 2009;119(6):1420–8.
13. Guevorkian K, Colbert MJ, Durth M, Dufour S, Brochard-Wyart F. Aspiration of biological viscoelastic drops. *Physical Review Letters*. 2010;104(21):1–4.
14. Fenz SF, Sengupta K. Giant vesicles as cell models. *Integrative Biology*. 2012;4(9):982.
15. Marmottant P, Mgharbel A, Kä Fer J, Audren B, Rieu J-P, Vial J-C, et al. The role of fluctuations and stress on the effective viscosity of cell aggregates. *Proceedings of the National Academy of Sciences*. 2009;106(41):17271–5.
16. Lecuit T, As Y. E-cadherin junctions as active mechanical integrators in tissue dynamics. *Nature cell biology*. 2015;17(5):533–9.
17. Bhushan B. Biomimetics: lessons from nature-an overview. *Philosophical Transactions of the Royal Society*. 2009;(367):1445–86.
18. Jaggessar A, Shahali H, Mathew A, Yarlagadda PKDV. Bio-mimicking nano and micro-structured

surface fabrication for antibacterial properties in medical implants. *Journal of Nanobiotechnology*. 2017;15(1):1–20.

19. Serrano L. Synthetic biology: promises and challenges. *Molecular Systems Biology*. 2007;3(1):158.

20. Mantri S, Sapra KT. Evolving protocells to prototissues: rational design of a missing link. *Biochemical Society Transactions*. 2013;41(5):1159–65.

21. Li Q, Li S, Zhang X, Xu W, Han X. Programmed magnetic manipulation of vesicles into spatially coded prototissue architectures arrays. *Nature Communications*. 2020;11(1):1–9.

22. Fenz SF, Merkel R, Sengupta K. Diffusion and intermembrane distance: Case study of avidin and E-cadherin mediated adhesion. *Langmuir*. 2009;25(2):1074–85.

23. Sackmann E, Smith A-S. Physics of cell adhesion: some lessons from cell-mimetic systems. *Soft Matter*. 2014;10(11):1644–59.

24. Puech P-H, Feracci † H, Brochard-Wyart F. Adhesion between Giant Vesicles and Supported Bilayers Decorated with Chelated E-Cadherin Fragments. 2004;

25. De Souza TP, Bossa GV, Stano P, Steiniger F, May S, Luisi PL, et al. Vesicle aggregates as a model for primitive cellular assemblies. *Physical Chemistry Chemical Physics*. 2017;19(30):20082–92.

26. Villringer S, Madl J, Sych T, Manner C, Imberty A, Römer W. Lectin-mediated protocell crosslinking to mimic cell-cell junctions and adhesion. *Scientific Reports*. 2018;8(1):1–11.

27. E. T. Kisak, M. T. Kennedy, Trommeshauser D, Zasadzinski JA. Self-Limiting Aggregation by Controlled Ligand—Receptor Stoichiometry. *Langmuir*. 2000;16(6):2825–31.

28. Pontani L-L, Jorjadze I, Viasnoff V, Brujic J. Biomimetic emulsions reveal the effect of mechanical forces on cell-cell adhesion. *Proceedings of the National Academy of Sciences*. 2012;109(25):9839–44.

29. Vermette P, Taylor S, Dunstan D, Meagher L. Control over PEGylated-Liposome Aggregation by NeutrAvidin—Biotin Interactions Investigated by Photon Correlation Spectroscopy. *Langmuir*. 2001;18(2):505–11.

30. Amjad OA, Mognetti BM, Cicuta P, Di Michele L. Membrane Adhesion through Bridging by Multimeric Ligands. *Langmuir*. 2017;33(5):1139–46.

31. Nam J, Santore MM, J N, MM S. The Adhesion Kinetics of Sticky Vesicles in Tension : The Distinction between Spreading and Receptor Binding. *Langmuir*. 2007;23(21):10650–60.

32. Bihr T, Fenz S, Sackmann E, Merkel R, Seifert U, Sengupta K, et al. Association rates of membrane-coupled cell adhesion molecules. *Biophysical Journal*. 2014;107(11):L33–6.

33. Dreyfus R, Chaikina P, Brujic J, Feng L, Pontani L-L. Specificity, flexibility and valence of DNA bonds guide emulsion architecture. 2013;(18):9816–23.

34. Hadorn M, Hotz PE. DNA-Mediated Self-Assembly of Artificial Vesicles. *PLOS ONE*. 2010;5(3):e9886.

35. Beales P, Vanderlick T. Specific binding of different vesicle populations by the hybridization of membrane-anchored DNA. *The Journal of Physical Chemistry*. 2007;111(49):12372–80.

36. Parolini L, Mognetti BM, Kotar J, Eiser E, Cicuta P, Di Michele L. Volume and porosity thermal regulation in lipid mesophases by coupling mobile ligands to soft membranes. *Nature Communications*. 2015;6:1–10.

37. Chan Y-HM, Lenz P, Boxer SG. Kinetics of DNA-mediated docking reactions between vesicles tethered to supported lipid bilayers. *Proceedings of the National Academy of Sciences*. 2007;104(48):18913–8.

38. Milcovich G, Lettieri S, Antunes FE, Medronho B, Fonseca AC, Coelho JFJ, et al. Recent advances in smart biotechnology: Hydrogels and nanocarriers for tailored bioactive molecules depot. *Advances in colloid and interface science*. 2017;249:163–80.

39. Bitounis D, Fanciullino R, Iliadis A, Ciccolini J. Optimizing Druggability through Liposomal Formulations: New Approaches to an Old Concept. *ISRN Pharmaceutics*. 2012;1–11.

40. Bangham AD, Standish MM, Watkins JC. Diffusion of Univalent Ions across the Lamellae of Swollen Phospholipids. *J. Mol. Biol*. 1965;13:238–52.

41. Hauser HO. The effect of ultrasonic irradiation on the chemical structure of egg lecithin. *Biochemical and Biophysical Research Communications*. 1971;45(4):1049–55.

42. Batzri S, Korn ED. Single bilayer liposomes prepared without sonication. *Biochimica et biophysica acta*. 1973;298(4):1015–9.

43. Angelova MI, Dimitrov DS. Liposome Electroformation. *Faraday Discussions of the Chemical Society*. 1986;81:303–11.

44. Angelova MI, Soléau S, Méléard P, Faucon F, Bothorel P. Preparation of giant vesicles by external AC electric fields. Kinetics and applications. *Trends in Colloid and Interface Science*. 1992;89:127–31.

45. Estes DJ, Mayer M. Electroformation of giant liposomes from spin-coated films of lipids. *Colloids and Surfaces B: Biointerfaces*. 2005;42(2):115–23.

46. Stein H, Spindler S, Bonakdar N, Wang C, Sandoghdar V. Production of isolated giant unilamellar vesicles under high salt concentrations. *Frontiers in Physiology*. 2017;8:1–16.

47. Horger KS, Estes DJ, Capone R, Mayer M. Films of agarose enable rapid formation of giant liposomes in solutions of physiologic ionic strength. *Journal of the American Chemical Society*. 2009;131(5):1810–9.

48. Van Swaay D, Demello A. Microfluidic methods for forming liposomes. *Lab on a Chip*. 2013;13(5):752–67.

49. Lin YC, Li M, Wang YT, Lai TH, Chiang JT, Huang KS. A new method for the preparation of self-assembled phospholipid microtubes using microfluidic technology. *Digest of Technical Papers - International Conference on Solid State Sensors and Actuators and Microsystems, TRANSDUCERS '05*. 2005;2:1592–5.

50. Dittrich PS, Heule M, Renaud P, Manz A. On-chip extrusion of lipid vesicles and tubes through microsized apertures. *Lab on a Chip*. 2006;6(4):488–93.

51. Funakoshi K, Suzuki H, Takeuchi S. Formation of giant lipid vesiclelike compartments from a planar lipid membrane by a pulsed jet flow. *Journal of the American Chemical Society*. 2007;129(42):12608–9.

52. Shum HC, Lee D, Yoon I, Kodger T, Weitz DA. Double emulsion templated monodisperse phospholipid vesicles. *Langmuir*. 2008;24(15):7651–3.

53. Pautot S, Frisken BJ, Weitz DA. Production of unilamellar vesicles using an inverted emulsion. *Langmuir*. 2003;19(7):2870–9.

54. Robinson T. Microfluidics and giant vesicles: creation, capture, and applications for biomembranes. *Advances in Biomembranes and Lipid Self-Assembly*. 2019;30:271–315.

55. Abkarian M, Loiseau E, Massiera G. Continuous droplet interface crossing encapsulation (cDICE) for high throughput monodisperse vesicle design. *Soft Matter*. 2011;7(10):4610–4.

56. Wilchek M, Bayer EA. Introduction to avidin-biotin technology. *Methods in Enzymology*. 1990;184(C):5–13.

57. Zempleni J, Wijeratne SSK, Hassan YI. Biotin. *BioFactors*. 2009;35(1):36–46.

58. Ren CL, Carvajal D, Shull KR, Szleifer I. Streptavidin-biotin binding in the presence of a polymer spacer. a theoretical description. *Langmuir*. 2009;25(20):12283–92.

59. Cuvelier D, Derényi I, Bassereau P, Nassoy P. Coalescence of Membrane Tethers: Experiments, Theory, and Applications. *Biophysical Journal*. 2005;88(4):2714.

60. Allen C, Dos Santos N, Gallagher R, Chiu GNC, Shu Y, Li WM, et al. Controlling the Physical Behavior and Biological Performance of Liposome Formulations Through Use of Surface Grafted Poly(ethylene Glycol). *Bioscience Reports*. 2002;22(2):225–50.

61. Hong F, Zhang F, Liu Y, Yan H. DNA Origami: Scaffolds for Creating Higher Order Structures. *Chemical Reviews*. 2017;117(20):12584–640.

62. Albrecht C, Blank K, Lalic-Mülthaler M, Hirler S, Mai T, Gilbert I, et al. DNA: a programmable force sensor. *Science*. 2003;301(5631):367–70.

63. Dreyfus R, Baudry J, Roper ML, Fermigier M, Stone HA, Bibette J. Microscopic artificial swimmers. *Nature*. 2005;437(7060):862–5.

64. Valignat MP, Theodoly O, Crocker JC, Russel WB, Chaikin PM. Reversible self-assembly and directed assembly of DNA-linked micrometer-sized colloids. *Proceedings of the National Academy of Sciences*. 2005;102(12):4225–9.

65. Hadorn M, Boenzli E, Sørensen KT, Fellermann H, Eggenberger Hotz P, Hanczyc MM. Specific and reversible DNA-directed self-assembly of oil-in-water emulsion droplets. 2012;109(50):20320–5.

66. Hoffecker IT, Arima Y, Iwata H. Tuning intercellular adhesion with membrane-anchored oligonucleotides. *Journal of the Royal Society Interface*. 2019;16(159):1–17.

67. Goodman SR, Zimmer WE. Cytoskeleton. *Medical Cell Biology: Third Edition*. 2008;59–100.

68. Bashirzadeh Y, Liu AP. Encapsulation of the cytoskeleton: towards mimicking the mechanics of a cell. *Soft Matter*. 2019;15(42):8425–36.

69. Pontani LL, Van Der Gucht J, Salbreux G, Heuvingh J, Joanny JF, Sykes C. Reconstitution of an Actin Cortex Inside a Liposome. *Biophysical Journal*. 2009;96(1):192–8.

70. Maan R, Loiseau E, Bausch AR. Adhesion of Active Cytoskeletal Vesicles. *Biophysical Journal*. 2018;115(12):2395–402.

71. Guevorkian K, Manzi J, Pontani LL, Brochard-Wyart F, Sykes C. Mechanics of Biomimetic Liposomes Encapsulating an Actin Shell. *Biophysical Journal*. 2015;109(12):2471–9.

72. Caorsi V, Lemière J, Campillo C, Bussonnier M, Manzi J, Betz T, et al. Cell-sized liposome doublets reveal active tension build-up driven by acto-myosin dynamics. *Soft Matter*. 2016;12(29):6223–31.

73. Sanchez T, Chen DTN, Decamp SJ, Heymann M, Dogic Z. Spontaneous motion in hierarchically assembled active matter. *Nature*. 2012;491(7424):431–4.

74. Keber FC, Loiseau E, Sanchez T, DeCamp SJ, Giomi L, Bowick MJ, et al. Topology and dynamics of active nematic vesicles. *Science*. 2014;345(6201):1135–9.

75. Serbus LR, Cha BJ, Theurkauf WE, Saxton WM. Dynein and the actin cytoskeleton control kinesin-driven cytoplasmic streaming in Drosophila oocytes. *Development*. 2005;132(16):3743–52.

76. Mattila PK, Lappalainen P. Filopodia: molecular architecture and cellular functions. *Nature Reviews Molecular Cell Biology 2008 9:6*. 2008;9(6):446–54.

77. Janmey PA, Georges PC, Hvidt S. Basic Concept and Preparation Culture Substrates for Cell Mechanical Studies Basic Rheology for Biologists. *Methods in Cell Biology*. 2007;83.

78. Dollet B. Local description of the two-dimensional flow of foam through a contraction. *Journal of Rheology*. 2010;54(4):741–60.

79. Dollet B, Graner F. Two-dimensional flow of foam around a circular obstacle: Local measurements of elasticity, plasticity and flow. *Journal of Fluid Mechanics*. 2007;585:181–211.

80. Gai Y, Bick A, Tang SKY. Timescale and spatial distribution of local plastic events in a two-dimensional microfluidic crystal. *Physical Review Fluids*. 2019;4(1):014201.

81. Golovkova I, Montel L, Wandersman E, Bertrand T, Prevost AM, Pontani L-L. Depletion attraction impairs the plasticity of emulsions flowing in a constriction. *Soft Matter*. 2020;16(13):3294–302.

82. Montel L, Golovkova I, Grigolon S, Wandersman E, Prevost AM, Bertrand T, et al. Adhesion Percolation Determines Global Deformation Behavior in Biomimetic Emulsions. *Frontiers in Physics*. 2021;9:547.

83. Stirbat TV, Tlili S, Houver T, Rieu J-PP, Barentin C, Ene Delanoë-Ayari H, et al. Multicellular aggregates: a model system for tissue rheology. *The European physical journal E Soft Matter*. 2013;36(8).

84. Weaire D, Rivier N. Soap, cells and statistics—random patterns in two dimensions. *Contemporary Physics*. 2006;25(1):59.

85. Neuman KC, Nagy A. Single-molecule force spectroscopy: optical tweezers, magnetic tweezers and atomic force microscopy. *Nature Methods*. 2008;5(6):491–505.

86. Gonzalez-Rodriguez D, Guevorkian K, Douezan S, Brochard-Wyart F. Soft matter models of developing tissues and tumors. *Science*. 2012;338(6109):910–7.

87. Forgacs G, Foty RA, Shafrir Y, Steinberg MS. Viscoelastic Properties of Living Embryonic Tissues: a Quantitative Study. *Biophysical Journal*. 1998;74(5):2227–34.

88. Miao C, Schiffhauer ES, Okeke EI, Robinson DN, Luo T. Parallel Compression Is a Fast Low-Cost Assay for the High-Throughput Screening of Mechanosensory Cytoskeletal Proteins in Cells. *ACS applied materials & interfaces*. 2017;9(34):28168.

89. Mitchison JM, Swann MM. The mechanical properties of the cell surface I. The cell elastimeter. *Journal of Experimental Biology*. 1954;31(3):443–60.

90. Maître JL, Niwayama R, Turlier H, Nedelec F, Hiiragi T. Pulsatile cell-autonomous contractility drives compaction in the mouse embryo. *Nature Cell Biology*. 2015;17(7):849–55.

91. Hochmuth RM. Micropipette aspiration of living cells. *Journal of Biomechanics*. 2000;33(1):15–22.

92. Kashkooli L, Rozema D, Espejo-Ramirez L, Lasko P, Fagotto F. Ectoderm to mesoderm transition by down-regulation of actomyosin contractility. *PLoS biology*. 2021;19(1).

93. Guo Q, Park S, Ma H. Microfluidic micropipette aspiration for measuring the deformability of single cells. *Lab on a Chip*. 2012;(12):2687–95.

94. Turlier H, Maître J. Mechanics of tissue compaction. *Seminars in Cell & Developmental Biology*. 2015;48:110–7.

95. Brodland GW, Veldhuis JH, Kim S, Perrone M, Mashburn D, Hutson S. CellFIT : A Cellular Force-Inference Toolkit Using Curvilinear Cell Boundaries. *PLoS ONE*. 2014;9(6):e99116.

96. Parent SE, Barua D, Winklbauer R. Mechanics of Fluid-Filled Interstitial Gaps. I. Modeling Gaps in a Compact Tissue. *Biophysical Journal*. 2017;113(4):913–22.

97. Barua D, Parent SE, Winklbauer R. Mechanics of Fluid-Filled Interstitial Gaps. II. Gap Characteristics in Xenopus Embryonic Ectoderm. *Biophysical Journal*. 2017;(113):923–36.

98. Beebe DJ, Mensing GA, Walker GM. Physics and Applications of Microfluidics in Biology. *Annu Rev Biomed Eng*. 2003;4:261–86.

99. Sackmann EK, Fulton AL, Beebe DJ. The present and future role of microfluidics in biomedical research. *Nature*. 2014;507(7491):181–9.

100. Matthews K, Duffy SP, Myrand-Lapierre M-E, Ang RR, Li L, Scott MD, et al. Microfluidic analysis of red blood cell deformability as a means to assess hemin-induced oxidative stress resulting from Plasmodium falciparum intraerythrocytic parasitism. *Integrative Biology*. 2017;9(6):519–28.

101. Yeom E, Lee SJ. Microfluidic-based speckle analysis for sensitive measurement of erythrocyte aggregation: A comparison of four methods for detection of elevated erythrocyte aggregation in diabetic rat blood. *Biomicrofluidics*. 2015;9(2).

102. Horton RE. Microfluidics for investigating vaso-occlusions in sickle cell disease. *Microcirculation*. 2017;24(5).

103. Aich A, Lamarre Y, Sacomani DP, Kashima S, Covas DT, de la Torre LG. Microfluidics in Sickle Cell Disease Research: State of the Art and a Perspective Beyond the Flow Problem. *Frontiers in Molecular Biosciences*. 2021;7:252.

104. Loiseau E, Massiera G, Mendez S, Martinez PA, Abkarian M. Microfluidic study of enhanced deposition of sickle cells at acute corners. *Biophysical Journal*. 2015;108(11):2623–32.

105. Tran QD, Marcos, Gonzalez-Rodriguez D. Permeability and viscoelastic fracture of a model tumor under interstitial flow. *Soft Matter*. 2018;14(30):6386–92.

106. Tran QD, Gonzalez-Rodriguez D. Quantitative characterization of viscoelastic fracture induced by time-dependent intratumoral pressure in a 3D model tumor. *Biomicrofluidics*. 2019;13:54107.

107. Samal P, van Blitterswijk C, Truckenmüller R, Giselbrecht S, Samal P, van Blitterswijk C, et al. Grow with the Flow: When Morphogenesis Meets Microfluidics. *Advanced Materials*. 2019;31(1805764):1–17.

108. Zheng Y, Shao Y, Fu J. A microfluidics-based stem cell model of early post-implantation human development. *Nature Protocols*. 2020;16(1):309–26.

109. Wu Q, Liu J, Wang X, Feng L, Wu J, Zhu X, et al. Organ-on-a-chip: recent breakthroughs and future prospects. *BioMedical Engineering OnLine*. 2020;19(1):1–19.

110. Roman GT, Chen Y, Viberg P, Culbertson AH, Culbertson CT. Single-cell manipulation and analysis using microfluidic devices. *Analytical and Bioanalytical Chemistry*. 2007;387(1):9–12.

111. Riahi R, Tamayol A, Shaegh SAM, Ghaemmaghami A, Dokmeci MR, Khademshosseini A. Microfluidics for Advanced Drug Delivery Systems. *Current opinion in chemical engineering*. 2015;7:101.

112. Tlili S, Durande M, Gay C, Ladoux B, Graner F, Delanoë-Ayari H. Migrating Epithelial Monolayer Flows Like a Maxwell Viscoelastic Liquid. *Physical review letters*. 2020;125(8).

113. Gaush CR, Hard WL, Smith TF, Read WO. Characterization of an established line of canine kidney cells (MDCK). *Proceedings of the Society for Experimental Biology and Medicine.* 1966;122(3):931–5.

114. Tlili S, Gauquelin E, Li B, Cardoso O, Ladoux B, Ayari HD, et al. Collective cell migration without proliferation: density determines cell velocity and wave velocity. *Royal Society Open Science*. 2018;5(5).

115. Cassiman JJ, Bernfield MR. Use of preformed cell aggregates and layers to measure tissue-specific differences in intercellular adhesion. *Developmental biology*. 1976;52(2):231–45.

116. Chu YS, Thomas WA, Eder O, Pincet F, Perez E, Thiery JP, et al. Force measurements in E-cadherin-mediated cell doublets reveal rapid adhesion strengthened by actin cytoskeleton remodeling through Rac and Cdc42. *The Journal of cell biology*. 2004;167(6):1183–94.

117. Hall BK. Germ Layers and the Germ Layer Theory Revisited. *Evolutionary Biology*. 1997;30:121-186.

118. Golovkova I, Montel L, Pan F, Wandersman E, Prevost AM, Bertrand T, et al. Adhesion as a trigger of droplet polarization in flowing emulsions. *Soft Matter*. 2021;17(14):3820–8.

119. Sutherland A, Keller R, Lesko A. Convergent extension in mammalian morphogenesis. *Seminars in cell & developmental biology*. 2020;100:199–211.

120. Okumura Y, Iwata Y. Electroformation of giant vesicles on indium tin oxide (ITO)-coated poly(ethylene terephthalate) (PET) electrodes. *Membranes*. 2011;1(2):109–18.

121. Loiseau E. Approche biomimétique de la vaso-occlusion dans la drépanocytose : production de vésicules et microfluidique. Université de Montpellier; 2012.

Acknowledgements

I would like to dedicate this last page to all the people that have made this Thesis a reality. First and foremost, I would like to thank Gladys Massiera and Laura Casanellas for having given me the opportunity of taking part in this PhD project. Specially, thanks to Laura for the patience, dedication and support offered during all this time; it must not have been easy to teach a biologist to think in terms of physics! I would also like to thank all the members of the jury for their feedback, observations and valuable discussions. More specifically, thanks to Andrea Parmeggiani for being there every year in my comité de suivi de thèse, for being able to see my progress and for encouraging me to hold on to my PhD until the end. Thanks also to Remi Merindol and Martin in for fruitful exchanges on chemistry and biophysics, and to François Fagotto for giving us advice from the perspective of a cell biologist. Thanks to Élodie Jublanc and Vicki Diackou from the MRI service for their help with confocal microscopy, the SOCSAM team from the University of Barcelona for providing us with the precious active biomimetic samples and the Juan José Rubio group from LPHI for keeping them safe in their -80°C freezer.

I would like to thank all the Soft Matter team from the Laboratoire Charles Coulomb for their unconditional support. Thanks to Ameur and Juliette for their 'postdoc wisdom' and for always being supportive when science (and life) got too overwhelming. Thanks also to Carole-Ann for sharing with me the adventure of being a PhD student at L2C, and for all the moments that we have lived together, in and out of the lab – the good, the bad and the ugly.

Last, I want to thank my friends, my flatmates, and my family for always being there for me. There are too many names to list here, but I just want to let you know that you are the best and I am very happy to have all of you in my life. Without you, none of this would have been possible!

Laura Casas Ferrer

Montpellier, 8th March 2022